



**AFRL-RB-WP-TR-2009-3076**

**AERO-OPTICS CODE DEVELOPMENT**  
**Experimental Databases and AVUS Code Improvements**

**Scott E. Sherer**

**Computational Sciences Branch**  
**Aeronautical Sciences Division**

**MARCH 2009**  
**Interim Report**

**Approved for public release; distribution unlimited.**

*See additional restrictions described on inside pages*

**STINFO COPY**

**AIR FORCE RESEARCH LABORATORY**  
**AIR VEHICLES DIRECTORATE**  
**WRIGHT-PATTERSON AIR FORCE BASE, OH 45433-7542**  
**AIR FORCE MATERIEL COMMAND**  
**UNITED STATES AIR FORCE**

## NOTICE AND SIGNATURE PAGE

Using Government drawings, specifications, or other data included in this document for any purpose other than Government procurement does not in any way obligate the U.S. Government. The fact that the Government formulated or supplied the drawings, specifications, or other data does not license the holder or any other person or corporation; or convey any rights or permission to manufacture, use, or sell any patented invention that may relate to them.

This report was cleared for public release by the USAF 88<sup>th</sup> Air Base Wing (88 ABW) Public Affairs Office (PAO) and is available to the general public, including foreign nationals. Copies may be obtained from the Defense Technical Information Center (DTIC) (<http://www.dtic.mil>).

AFRL-RB-WP-TR-2009-3076 HAS BEEN REVIEWED AND IS APPROVED FOR PUBLICATION IN ACCORDANCE WITH ASSIGNED DISTRIBUTION STATEMENT.

\*//Signature//

SCOTT SHERER, Program Manager  
Computational Sciences Branch  
Aeronautical Sciences Division

//Signature//

REID MELVILLE, Chief  
Computational Sciences Branch  
Aeronautical Sciences Division

//Signature//

MATTHEW BURKINSHAW  
Technical Advisor  
Aeronautical Sciences Division  
Air Vehicles Directorate

This report is published in the interest of scientific and technical information exchange, and its publication does not constitute the Government's approval or disapproval of its ideas or findings.

\*Disseminated copies will show “//Signature//” stamped or typed above the signature blocks.

REPORT DOCUMENTATION PAGE				Form Approved OMB No. 0704-0188	
<p>The public reporting burden for this collection of information is estimated to average 1 hour per response, including the time for reviewing instructions, searching existing data sources, gathering and maintaining the data needed, and completing and reviewing the collection of information. Send comments regarding this burden estimate or any other aspect of this collection of information, including suggestions for reducing this burden, to Department of Defense, Washington Headquarters Services, Directorate for Information Operations and Reports (0704-0188), 1215 Jefferson Davis Highway, Suite 1204, Arlington, VA 22202-4302. Respondents should be aware that notwithstanding any other provision of law, no person shall be subject to any penalty for failing to comply with a collection of information if it does not display a currently valid OMB control number. <b>PLEASE DO NOT RETURN YOUR FORM TO THE ABOVE ADDRESS.</b></p>					
1. REPORT DATE (DD-MM-YY) March 2009		2. REPORT TYPE Interim		3. DATES COVERED (From - To) 01 March 2006 – 29 February 2008	
4. TITLE AND SUBTITLE AERO-OPTICS CODE DEVELOPMENT Experimental Databases and AVUS Code Improvements				5a. CONTRACT NUMBER In-house	
				5b. GRANT NUMBER	
				5c. PROGRAM ELEMENT NUMBER 62764	
6. AUTHOR(S) Scott E. Sherer				5d. PROJECT NUMBER A08A	
				5e. TASK NUMBER	
				5f. WORK UNIT NUMBER 0B	
7. PERFORMING ORGANIZATION NAME(S) AND ADDRESS(ES) Computational Sciences Branch (AFRL/RBAC) Aeronautical Sciences Division Air Force Research Laboratory, Air Vehicles Directorate Wright-Patterson Air Force Base, OH 45433-7542 Air Force Materiel Command, United States Air Force				8. PERFORMING ORGANIZATION REPORT NUMBER AFRL-RB-WP-TR-2009-3076	
9. SPONSORING/MONITORING AGENCY NAME(S) AND ADDRESS(ES) Air Force Research Laboratory Air Vehicles Directorate Wright-Patterson Air Force Base, OH 45433-7542 Air Force Materiel Command United States Air Force				10. SPONSORING/MONITORING AGENCY ACRONYM(S) AFRL/RBAC	
				11. SPONSORING/MONITORING AGENCY REPORT NUMBER(S) AFRL-RB-WP-TR-2009-3076	
12. DISTRIBUTION/AVAILABILITY STATEMENT Approved for public release; distribution unlimited.					
13. SUPPLEMENTARY NOTES PAO Case Number: 88ABW 2009-1214; Clearance Date: 26 Mar 2009. Report contains color.					
14. ABSTRACT Work has been performed in and coordinated by the Computational Sciences Branch to develop an in-house aero-optics predictive capability. This interim report summarizes the first two years of this effort. The work during this period has focused on acquiring high-quality experimental databases consisting of both aerodynamic and aero-optical measurements for future code validation, and the evaluation and improvement of the unstructured flow solver AVUS to solve representative flow fields.					
15. SUBJECT TERMS Aero-optics, computational fluid dynamics, turrets, shear layers, AVUS					
16. SECURITY CLASSIFICATION OF:			17. LIMITATION OF ABSTRACT: SAR	18. NUMBER OF PAGES 76	19a. NAME OF RESPONSIBLE PERSON (Monitor) Scott E. Sherer 19b. TELEPHONE NUMBER (Include Area Code) N/A
a. REPORT Unclassified	b. ABSTRACT Unclassified	c. THIS PAGE Unclassified			

# Table of Contents

<b>List of Figures</b>	<b>iv</b>
<b>List of Tables</b>	<b>vi</b>
<b>Acknowledgements</b>	<b>vii</b>
<b>1 Introduction</b>	<b>1</b>
<b>2 Experimental Database</b>	<b>2</b>
2.1 Compressible Shear Layer . . . . .	2
Experimental Set-Up . . . . .	2
Pressure Measurements . . . . .	2
Hot-Wire Measurements . . . . .	3
Malley Probe Measurements of OPD . . . . .	3
Instantaneous Wavefronts . . . . .	3
2.2 1.5-Inch Turret with Conformal Window . . . . .	3
Experimental Set-Up . . . . .	3
Velocity and Pressure Measurements . . . . .	4
Optical Measurements . . . . .	9
2.3 1-Foot Turret with Conformal Window . . . . .	22
Experimental Set-Up . . . . .	22
Velocity and Pressure Measurements . . . . .	23
Optical Measurements . . . . .	26
Summary . . . . .	38
2.4 1-Foot Turret with Flat Window . . . . .	39
Experimental Set-Up . . . . .	39
Hot-wire Measurements . . . . .	39
Malley Probe Measurements . . . . .	40
Wavefront Measurements . . . . .	40
2.5 4-Inch Cylindrical Turret with Flat Window . . . . .	40
Passive Control Devices . . . . .	42
<b>3 AVUS Code Analysis and Improvement for Aero-Optic Applications</b>	<b>44</b>
3.1 Introduction . . . . .	44
3.2 Gradient Estimation . . . . .	44
Un-weighted Least Square Gradients . . . . .	44
Weighted Least Square Gradients . . . . .	45
Validation of weighted least square method . . . . .	45
3.3 Summary of Laminar Cylinder Simulations . . . . .	47
3.4 Summary of Turbulent Cylinder Simulations . . . . .	50
Computational Domain and Grids . . . . .	50
Results . . . . .	51
Effect of Turbulence Model on Strouhal Number . . . . .	52
Effect of Dimensionality on Strouhal Number . . . . .	53
3.5 Summary of Prolate Spheroid Simulations . . . . .	53
3.6 Summary of Shear Flow Simulations . . . . .	56
Configuration 1 . . . . .	59
Configuration II . . . . .	59
<b>4 Conclusion</b>	<b>62</b>
<b>5 References</b>	<b>63</b>

# List of Figures

1	Shear layer test section geometry . . . . .	2
2	Inlet attached to test section (a) and close up of test section with the flow-measurement turret installed (b). . . . .	4
3	Turret dimensions (left) and location in test section (right). . . . .	4
4	Schematic of the test section showing planes for hot-wire measurements and locations for static pressure measurements (left) and lines along which hot-wire measurements were made in cross section of the test section (right). All dimensions are in inches. . . . .	5
5	Hot wire mounted on the traverse system behind the turret. . . . .	5
6	Profiles of mean (solid line) and fluctuating component (dashed line) of streamwise velocity, normalized by the inlet freestream velocity at three measurement planes; at inlet plane (left), ahead of turret (middle) and behind turret (right). Incoming Mach number = 0.5. . . . .	6
7	Pressure turret instrumented with static pressure ports installed in the test section (left), and location of ports (right). . . . .	7
8	$C_p$ on the turret for different incoming Mach numbers. . . . .	7
9	Local Mach numbers on the turret for different incoming Mach numbers. . . . .	7
10	Unsteady pressure locations on and behind the turret. Dimensions are in inches. . . . .	8
11	Unsteady pressures at and behind the turret as a function of incoming dynamic pressure $q$ . . . . .	8
12	Unsteady pressure spectra for all locations and Mach numbers. . . . .	10
13	Phase difference $S_{2k}(f)$ between all unsteady pressure sensors and the sensor at Location 2. . . . .	11
14	Optical test section with a one of two optical turrets installed. . . . .	12
15	General and schematic view of optical turret for Malley probe set-up. . . . .	13
16	Malley probe set-up. . . . .	14
17	Malley probe phase maps at different elevation angles for $M = 0.5$ . . . . .	15
18	Deflection angle spectra for different elevation angles, $M = 0.5$ . . . . .	16
19	$OPD_{rms}$ for different elevation angles. Solid line represents “ $\approx 1/\sin(\theta)$ ” law. . . . .	17
20	Averaged auto-correlation function of apertured OPD, $M = 0.5$ . . . . .	17
21	Optical set-up to measure 2-D wavefronts. . . . .	18
22	Optical turret for 2-D wavefronts measurement. . . . .	18
23	$OPD_{rms}$ from 2-D measurements (top) and mean removed tilt and tip (bottom) for range of elevation angles and incoming mach numbers. . . . .	20
24	Mean “lensing” wavefronts for range of elevation angles between $40^\circ$ and $140^\circ$ . Incoming $M = 0.5$ . Flow direction is from left to right. . . . .	21
25	Left: Turret is mounted on the back side of the tunnel. Right: Dimensional drawing of the tunnel’s cross-section with the mounted turret. . . . .	22
26	Turret-based system of coordinates and locations of unsteady pressure sensors. . . . .	23
27	Locations of velocity profile measurement stations. . . . .	23
28	Mean (blue line) and RMS (red line) velocity profiles at Location 1 ( $x = -17''$ , $y = 0''$ ) . . . . .	24
29	Normalized mean (blue line) and RMS (red line) velocity profiles at locations downstream of the turret. $U_{normalized} = U_\infty = 137m/sec$ , $H = 10.5''$ . . . . .	25
30	Normalized static pressures along the line of zero-degree azimuthal angle. . . . .	26
31	Unsteady pressure spectra for different sensors for several Mach numbers as a function of frequency. . . . .	27
32	Unsteady pressure spectra for different sensors for several Mach numbers as a function of $St_D = fD/U_\infty$ . . . . .	27
33	Optical components inside the turret. . . . .	28
34	Turret’s system of coordinates for optical measurements. . . . .	28
35	Malley probe optical set-up. . . . .	29
36	Deflection angle spectra for different elevation angles, $M = 0.4$ . . . . .	30
37	Phase plots $\arg[S(f)]$ for different elevation angles, $M = 0.4$ . . . . .	31
38	Convective speeds of optical structures from Malley probe. . . . .	32
39	2-D Wavefront Set-Up. . . . .	32
40	$OPD_{rms}$ from WaveFront and Malley probe measurements. . . . .	33

41	Selected wavefronts for 76, 90 and 132 degrees, $M = 0.4$ . Flow goes from left to right. . . . .	34
42	Temporal variations of wavefronts over the aperture, $M = 0.4$ . . . . .	35
43	$8 \times 8$ Wavefront sensor. . . . .	35
44	$8 \times 8$ wavefront sensor optical set-up. . . . .	36
45	Temporal evolution of $OPD_{rms}$ from $8 \times 8$ sensor for 120 degree (left) and 132 degree (right) cases, $M = 0.4$ . . . . .	37
46	$OPD_{rms}$ for different elevation angles for all measurement devices. . . . .	37
47	Flow topology around the conformal-window turret. . . . .	38
48	Test section schematic (dimension in inches). . . . .	39
49	Turret orientation and measurement locations . . . . .	40
50	2-dimensional turret . . . . .	41
51	Optical set-up to measure 2-D wavefronts . . . . .	41
52	Flow control devices . . . . .	42
53	BVG arrangements . . . . .	42
54	Sample grid for gradient estimation using least square approach . . . . .	44
55	Grid used for the transonic flow past NACA0012 airfoil . . . . .	46
56	Comparison of pressure distribution around NACA0012 airfoil for different least square approaches . . . . .	46
57	Comparison of $C_p$ distribution around NACA0012 airfoil for weighted and un-weighted least square approaches . . . . .	47
58	Grids used for the simulation of laminar vortex shedding from a cylinder . . . . .	48
59	Pressure distribution around the cylinder during vortex shedding . . . . .	49
60	Time history of forces acting on the cylinder . . . . .	49
61	Power Spectral Density (PSD) of the vortex shedding . . . . .	50
62	Typical force history for Grids 1-4 and time step of 0.002 seconds . . . . .	51
63	Typical PSD distribution for grids 1-4 and time step of 0.002 seconds . . . . .	52
64	Force history for Grid 4 and time step of 9.1E-05 seconds . . . . .	52
65	Force history for Grid 6 and time step of 9.1E-05 seconds . . . . .	53
66	Lift history for vortex shedding from a circular cylinder . . . . .	53
67	Power spectral density of lift and drag histories . . . . .	54
68	Pictorial representation of the 6:1 prolate spheroid . . . . .	54
69	Configurations and grids used for prolate spheroid simulations . . . . .	55
70	Oil flow pattern for an angle of attack of $10^\circ$ . . . . .	55
71	Oil flow pattern for an angle of attack of $20^\circ$ . . . . .	56
72	Cross flow separation associated with flow over a 6:1 prolate spheroid . . . . .	56
73	Streamline pattern over the spheroid for an angle of attack of $10^\circ$ . . . . .	57
74	Circumferential $C_p$ distribution for an angle of attack of $10^\circ$ . . . . .	57
75	Circumferential $C_p$ distribution for an angle of attack of $20^\circ$ . . . . .	57
76	Geometry for the configuration I for the shear flow simulations . . . . .	57
77	Grid used for configuration I for shear flow simulation . . . . .	58
78	Visualization of the flow field after 400,000 time levels for configuration I . . . . .	59
79	Geometry and grid used for configuration II for shear flow simulation . . . . .	60
80	Results from the simulation of shear layers for configuration II . . . . .	61

## List of Tables

1	Inlet/outlet static pressures at different Mach numbers. . . . .	6
2	Test matrix of optical measurements. . . . .	29
3	Test-section flow parameters . . . . .	39
4	Model parameters . . . . .	39
5	Description of Passive Control Devices . . . . .	43
6	Pressure port locations . . . . .	43
7	Summary of results for the laminar vortex shedding simulations. . . . .	50

8	Summary of grids used and the computed Strouhal numbers for the turbulent vortex shedding simulations. . . . .	51
9	The effect of turbulence models on Strouhal number . . . . .	52
10	Flow parameters for the mixing layer problem (Configuration II) . . . . .	60

## Acknowledgements

The author would like to acknowledge Drs. Eric Jumper and Mark Rennie and their research group at the University of Notre Dame for compiling and providing the experimental datasets. The author would also like to acknowledge Dr. Roy Koomullil of the Department of Mechanical Engineering at the University of Alabama at Birmingham for evaluating and making improvements to AVUS, running the cases and providing the results shown in this report.



# 1 Introduction

This report details the interim progress made under the Aero-Optics Code Development Program managed by the Computational Sciences Branch, AFRL/RBAC. This program is tasked with developing an in-house capability to perform computational analysis of the aero-optical environment associated with configuration of interest to the Air Vehicles Directorate. The progress in the first two years has focused on two main areas: 1) identify and obtain high quality experimental data for various aero-optic configurations to serve as possible validation data for future code development, and 2) evaluate the in-house unstructured flow solver AVUS for use on canonical cases representing the types of problems expected to be encountered in the aerodynamic analysis of future aero-optics configurations and improve the predictive capabilities of the code if feasible.

## 2 Experimental Database

As part of this effort, sets of experimental data corresponding to various configurations of interest were compiled by researchers at the University of Notre Dame. These experimental data sets consisted of a compressible shear layer, a 1.5-inch turret with a conformal window, a 1-foot turret with a conformal window, a 1-foot turret with a flat window, and a 4-inch cylindrical turret with a flat window. These data sets typically consist of both fluid dynamic and aero-optical measurements. In some cases, particularly the conformal turret configurations, the fluid-dynamic and aero-optical data is plotted and interpreted. The material for the remaining cases primarily focuses on the experimental set-up and the data collected with limited interpretation. Due to the large amount of data provided, the raw data corresponding to these sets will not be provided here. If raw data is desired, please contact the Computational Sciences Branch for further guidance on acquiring this data.

### 2.1 Compressible Shear Layer

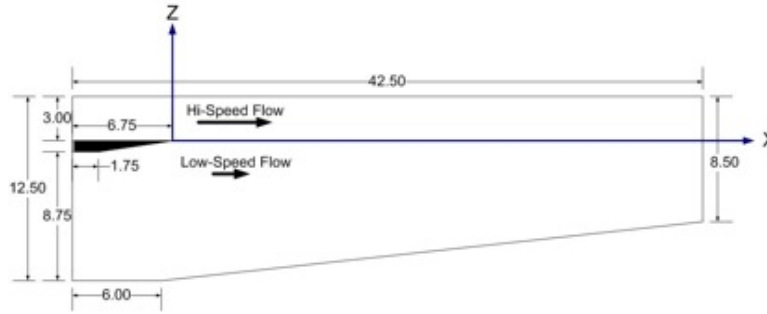


Figure 1: Shear layer test section geometry. All dimensions in inches. Splitter plate shown in black.

#### Experimental Set-Up

The first data set consisted of measurements associated with a compressible shear layer. The tests were performed in a specially-made wind-tunnel test section attached to one of the University of Notre Dame's transonic indraft wind tunnels. The test section is designed to generate a shear layer by mixing high- and low-speed flows at the test-section inlet. Flow enters the high-speed flow side of the test section through a contraction in which the air is assumed to accelerate isentropically from quiescent laboratory air conditions. On the low-speed side, the flow passes through a series of lossy, small-cell honeycomb sections before entering the test section. The honeycomb sections reduce the total pressure (and speed) in the low-speed flow, and the number of sections can be varied to produce different speed ratios in the shear layer. Stagnation properties in the low-speed flow are therefore lower than those in the high-speed flow; however the static pressure at the trailing edge of the splitter is matched across the high- and low-speed flows. As can be seen in Figure 1, the test-section contracts in the flow direction at a constant  $6.3^\circ$  angle. The contraction of the test section maintains a constant static pressure along the length of the test section, which was verified by measurements. The splitter plate at the inlet to the test section was interchangeable, and two types of splitters were tested:

- a plain splitter
- a "forcing" splitter that had voice-coil actuators mounted on the high-speed side of the splitter at the trailing edge. The actuators could be vibrated vertically in the direction perpendicular to the flow direction, and thus used to force the development of the shear layer.

#### Pressure Measurements

Two data sets consisting of both static and total pressure measurements were acquired using a single pitot-static probe traversed vertically through the shear layer. The first data set was collected 25.4 mm downstream

of the splitter trailing edge (STE), with  $M_{hi} = 0.56$ ,  $M_{low} = 0.056$ , and lab air barometric pressure measured at 29.11 in. Hg. The second data set was collected 310 mm downstream of the STE, with  $M_{hi} = 0.64$ ,  $M_{low} = 0.08$ , and lab air barometric pressure measured at 29.56 in. Hg.

### Hot-Wire Measurements

Hot-wire measurements consisting of mean streamwise velocity and root-mean-squared streamwise velocity fluctuations were collected vertically across the shear layer at a variety of downstream locations for both the “forced” and “unforced” cases. For the unforced case, data was collected at  $M_{hi} = 0.55$  at locations corresponding to 40, 135, 243, 288, 396 and 549 mm downstream of the STE. In the forced case, the shear layer was forced using voice-coil splitter with a 500 Hz forcing frequency. The amplitude of the vertical motions of the voice coil actuator during forcing was approximately 0.72 mm. Hot-wire measurements were collected at  $M_{hi} = 0.53$  and 0.58 at locations 26, 118, 226, 319, and 480 mm downstream from the STE. Unforced hot wire measurements were also collected at these locations for comparison purposes.

### Malley Probe Measurements of OPD

Malley probe measurements of the optical path difference (OPD) were collected for both forced and unforced shear layers. The aperture size was 427 mm, which was approximately twice the dominant structure size for the forced case. Flow conditions were given by  $M_{hi} = 0.78$  and  $M_{low} = 0.12$ , and the forced case was forced at 700 Hz with an amplitude of 0.2 mm. OPD data was collected across the aperture for two beams at locations downstream of the STE corresponding to 172, 281, 374, and 570 mm. Malley probe data consists of 100 independent OPD realizations and is provided along both Malley beams which are separated by 5 mm. In addition, the forced case has averaged OPD data over the 100 instantaneous data sets.

### Instantaneous Wavefronts

Instantaneous wavefront measurements across a 100 mm aperture was collected at  $M_{hi} = 0.78$  and  $M_{lo} = 0.12$  for both unforced and forced cases. For the forced case, the shear layer was forced at 800 Hz with an amplitude of 0.15 mm. A set of 100 independent realizations was provided at various phase angles that were used for phase-locking of the wavefront measurements to the forcing signal. Data at phase angles ranging from 30° to 330° in increments of 30° was collected as well as for the unforced case.

## 2.2 1.5-Inch Turret with Conformal Window

### Experimental Set-Up

All of the wind tunnel tests were performed in a specially-made wind tunnel section attached to one of Notre Dame’s three transonic in-draft wind tunnels located in the Hessert Laboratory. The tunnel section consisted of a 20:1 contraction inlet and the test section measured 12.65 cm × 14.41 cm by 81.28 cm in length. The diffuser joined to a large gated plenum. The plenum is pumped to low pressure by up to three Allis-Chalmers 3,310 CFM vacuum pumps. By selecting the proper valve settings, the tunnel could be run by one, two or three pumps; the present experiments used either one or two pumps depending on the specific Mach number being used for the tests.

Six nominally-identically-shaped turret test fixtures were designed and manufactured for these tests; the turrets could be interchanged depending on the specific test being run. The nozzle and the test section and a close-up of the flow-measurement turret installed are shown in Figure 2. Each of three turrets designed and constructed for these tests had the same nominal dimensions shown in Figure 3. These turrets, when tested, were located at the centerline of the test section and located axially as shown in Figure 3. All dimensions are shown in inches. Also shown in the test section figure are the planes where velocity data was taken (inlet plane and two comparison planes) and where the static pressure was measured (outlet plane). For the velocity data, Figure 4 shows the profiles where the velocity data was taken in the cross-section of the test section.

Some data regarding the tunnel test is given below:

- Model: Hemisphere-on-Cylinder Turret,  $D = 1.5''$ ,  $H = 0.45''$ ,  $H/D = 0.8$

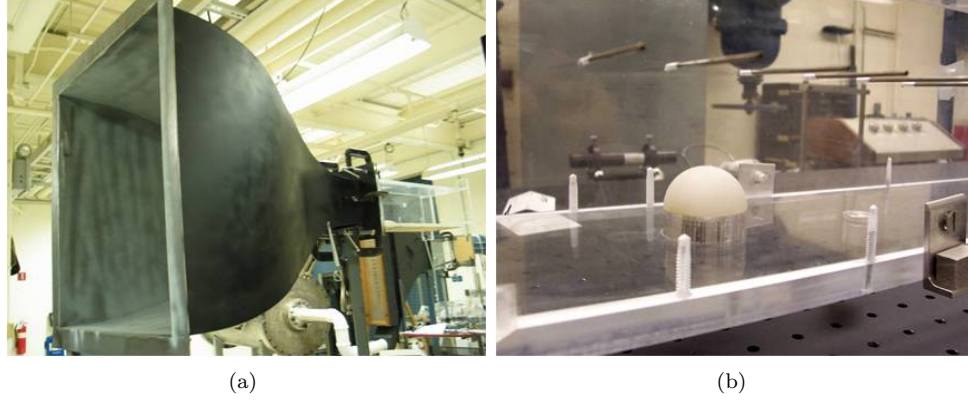


Figure 2: Inlet attached to test section (a) and close up of test section with the flow-measurement turret installed (b).

- Tunnel Elevation: 750 ft
- Total density:  $1.20 \text{ kg/m}^3$
- Mach numbers tested: 0.36 through 0.7
- Reynolds number based on diameter: 0.3 through 0.6 million
- Boundary layer thickness/D:  $\approx 0.2$
- Model blockage: 5.5%

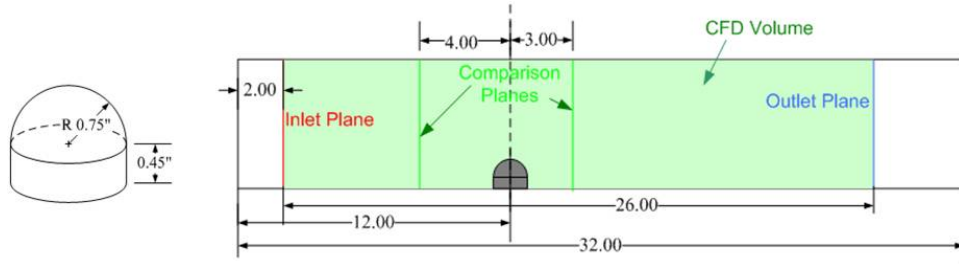


Figure 3: Turret dimensions (left) and location in test section (right).

### Velocity and Pressure Measurements

In order to provide boundary conditions for calculating the flow around the turret, inlet and outlet conditions were measured on the inlet and outlet planes shown in Figure 3 and shown again in Figure 4. In the inlet plane, located 10 inches upstream of the turret, five velocity profiles were taken along lines shown on the right in Figure 4. Two additional velocity profiles were measured along single, vertical center lines at the comparison planes 4 inches upstream and 3 inches downstream of the turret, see Figure 4. In addition to measuring the static pressure in the walls of the tunnel at the inlet and outlet planes, static pressure was also measured at the locations indicated in Figure 4.

*Velocity profiles.* A single-wire, Dantec hot-wire was used to obtain u-component velocity profiles in the inlet and comparison planes. The hot wire was used in conjunction with a commercial IFA-100 anemometer unit with a built in low pass filter. The signal was anti-alias filtered at 40 kHz, and the sampling frequency was 100 kHz. The probe was calibrated in the mean flow (in the middle of the test section) at several Mach numbers ranging from 0.2 to 0.6. Boundary layer mean and rms velocity profiles were measured at

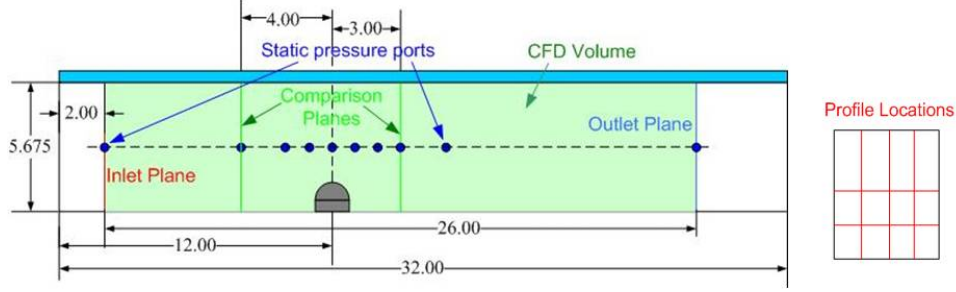


Figure 4: Schematic of the test section showing planes for hot-wire measurements and locations for static pressure measurements (left) and lines along which hot-wire measurements were made in cross section of the test section (right). All dimensions are in inches.

one incoming Mach number  $M = 0.5$ . Voltage from IFA-100 system was acquired using an A/D system which was able to simultaneously sample up to 16 channels of data at 2 MHz with no detectable lag between channels. As discussed in the beginning of this report, in addition to these Mach 0.5 data, originally velocity data at 0.36 and 0.68 Mach numbers were planned; however, at Mach 0.68 hot-wire calibrations are unreliable because of the onset of shocks on the hot wires; thus, no velocity data was taken at Mach 0.68. Further, because the aero-optical data at Mach 0.36 was unusable, velocity data for Mach 0.36 was originally delayed.

In taking the hot-wire data, the probe was mounted on a traverse system (see Figure 5) in order to measure streamwise velocity time series in the wall normal direction at 7 locations: along 5 lines on the inlet plane (see right-hand side of Figure 4) and 2 lines at both comparison planes. Mean and fluctuation profiles were computed at each location. Three example velocity profiles, one in the inlet plane and in two comparison planes are shown in Figure 6, for the incoming Mach number of 0.5. Flow at the inlet plane, Figure 6(a), is uniform across the plane, except in the boundary layer region, approximately 7 mm thick near the wall. The boundary layer grows downstream and at the location of the first comparison plane, 4 inches upstream of the turret, is 10 mm thick as shown in Figure 6(b). Flow separates behind the turret and by the second comparison plane, 3 inches downstream of the turret, exhibits high levels of turbulence, up to 25 % of the free-stream speed, and a significant velocity deficit in the mean velocity profile is present, as shown in Figure 6. Note that at this location the velocity in the free stream is higher than the inlet freestream velocity because of the turret blockage.

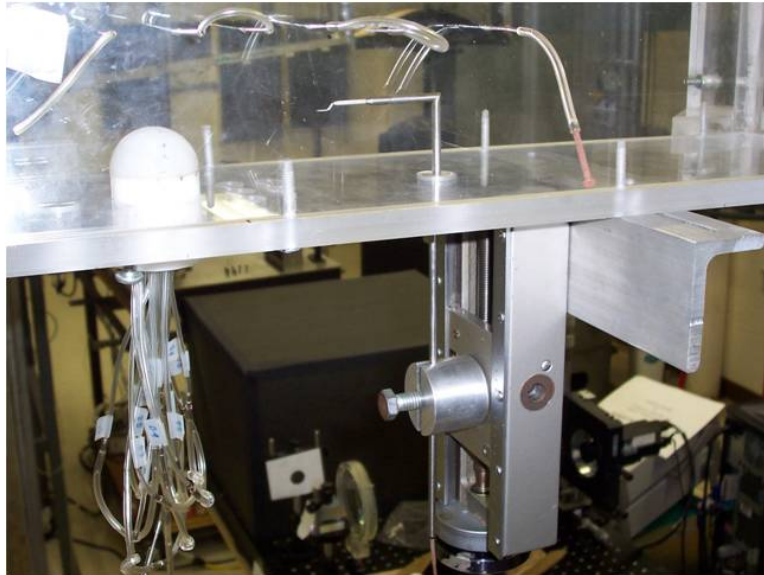


Figure 5: Hot wire mounted on the traverse system behind the turret.

Incoming $M$	0.36	0.5	0.6	0.66
Inlet pressure (in Hg)	27.35	23.20	23.45	22.35
Outlet pressure (in Hg)	26.95	24.30	21.75	19.75

Table 1: Inlet/outlet static pressures at different Mach numbers.

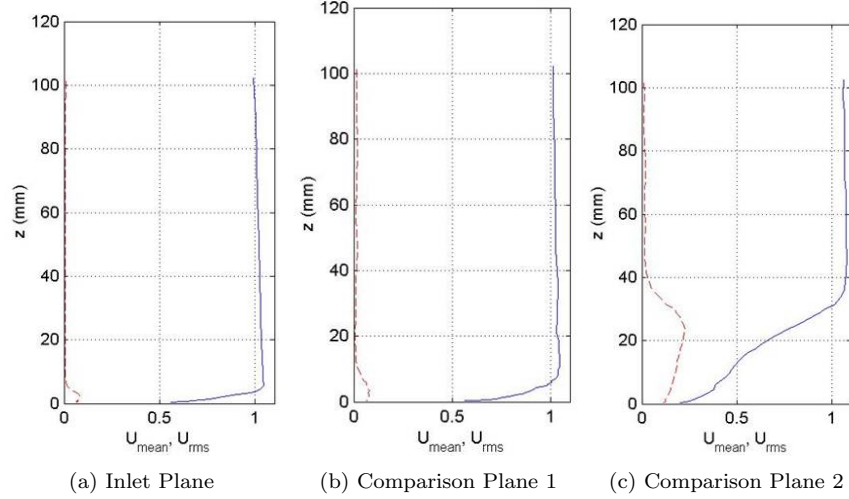


Figure 6: Profiles of mean (solid line) and fluctuating component (dashed line) of streamwise velocity, normalized by the inlet freestream velocity at three measurement planes; at inlet plane (left), ahead of turret (middle) and behind turret (right). Incoming Mach number = 0.5.

*Inlet/outlet pressure:* Static pressure profiles were taken in the inlet and outlet planes using a manometer. Static pressure profiles are fairly uniform (within 1%) in each plane with values for different incoming Mach numbers presented in Table 2.2 ( in inches of Hg ). Experimental accuracy is 0.05 inches of Hg.

*Static pressures on the turret:* In order to measure static pressures on the turret, a second turret was constructed that was instrumented with series of static pressure ports, 12 ports on the hemispherical part of the turret in the streamwise direction (later referred to as the dome) and 7 ports along the hemisphere's base (later referred to as the side wall). Figure 7 shows a photograph of the turret (left) and the locations of all the pressure ports (right). A multi-channel manometer was used to provide static pressure data at different incoming Mach numbers. The pressure coefficient,  $C_p = (p - p_\infty)/(0.5\rho_\infty U_\infty^2)$ , is plotted in Figure 8 as a function of port location on the turret (plot (a) is for the dome ports and plot (b) is for the side-wall ports) for incoming Mach numbers of 0.36, 0.5 and 0.68. These coefficients values indicate that the flow accelerates on the front part of the turret as the static pressure drops on the dome and side wall between  $0^\circ$  and  $80^\circ$ . At  $80^\circ$  the flow reaches its maximum speed as indicated by the pressure coefficients reaching their lowest values. Further downstream (above  $80^\circ$ ) the flow decelerates as the pressure increases until the flow separates at approximately  $100^\circ$  and remains separated further downstream. In the separation region the pressure stays approximately constant at about  $C_p = -0.5$  for  $M = 0.36$  and  $M = 0.5$ . Note that at these Mach numbers the pressure coefficient data collapse onto a single curve.

At  $M = 0.68$  the pressure-coefficient data collapses on the front portion of the turret and flow also separates around  $100^\circ$ , but with lower pressure-coefficient values thereafter, around -0.9 ( see Figure 8). To explain this, local Mach numbers were computed from pressure data assuming the isentropic relationship and results are presented in Figure 9. This figure shows that for the 0.36 and 0.5 incoming Mach numbers the flow remains subsonic everywhere; however for the 0.68 incoming Mach number, the local Mach numbers are subsonic only up to  $\approx 60^\circ$ , after which the Mach numbers are supersonic. The supersonic region persists not from  $60^\circ$  all the way up to the separation point at  $100^\circ$ , where flow separates and the local Mach number drops to just above unity; this indicates that the flow is choked after the turret. It also means that  $M = 0.68$  is the highest reachable incoming Mach number for this test section.

*Unsteady pressure data on and behind turret:* A third turret was manufactured and instrumented with

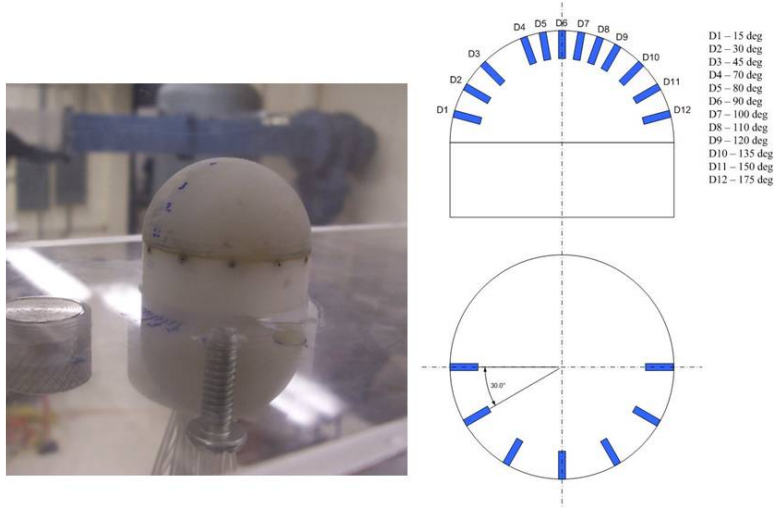


Figure 7: Pressure turret instrumented with static pressure ports installed in the test section (left), and location of ports (right).

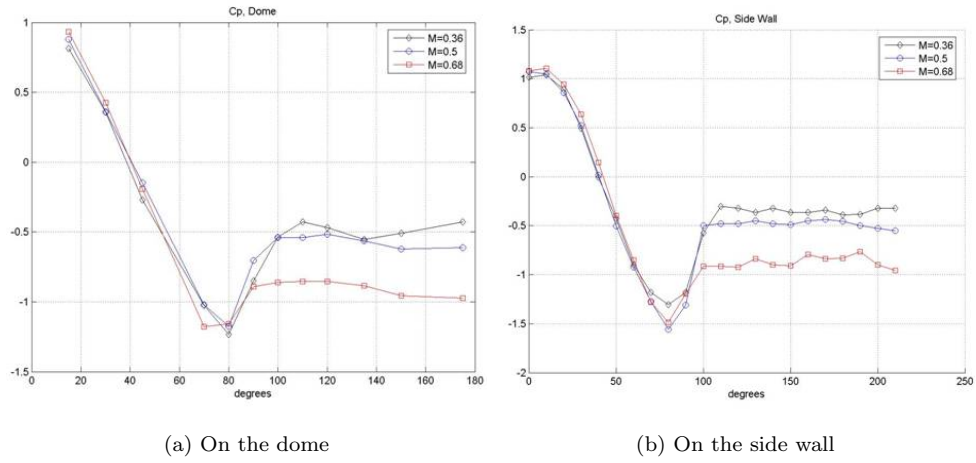


Figure 8:  $C_p$  on the turret for different incoming Mach numbers.

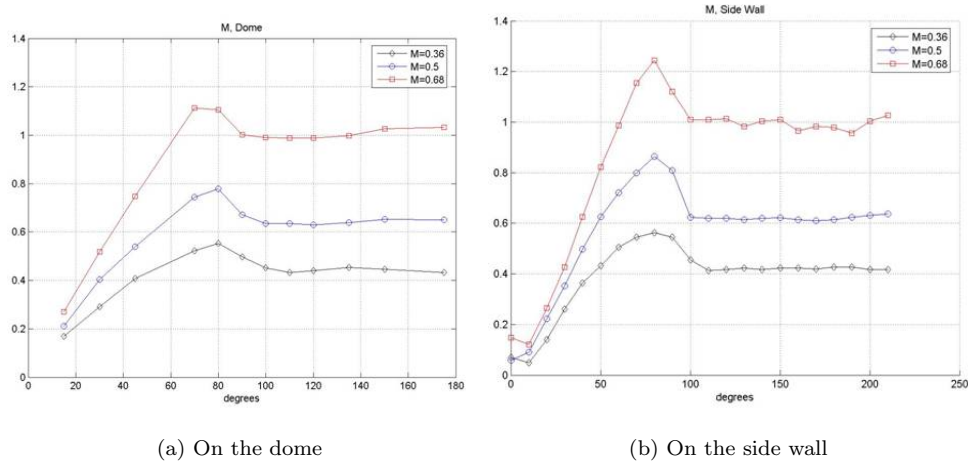


Figure 9: Local Mach numbers on the turret for different incoming Mach numbers.



unsteady Kulite pressure sensor. A total of seven Kulite sensors were placed on the turret and on the test section wall: 3 on the turret and 4 on the wall downstream of the turret, as shown in Figure 10. Sampling rate was 200 kHz per channel. Unsteady pressure measurements were made for four different incoming Mach numbers  $M = 0.36, 0.5, 0.6$  and  $0.67$ . The mean and rms pressure results are given in Figure 11 as a function of incoming dynamic pressure  $q$ , i.e.,  $0.5\rho_\infty U_\infty^2$ . Notice in Figure 11 that the mean values of pressure coefficient at Locations 2 and 3 are  $C_p = -0.4$  and  $-0.5$ , for  $M = 0.36$  and  $0.5$ , respectively, and  $C_p = -0.75$  at  $M = 0.67$ ; these values are consistent with the steady pressure results given in Figure 8. The rms results are shown in Figure 11(b); notice that with the exception of Location 4, which is imbedded in the wake, these rms data exhibit a linear increase with  $q$  for  $M = 0.36 \dots 0.6$ , as would be expected from scaling arguments published elsewhere. This linear trend changes once the flow becomes sonic ( $M = 0.67$ ).

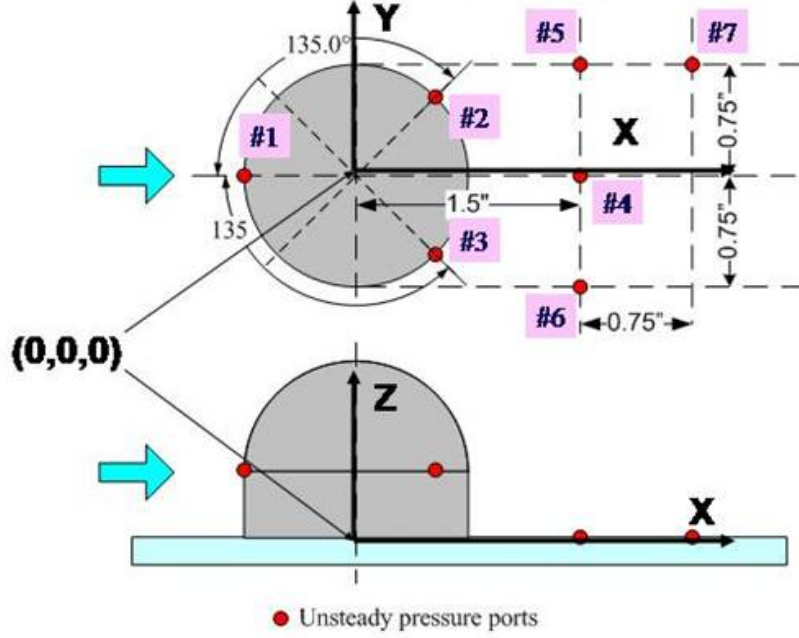


Figure 10: Unsteady pressure locations on and behind the turret. Dimensions are in inches.

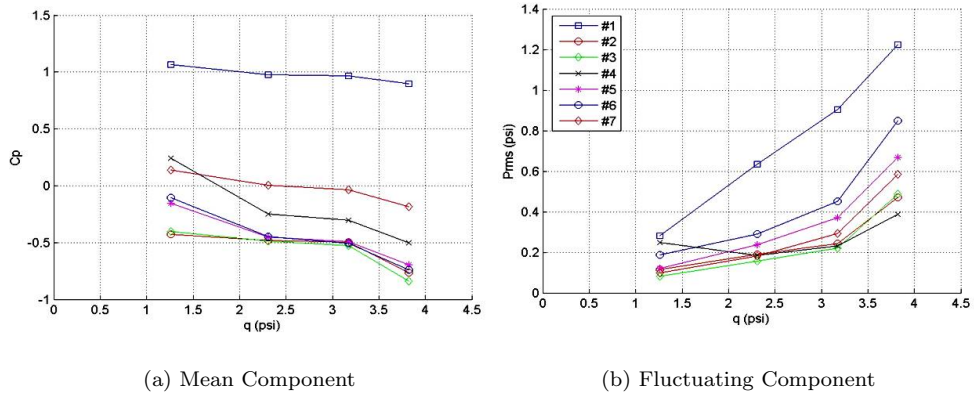


Figure 11: Unsteady pressures at and behind the turret as a function of incoming dynamic pressure  $q$ .

Power spectral density (PSD) results are shown in Figure 12 for all Mach numbers. A broad peak corresponding to the vortex shedding from the turret around 1 kHz is clearly visible at Locations 2, 3, 5, 6 and 7 for  $M = 0.5, 0.6$  and  $0.67$ . The peak frequency is increasing with Mach number, as expected for a



von Karman-like wake with at Strouhal number of  $\approx 0.2$ . Note the considerable low frequency fluctuations at Location 1, which is related to the dynamics of the unsteady recirculation “horseshoe head” structure in the front of the turret. An example of phase correlations,  $\arg[S_{2k}(f)], S(2k) = \langle \hat{p}_2(f) \cdot \hat{p}_k(f) \rangle$ , between the Location 2 sensor and all other sensors for  $M = 0.5$  is shown in Figure 13. There is a strong correlation of a convective nature between Location 2 and Locations 5 and 7. This results from a train of shed vortices at one side of the turret passing by/over all the other locations. Also one can observe an out-of phase correlation at the opposite sides of the turret (Locations 2 and 3, for example) for frequencies below 4 kHz, which corresponds to an alternating, von Karman-like, natural vortex shedding mechanism on the turret. Also note a weak, but definite convective correlation between Location 2 and Location 1, corresponding to the horseshoe vortex formed in the front of turret and convecting downstream around it.

## Optical Measurements

The test section described earlier was modified by replacing the upper wall with a relatively-good optical-quality glass. The test section with the optical-glass wall and one of three optical turrets installed is shown in Figure 14. The first of three optical turrets was manufactured and used to obtain Malley probe data. The Malley-probe-configured turret is shown in Figure 15; the range of elevation angles for this turret was between  $35^\circ$  and  $145^\circ$ .

*Malley Probe results:* The Malley-probe optical set-up is shown in Figure 16. A small, 1 mm diameter laser beam is split into two parallel laser beams spaced by 4 mm. Using two steering mirrors, the two beams are directed in and out of the optical turret. A returning mirror reflects beams exactly along the same optical path back to the optical table, which doubles an optical signal. The returning beams are split at the optical bench by using a beam splitter and passed each beam through focusing lenses onto Position Sensing Devices (PSD). The PSDs measure each beam instantaneous deflection angles, which are digitally acquired at with a 200 kHz sampling rate by a computer for post-processing analysis, outlined as follows:

1. Measure streamwise deflection angles  $\theta_1(t)$  and  $\theta_2(t)$ .
2. Remove vibration contamination by analyzing phase maps of  $\arg[S(f)]$ , where  $S(f) = \langle \hat{\theta}_1(f) \cdot \hat{\theta}_2(f) \rangle$  - cross-spectral function.
3. Calculate convective speeds  $U_c$ .
4. Calculate OPD(t) series assuming frozen-flow hypothesis,  $OPD(t) = -U_c \int \theta_1(t)dt$ .
5. Calculate correlation lengths  $L$ .
6. Apply aperture  $A_p$  to OPD(t) results, remove instantaneous tilt component from each apertured slice and calculate residual  $OPD_{rms}$  for a given aperture and range of elevation angles.

Phase maps (defined in bullet 2 above) for incoming  $M = 0.5$  are shown in Figure 17. The phase shift between two laser beams is zero for frequencies below 1 kHz, indicating the presence of in-phase tunnel vibrations; they were filtered out from both signals. Above 1 kHz the phase exhibits a linear variation with frequency, indicating convecting structures at these scales. The phase slope is proportional to a convecting time delay, which gives a convective speed of structures  $U_c = \Delta/\tau$ , where  $\Delta = 4mm$  is the separation between beams in the streamwise direction. A linear curve fit is presented in Figure 16 as a green line and calculated convective speeds are presented on each plot. For a range of backward-looking elevation angles between  $90^\circ$  and  $145^\circ$  the convective speed is approximately 200 m/sec for the incoming  $M = 0.5$ , or is roughly 80 % of the local freestream speed on top of the turret. A complex flow behavior with a possible reverse flow (negative phase slopes) can be observed for elevation angles  $90^\circ$ ,  $100^\circ$  and  $110^\circ$  for the frequencies 1 to 15 kHz. This is due to an unsteady separation line situated over the aperture at these angles. For elevation angles greater than 120 degrees the separation line is located upstream of the optical aperture and beams go through a separated shear layer. The phase plots indicate the same convective speeds for a wide range of frequencies between 5 and 35 kHz.

Deflection angle power spectra are presented in Figure 18. Tunnel vibrations are present below 0.5 kHz as a series of peaks. A broad peak at 1 kHz and it's harmonic at 2 kHz correspond to induced pressure fluctuations from the von Karman-like vortex shedding region behind the turret, shown in Figure 12.

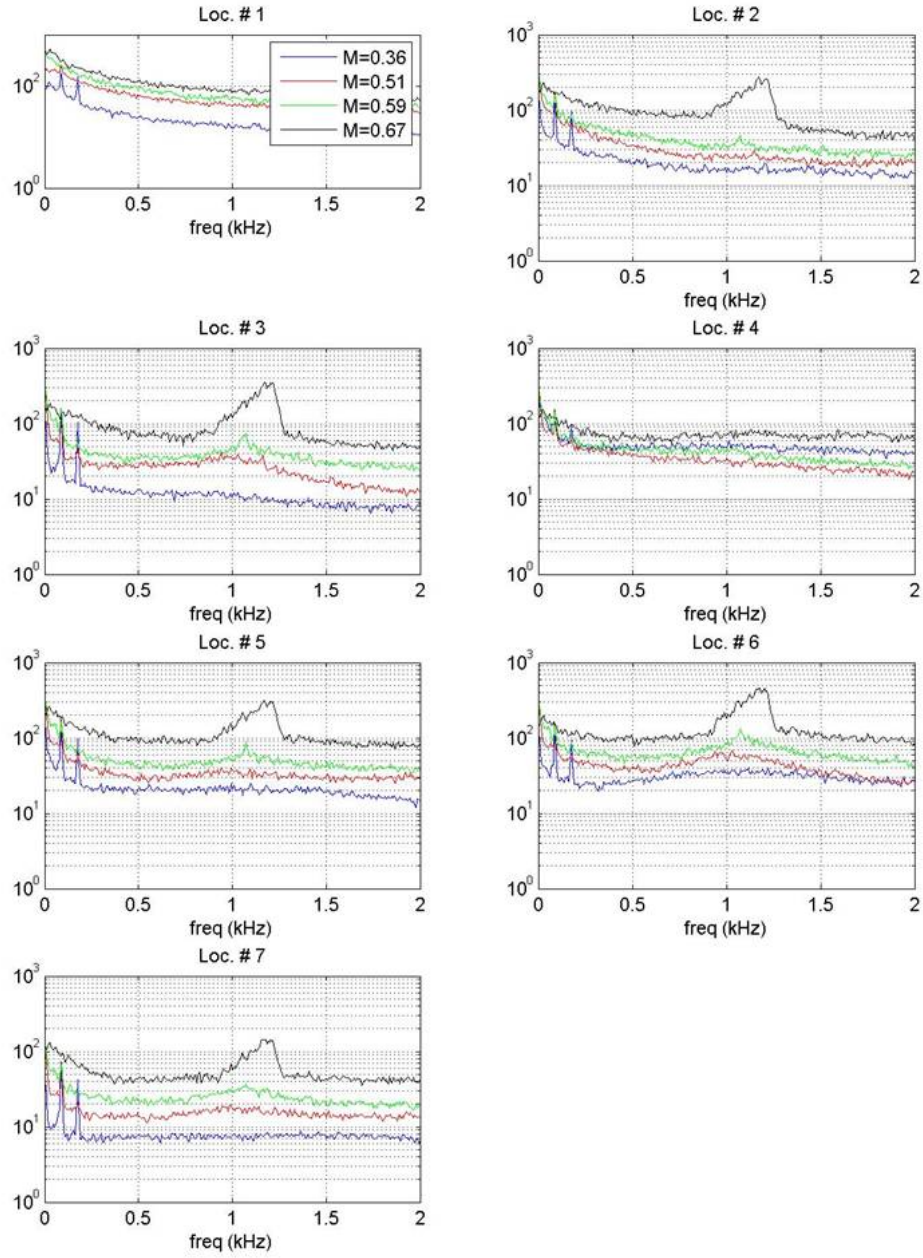


Figure 12: Unsteady pressure spectra for all locations and Mach numbers.

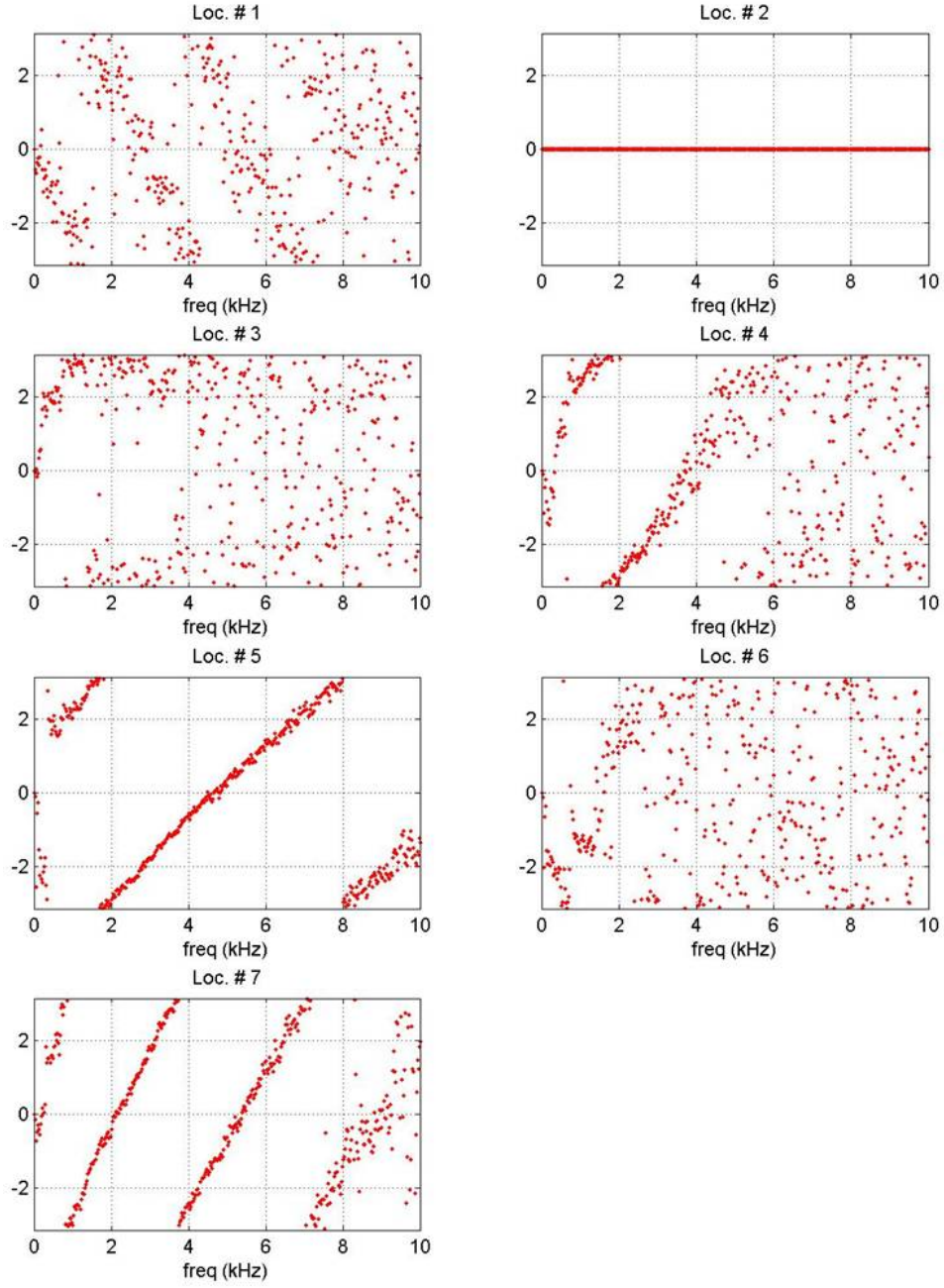


Figure 13: Phase difference  $S_{2k}(f)$  between all unsteady pressure sensors and the sensor at Location 2.

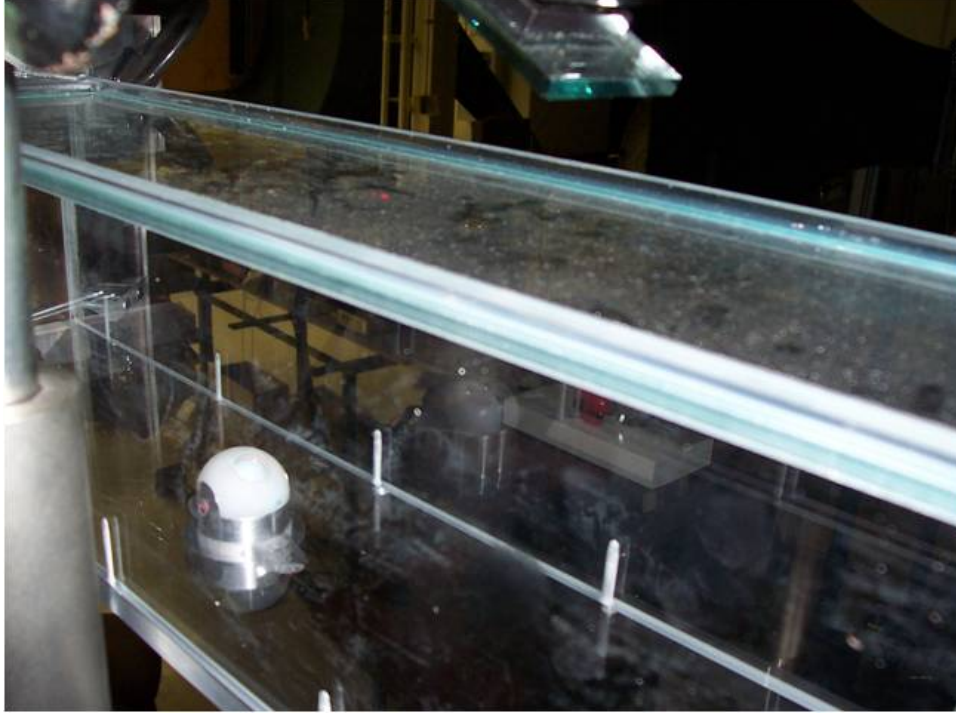


Figure 14: Optical test section with a one of two optical turrets installed.

As mentioned earlier in the Kulite data, the shedding frequency matched fairly well with the theoretical prediction of vortex-shedding frequency behind a 2-D cylinder, which at  $M = 0.5$  yields 850 Hz. A small hump starts appearing at 9 kHz for 145 degree elevation angle, which is due to vortical structures present in the separated shear layer behind the turret. The data indicates that the structures' characteristic sizes are about  $200 \text{ m/sec} / 9000 \text{ Hz} = 2.2 \text{ cm}$ . Also other vortical scales are present up to 40 kHz, as expected for fully turbulent flows. Apertured unsteady  $OPD_{rms}$  are presented in Figure 19, for an aperture size of 12 mm. Optical aberrations are relatively small for "looking-up" elevation angles of  $90^\circ$  and  $100^\circ$ , on an order of 0.01 micron, but start increasing for further look-back angles. A black line represents a theoretically predicted increase in optical aberrations as  $OPD_{rms} \approx 1/\sin(\theta)$ , where  $\theta$  is the elevation angle.

It is worth noting the small absolute numbers for the optical aberrations ( $< 0.03$  microns); this small of aberrations presented a measurement challenge. Even with "a double optical pass" Malley probe set-up, which doubles a signal-to-noise ratio, noise was still present in the data and its amplitude can be inferred from the  $OPD_{rms}$  fluctuations around the theoretical prediction in Figure 19. Assuming optical aberrations increase linearly with a turret size, expected values for  $OPD_{rms}$  for a "one-foot turret" should be in a range of 0.08 - 0.27 microns. For each apertured slice an auto-correlation function was computed and averaged over all apertures as

$$\rho(\Delta x) = \frac{\langle OPD_1(x)OPD_2(x + \Delta x) \rangle}{OPD_{rms}^2}, \quad x = -U_c t \quad (1)$$

The results are plotted in Figure 20 for elevation angles  $90^\circ$  to  $140^\circ$ . All of them collapse on a single curve. A streamwise correlation length defined as a distance between to minima is approximately 7.5 mm or 60 % of the aperture size of 12 mm. It is less than a 22 mm structure size predicted from deflection angle spectra (Figure 18). This can be attributed to aperture effects, which works like a high-frequency filter effectively removing all scales bigger than the aperture size. Detailed analysis of apertured effects can be found in Ref. [1].

*Wavefront Measurements:* Uncorrelated 2D wavefronts across the turret aperture were taken using a CLAS-2D 2-dimensional wavefront system. Pictures of the test section and the optical set-up are presented in Figure 21. A circular laser beam 12 mm in diameter was directed from the optical bench through the

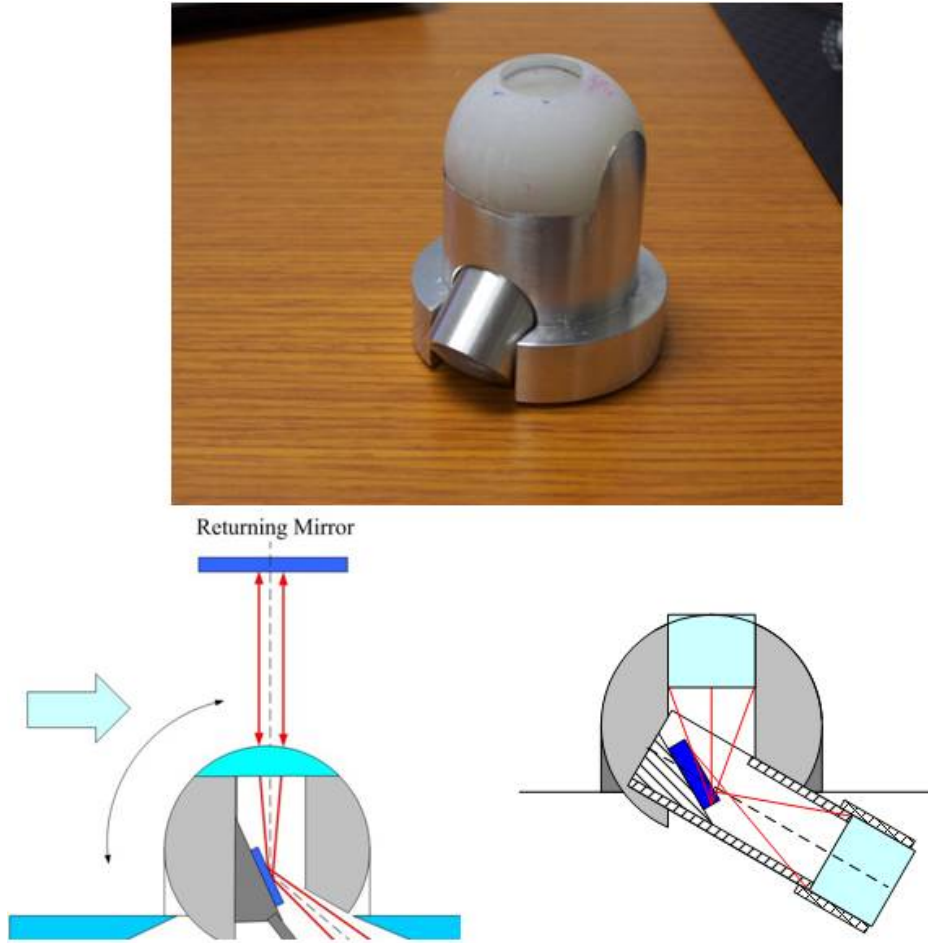


Figure 15: General and schematic view of optical turret for Malley probe set-up.



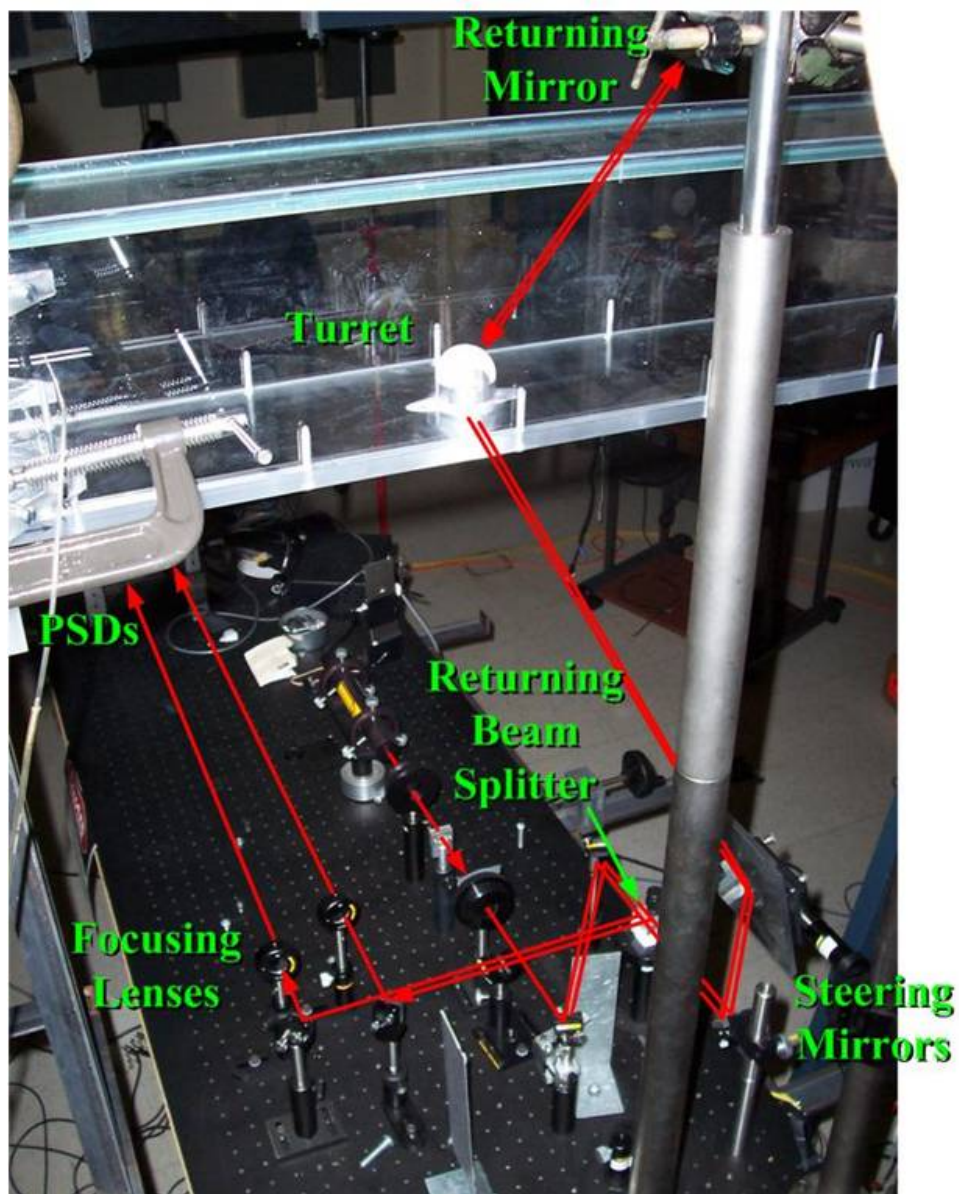


Figure 16: Malley probe set-up.

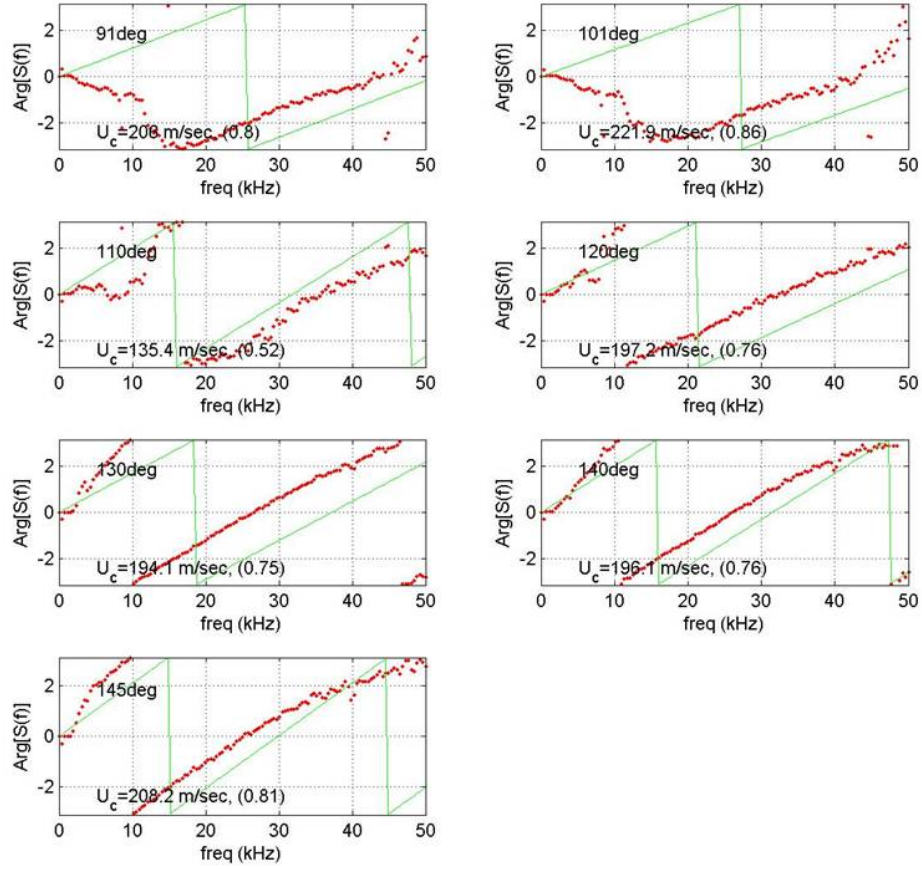


Figure 17: Malley probe phase maps at different elevation angles for  $M = 0.5$ .

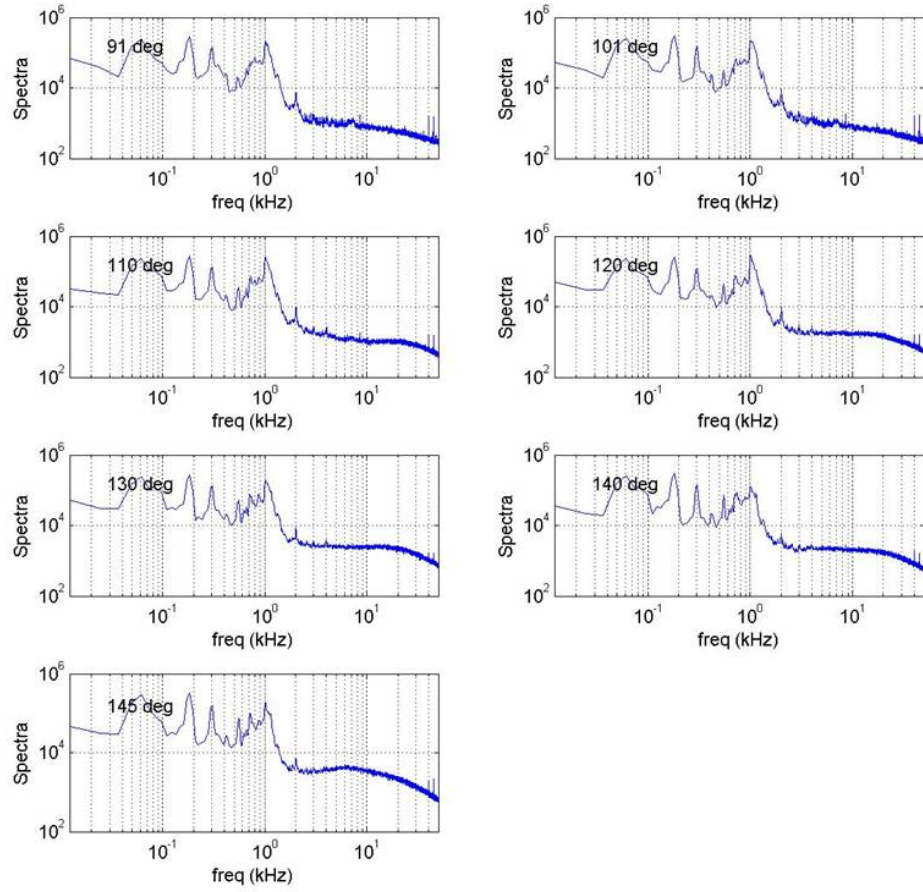


Figure 18: Deflection angle spectra for different elevation angles,  $M = 0.5$ .



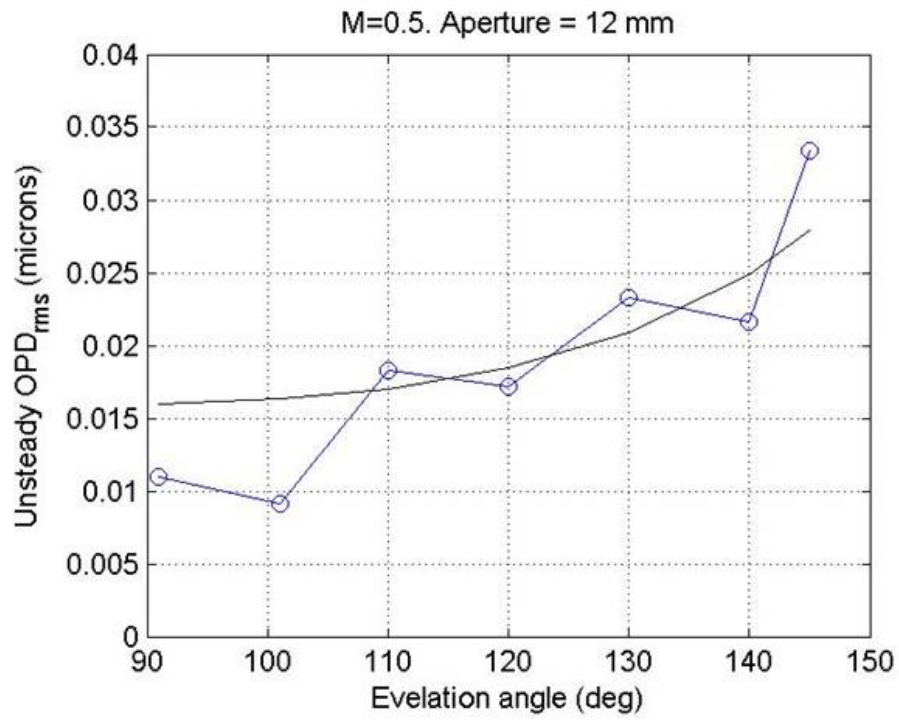


Figure 19:  $OPD_{rms}$  for different elevation angles. Solid line represents " $\approx 1/\sin(\theta)$ " law.

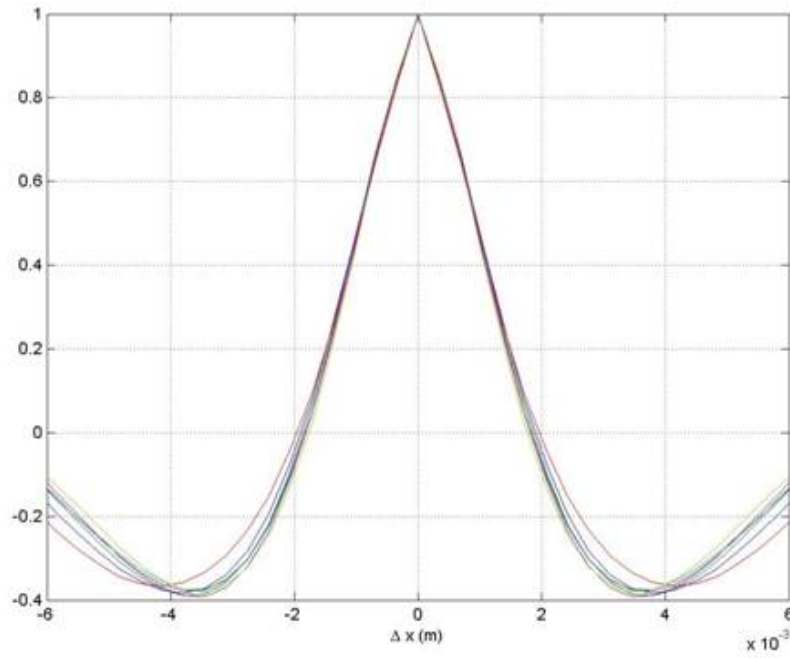


Figure 20: Averaged auto-correlation function of apertured OPD,  $M = 0.5$ .



Figure 21: Optical set-up to measure 2-D wavefronts.

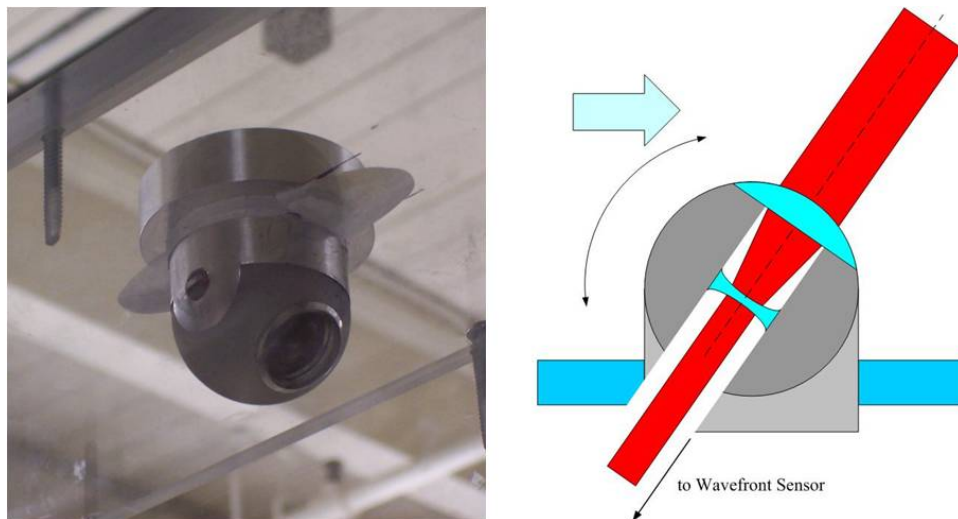


Figure 22: Optical turret for 2-D wavefronts measurement.

turret. A fifth optical turret was manufactured, see Figure 22. Because commercially-available lenses were used, which had some residual aberrations, only a single-beam-pass approach was used to keep the effect of the lens aberrations to a minimum. The beam’s optical distortions were measured using the 2-D Shack-Hartmann wavefront sensor with a  $24 \times 36$  lenselet-array resolution. The wavefronts were made using a pulsed, frequency-doubled Ne-YAG laser with a pulse width of 3 nsec. The wavefronts were sampled at 10 Hz. Two hundred wavefronts were recorded for each elevation angles between  $40^\circ$  and  $140^\circ$  and range of Mach numbers between 0.36 and 0.67. Although the beam diameter was 12 mm, due to significant spherical aberrations imposed by turret lenses only a central, 10 mm-diameter portion was used. The wavefronts for each elevation angle and Mach number were post-processed as follows:

1. A reference "no-flow" wavefront was obtained at the beginning of each run to absorb all non-flow related aberrations imposed on the laser beam and all wavefronts were measured as deviation from this reference wavefronts.
2. Piston and tip/tilt components were removed from each wavefront. Removed tip/tilt was recorded and mean values of removed tip/tilt were calculated.
3. A steady wavefront was computed by averaging among all wavefronts.
4. The steady wavefront was subtracted from each wavefront and spatial  $OPD_{rms}$  was averaged over all wavefronts.

Averaged unsteady components of wavefronts,  $OPD_{rms}$  are presented in the top plot of Figure 23 for a range of elevation angles between  $40^\circ$  and  $140^\circ$  for two incoming Mach numbers of 0.5 and 0.6. Also,  $OPD_{rms}$  from Malley probe data for  $M = 0.5$  is plotted in this figure. Above  $110^\circ$  2D wavefronts and Malley probe data agree fairly well. The 2D wavefronts results indicate slightly larger levels of optical distortion, most probably due to contamination from tunnel vibrations. Remember that these vibrations were effectively removed from Malley probe data.  $OPD_{rms}$  is seen to grow as the square of the incoming Mach number times the freestream density,  $OPD_{rms} \approx M^2 \rho$ , so that the  $M = 0.6$  results are consistently higher, by a factor of  $\approx 1.5$ , than the  $M = 0.5$  results.

The  $OPD_{rms}$  profiles shows a peak around  $90^\circ$ , while Malley probe results do not. The probable explanation for this is that the new optical turret had a metal cylinder around the lenses (see Figure 22). Although the cylinder was flush mounted on the turret as well as possible, it might still have had a small step; such a step is known to cause a separation and reattachment causing the aberrating character of the flow to increase. The small re-circulating separated region and its release into the flow and reformation are known to be responsible for an increased level of optical aberrations. A similar flow topology was discovered over the turret with a flat insert and results and related discussion can be found in Ref. [2].

Although the flow is attached at the front portion of the turret, for forward-looking elevation angles  $OPD_{rms}$  is not zero as may be seen in Figure 23. This is probably due to the presence of the unsteady horse-shoe vortex situated around the bottom portion of the turret. This somewhat-unsteady vortex, while being out-of-sight of the laser beam projected from the turret, still creates unsteady pressure fluctuations on the front portion of the turret via Biot-Savart induction mechanism. This effect is the strongest when the aperture is located close to the horseshoe vortex, at  $40^\circ$ ; although, it is worth noting that the turret had exhibited a higher level of mechanical vibrations at this angle and the value of  $OPD_{rms}$  is probably somewhat over-predicted.

For the same experiments, the mean values of removed tip/tilt are also shown in the bottom part of Figure 23. The label "tilt" corresponds to a mean tilt in the streamwise direction and label "tip" denotes the mean tilt in the cross-stream direction. Since the mean flow has significant pressure gradients in the streamwise direction, the tilt angles are not zero. At the front portion of the turret, the flow accelerates and creates a negative pressure gradient; this causes the beam to be bent forward, thus toward positive tilt angles (at  $70^\circ$ ). At the back of the turret, the flow decelerates and separates, which causes the beam to be tilted downstream (toward negative values) as can be seen in the bottom of Figure 24 for elevation angles above  $90^\circ$ . A small region with negative tilt angles between elevation angles  $40^\circ$  and  $50^\circ$  is probably due to the presence of the separated horseshoe-vortex region sitting at the front bottom of the turret.

Due to the flow symmetry in the cross-direction, the mean tip values were found to be around zero, as expected, except at the two extreme angles of  $40^\circ$  and  $140^\circ$ . This is probably due to mechanical flexing of

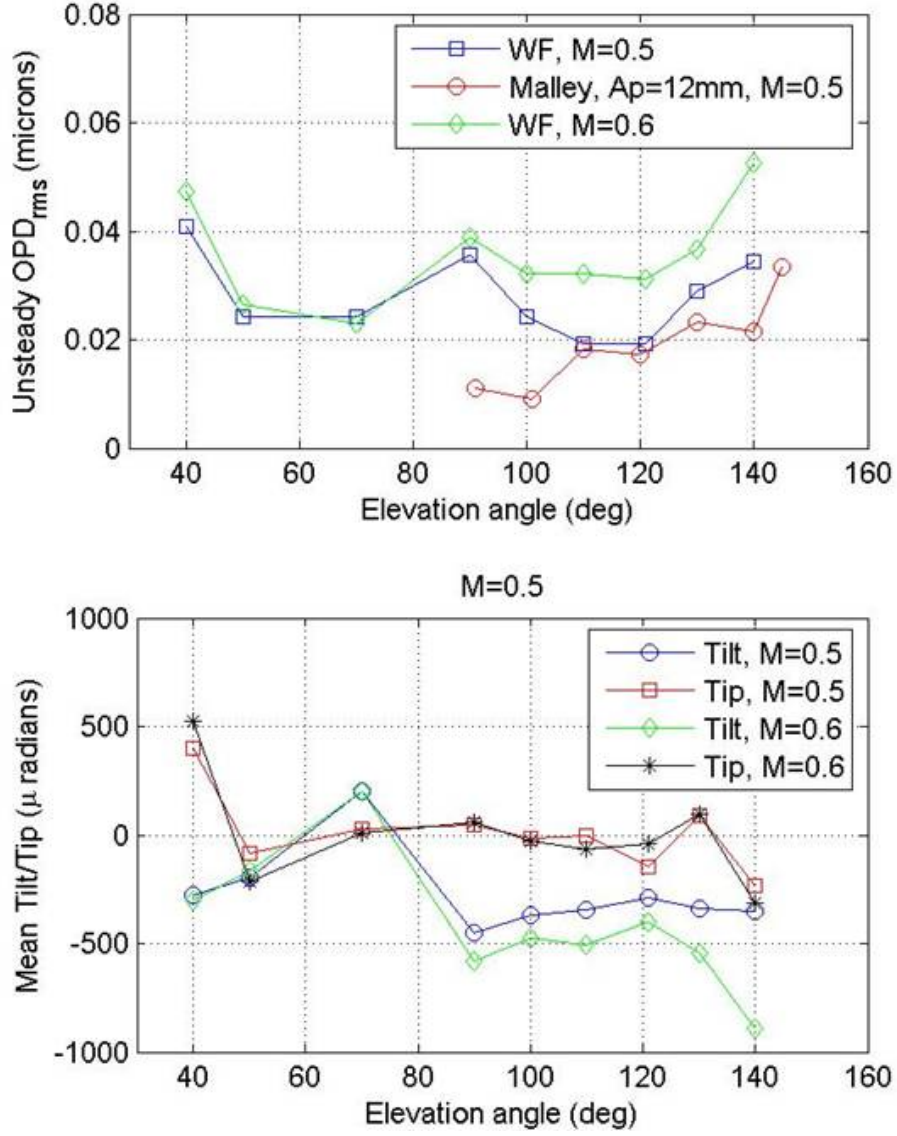


Figure 23:  $OPD_{rms}$  from 2-D measurements (top) and mean removed tilt and tip (bottom) for range of elevation angles and incoming mach numbers.

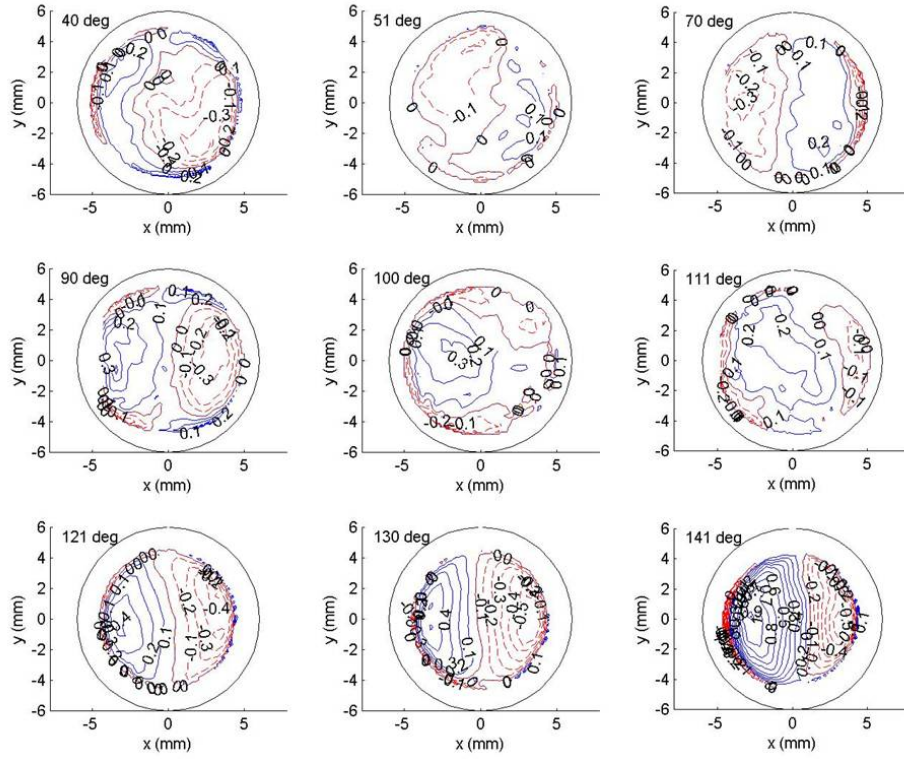


Figure 24: Mean “lensing” wavefronts for range of elevation angles between  $40^\circ$  and  $140^\circ$ . Incoming  $M = 0.5$ . Flow direction is from left to right.

turret, which was noticed while taking data at these angles, since the turret structure was slightly weakened while been modified to accommodate for measurements at these angles. The steady portions of 2-D wavefronts for all observed angles are shown in Figure 24 for the incoming  $M = 0.5$ . It should be remembered that instantaneous tip/tilt has been removed from these wavefronts. These wavefronts demonstrate the “lensing” effects from mean pressure gradients around the turret. Positive values of wavefronts correspond to regions of higher pressure and negative values correspond to regions of lower pressures. The flow direction is from left to right, along the x-axis. The presence of the horse-shoe vortices with a region of lower pressure can be noticed at the far left edge of the wavefront at  $40^\circ$ . The flow then accelerates over the turret, which creates a region of lower pressure, negative wavefront values, seen at angles 50 and 70 degrees. The complex separated region behind the turret can be observed for all other angles above  $90^\circ$ . The mean aberrating effect gets stronger for further back-looking angles, thus increasing gradients in mean wavefronts, as may be seen in Figure 14, at angles  $120^\circ$ ,  $130^\circ$  and  $140^\circ$ .

## 2.3 1-Foot Turret with Conformal Window

### Experimental Set-Up

All experiments were conducted at Subsonic Wind Tunnel at the Air Force Academy, Colorado Springs, Colorado. It has  $3\text{ft} \times 3\text{ft} \times 8\text{ft}$  test section and capable of achieving Mach numbers up to 0.6, although running times at high Mach numbers are relatively short due to bearings overheating. Tested Mach numbers were chosen to be 0.35, 0.4 and 0.45. Wind tunnel tests were conducted on the conformal-window hemisphere-

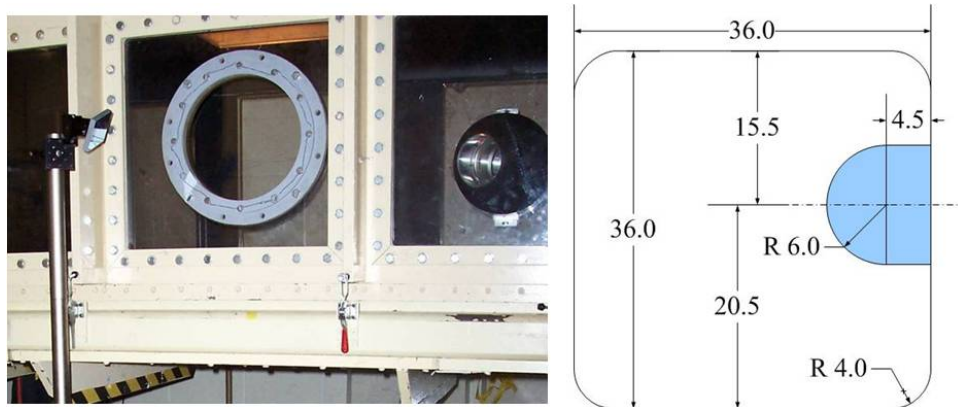


Figure 25: Left: Turret is mounted on the back side of the tunnel. Right: Dimensional drawing of the tunnel's cross-section with the mounted turret.

on-cylinder “turret” model shown mounted on the back wall of the Academy tunnel in Figure 25, left. A cross-sectional dimensional drawing is presented in Figure 25, right. All dimensions are in inches. The turret was placed on the back side of the test section 54” downstream from the beginning of the test section. The 12” diameter turret is composed of a sphere mated to a cylindrical base of 4.5” height. The hollow sphere is made of plastic and re-enforced by adding epoxy material to create a thicker wall. The sphere is fitted with a flush-mounted, positive lens with an outer radius of curvature that matches the 6” curvature of the sphere. Details of the turret configuration will be discussed later. The sphere can be rotated along a vertical axis, as in an overhead pass, thus allowing any elevation angle between  $40^\circ$  and  $140^\circ$ . The cylinder was mounted on a flat plate and can be rotated to any azimuth angle. The open cylinder’s end was sealed with a flat aluminum plate, so that the interior of the beam director was nominally at the test-section static pressure.

The turret was equipped with 10 static pressure ports and 4 Kulite unsteady pressure sensors; 2 mounted on the turret and 2 mounted on the mounting plate downstream of the turret.

Some data regarding the tunnel test is given below:

- Model: Hemisphere-on-Cylinder Turret,  $D=12''$ ,  $H=4.5''$ ,  $H/D = 0.875$



- Elevation: 7,160 ft,  $\rho_o = 0.99 \text{ kg/m}^3$
- Mach number range tested: 0.35 ... 0.45
- Re range based on  $D \approx 2.6 \dots 3.2 \times 10^6$
- Boundary layer thickness/ $D \approx 0.08$
- Model Blockage: 8.5 %

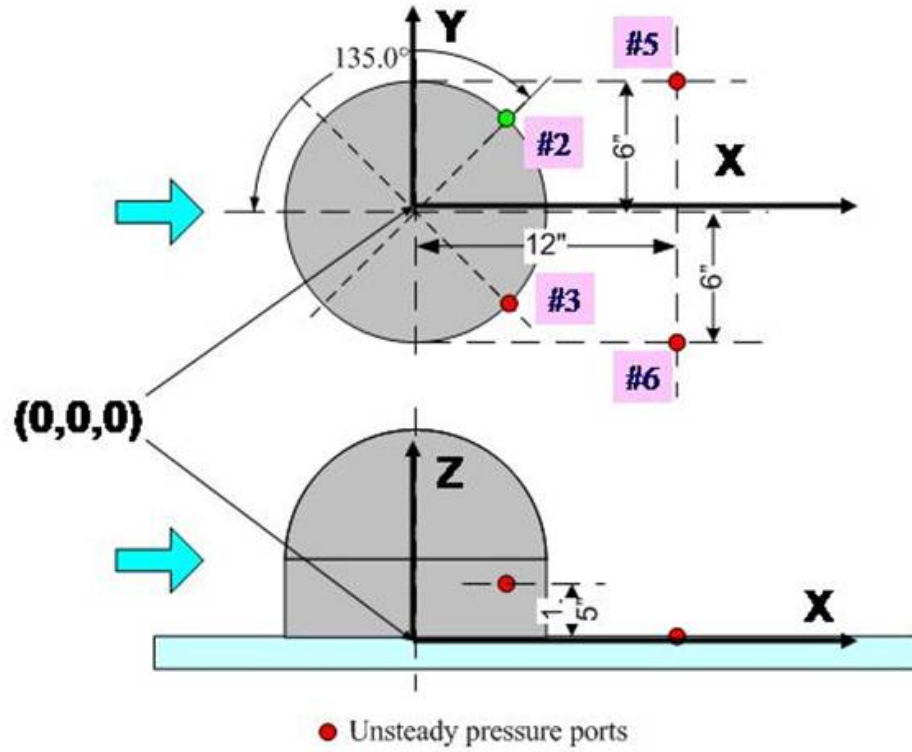


Figure 26: Turret-based system of coordinates and locations of unsteady pressure sensors.

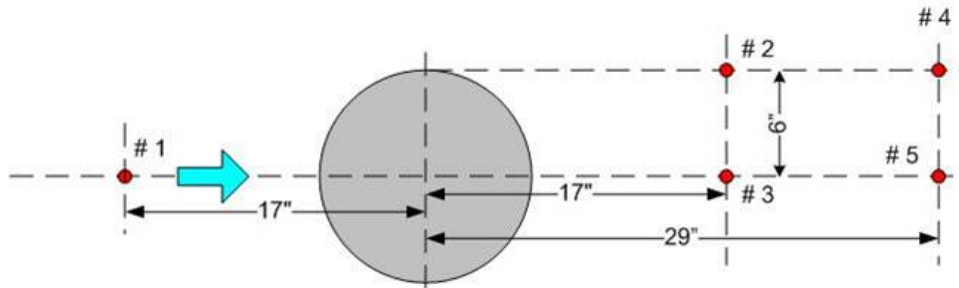


Figure 27: Locations of velocity profile measurement stations.

### Velocity and Pressure Measurements

For all non-optical measurements the turret based system of coordinates was used, see Figure 26.

*Velocity Measurements:* Five profiles of the streamwise component of velocity in the direction normal to the mounting plate (z-direction) were measured using the TSI IFA-100 model. Locations relative to the turret are shown in Figure 27. The sampling rate was 100 kHz with a low-pass filter cut-off at 40 kHz. One million samples were taken at each point. All measurements were performed at Mach number 0.4 only for time constraints reasons.

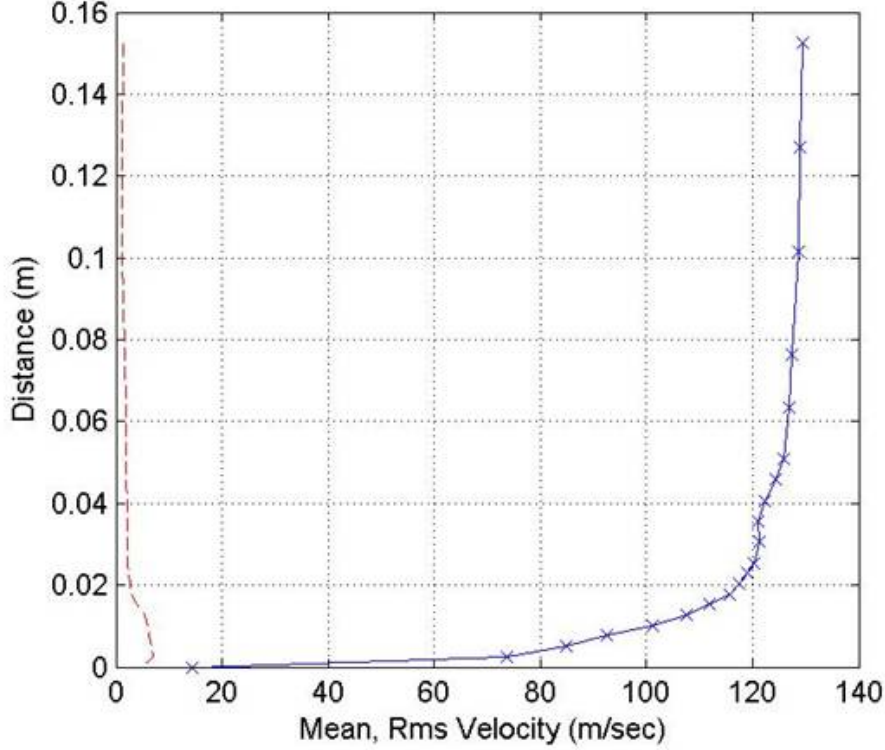


Figure 28: Mean (blue line) and RMS (red line) velocity profiles at Location 1 ( $x = -17''$ ,  $y = 0''$ )

Location 1 upstream of the turret characterizes the incoming boundary layer. Results are presented in Figure 28. The thickness of the boundary layer is approximately 2-2.5 cm, which is consistent with boundary layer measurements conducted in the Subsonic Tunnel using static pressure rake (Ref. [3]).

Velocity profiles for Locations 2, 3, 4 and 5 downstream of the turret are presented in Figure 29. All velocities are normalized by the freestream speed,  $U_\infty = 137$  m/sec, and distances from the wall normalized by the turret height  $H = 10.5''$ . At locations directly behind the turret (Locations 3 and 5), the flow is separated and exhibits shear-layer like profiles with sharp drops in mean velocities and high levels of turbulent intensity,  $u_{rms}/U_\infty \approx 0.2$ , for  $z/H < 0.5$ . Locations 2 and 4 are in the region of the necklace vortex wrapped around the turret and have more boundary-layer-like mean velocity shapes with lower turbulence intensity levels of  $u_{rms}/U_\infty \approx 0.1 - 0.15$ .

*Static Pressure Measurements:* The hemispherical portion of the turret was equipped with a series of static pressure ports one inch apart. Results of static pressure measurements along the turret center-plane (at zero-degree azimuth angle) for different Mach numbers, are presented in Figure 30. The azimuth and elevation angles are defined in Figure 34. An elevation angle of zero degrees corresponds to the upstream direction. Flow stagnates at the bottom of the hemispherical part of the turret (elevation angle of  $0^\circ$ ), accelerates along the front portion of the turret (elevation angles between  $0$  and  $90^\circ$ ), enters the region of an adverse pressure gradient on the back of the turret (elevation angles above  $90^\circ$ ) and eventually separates either after  $120^\circ$  for lower Mach number of 0.3, or  $115^\circ$  for higher Mach numbers of 0.35, 0.4 and 0.45.

*Unsteady pressure measurements:* To characterize the temporal behavior of the wake behind the turret,



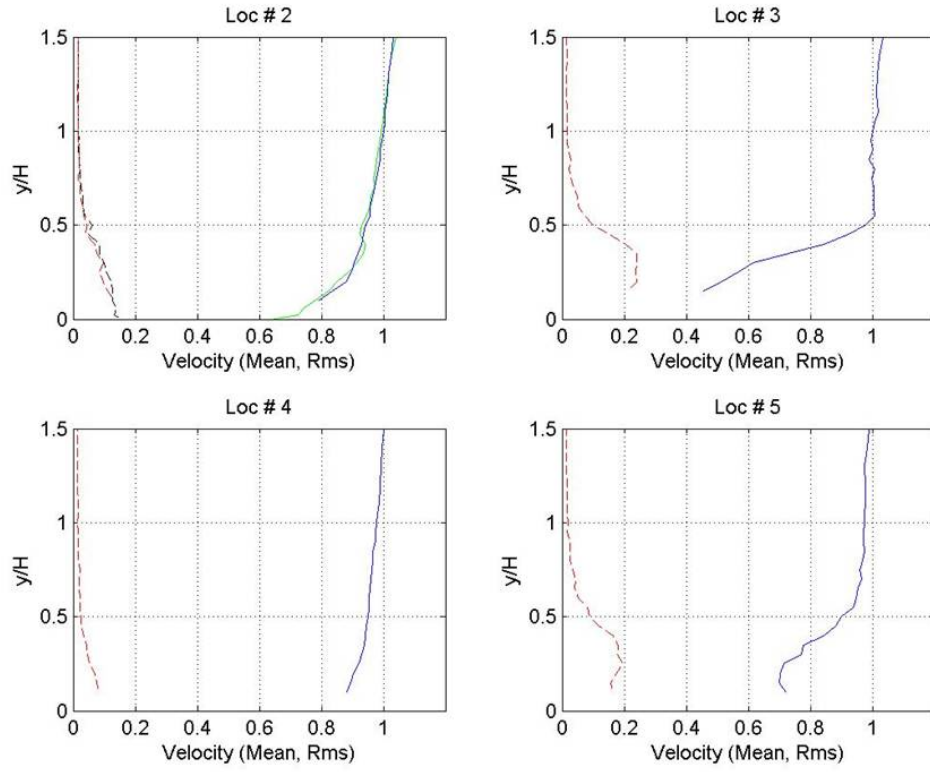


Figure 29: Normalized mean (blue line) and RMS (red line) velocity profiles at locations downstream of the turret.  $U_{normalized} = U_{\infty} = 137m/sec, H = 10.5''$

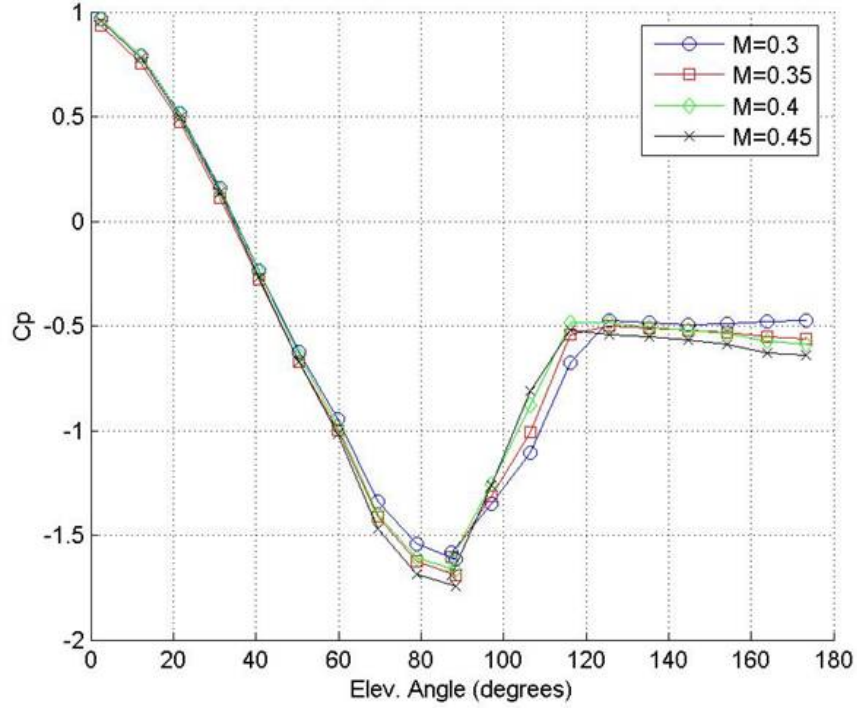


Figure 30: Normalized static pressures along the line of zero-degree azimuthal angle.

four unsteady pressure sensors were placed in the wake. Two sensors (#2 and #3) were placed on the mounting cylinder at azimuth angles of  $\pm 135$  degrees, 1.5" above of the mounting plate. Two other sensors (#5 and #6) were placed at locations with coordinates (12", 6") and (12", -6"), respectively, on the plate downstream of the turret, as shown in Figure 26. Sensor #2 was accidentally damaged during runs, so no data are available from this sensor.

Unsteady pressure power spectra for all three available sensors at different Mach numbers are presented in Figure 31. Pressures in the wake behind the turret (locations 5 and 6) exhibit a broad peak between 0.1 and 0.2 kHz, with increases in magnitude and shifts to higher frequencies with increasing Mach number. A turret-mounted sensor #3 shows the presence of several small broad peaks on the surface of turret. The same data re-plotted in non-dimensional frequencies inferred from the Strouhal number,  $St_D = fD/U_\infty$  are shown in Figure 32. The non-dimensional wake spectra show a single peak at  $St_D = 0.35$ , independent of Mach number.

### Optical Measurements

The turret was equipped with set of lenses and mirrors, which was designed to return a co-axial collimated beam back to the optical bench; see Figure 33. The optical system consists of three elements: a positive lens, a negative lens, and a flat mirror. The positive lens is 6 inches in diameter (5 inch clear aperture) with radius of curvature of 6 inches, mounted flush with the turret surface. The negative lens is mounted on an adjustable platform and is designed to compensate for spherical aberration. The collimated beam passing through the flow, and positive and negative lenses, is reflected from the flat mirror back through the flow, thus increasing the OPD sensitivity by a factor of two. The overall residual wavefront error of the optical system is less than  $\lambda/8$  (for 633 nm) rms.

The beam-director's system of coordinates is shown in Figure 34. The origin is placed at the center of the aperture. Both x- and y-axis are tangent to the center point of the aperture, the x-axis is aligned horizontally and the y-axis is normal to the x-axis. The z-axis is normal to the sphere surface at the center

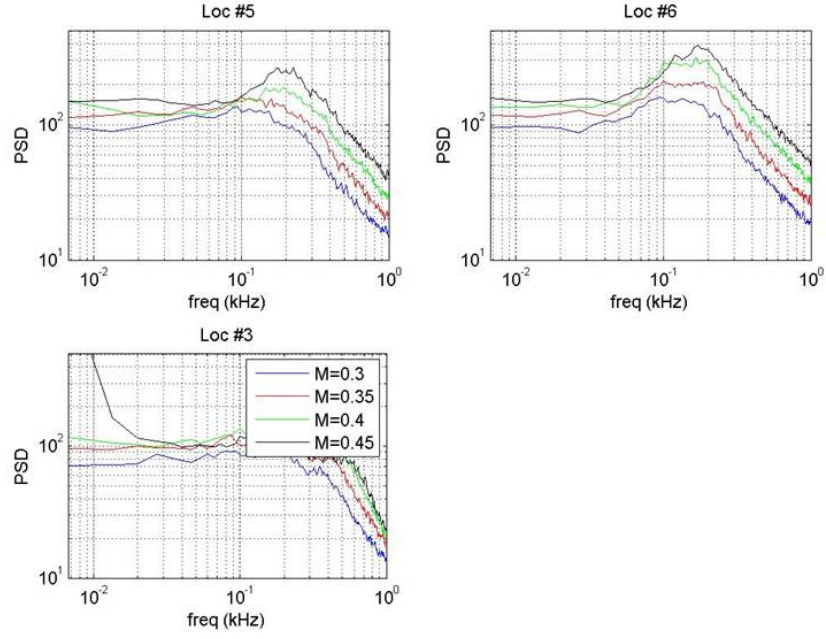


Figure 31: Unsteady pressure spectra for different sensors for several Mach numbers as a function of frequency.

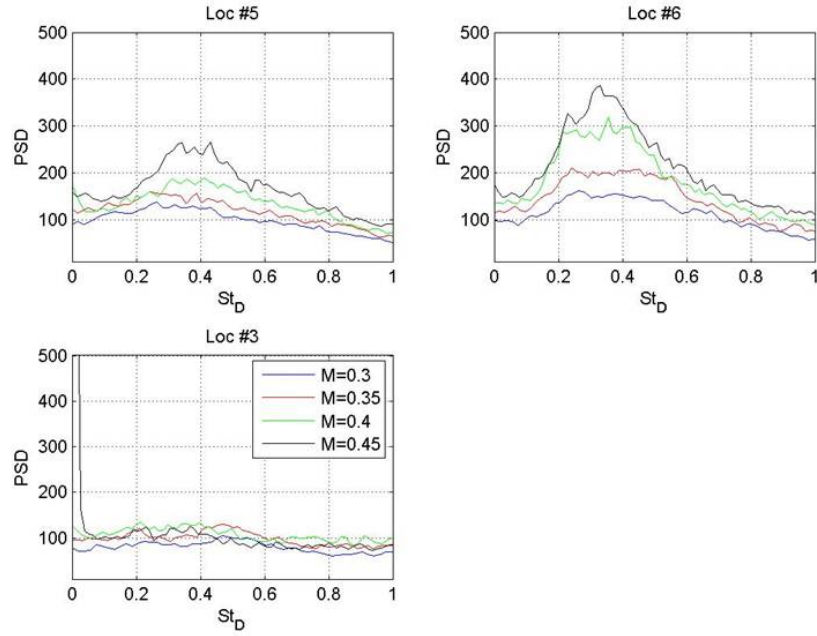


Figure 32: Unsteady pressure spectra for different sensors for several Mach numbers as a function of  $St_D = fD/U_\infty$ .

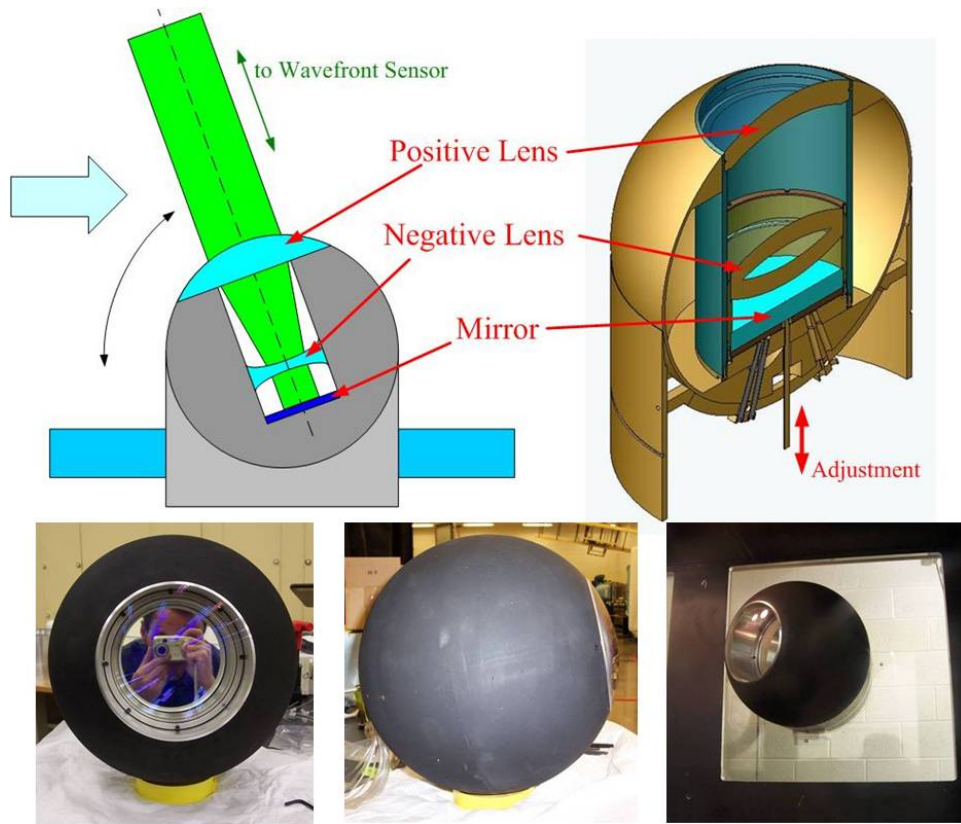


Figure 33: Optical components inside the turret.

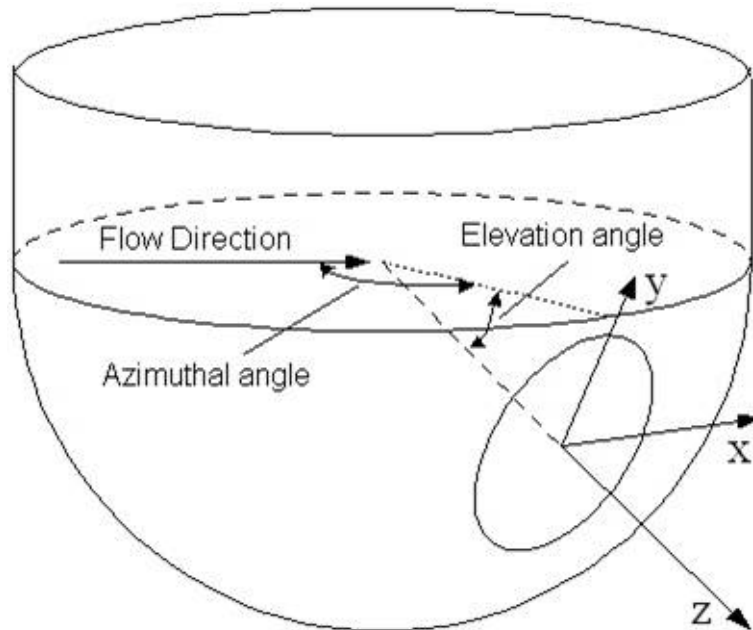


Figure 34: Turret's system of coordinates for optical measurements.

Elevation Angle	Mach numbers	Measurements
45	0.35,0.4,0.45	Malley, WFs
60	0.35,0.4,0.45	Malley, WFs
76	0.35,0.4,0.45	Malley, WFs
90	0.35,0.4,0.45	Malley, WFs
103	0.35,0.4,0.45,0.5	Malley, WFs
120	0.35,0.4,0.45,0.5	Malley, WFs, $8 \times 8$ (no M=0.5)
132	0.35,0.4,0.45,0.5	Malley, WFs, $8 \times 8$ (no M=0.5)

Table 2: Test matrix of optical measurements.

of the aperture.

Three different optical wavefront devices, Malley probe (Malley), conventional wavefront sensor (WFs) and  $8 \times 8$  high-bandwidth wavefront sensor ( $8 \times 8$ ), were used to measure optical aberrations around the turret at a zero azimuthal angle at different elevation angles and Mach numbers. A summary of tested elevation angle and Mach numbers for optical measurements is presented in Table 2.

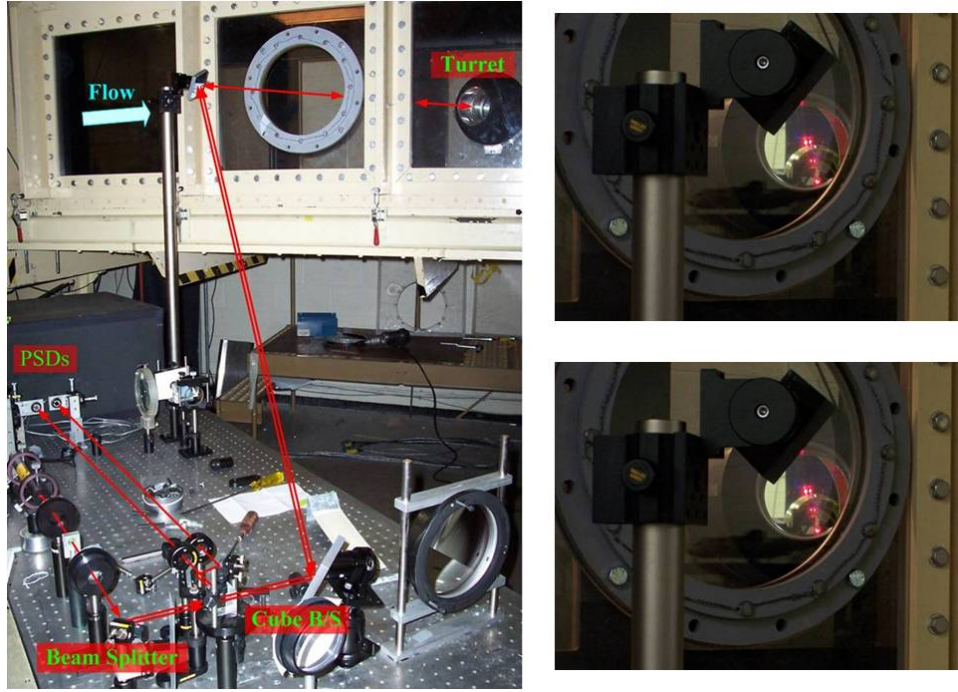


Figure 35: Malley probe optical set-up.

*Malley Probe results* The Malley-probe optical set-up is shown in Figure 35. A small, 1mm diameter laser beam is split into two parallel laser beams spaced by 4 to 5 mm. Using two steering mirrors, the two beams are directed in and out of the optical turret. A mirror reflects the beams exactly along the same optical path back to the optical table, which doubles the wavefront error. The returning beams are split at the optical bench using a cube beam splitter and each beam is passed through a focusing lens onto Position Sensing Devices (PSD). The PSDs measure each beam instantaneous deflection angles, which are digitally acquired at with a 200 kHz sampling rate by a computer for post-processing analysis, outlined below.

1. Measure streamwise deflections angles  $\theta_1(t)$  and  $\theta_2(t)$ .
2. Compute power density spectra for each deflection angle.
3. Compute cross-correlation function  $S(f) = \langle \hat{\theta}_1(f) \cdot \hat{\theta}_2(f) \rangle$  - cross-spectral function.



4. Remove vibration contamination by analyzing phase maps of  $\arg[S(f)]$ .
5. Calculate convective speeds  $U_c$ .
6. Calculate  $OPD(t)$  series assuming a Frozen Field hypothesis,  $OPD(t) = -U_c \int \theta_1(t) dt$ .
7. Apply aperture  $A_p$  to  $OPD(t)$  results, remove instantaneous tilt component from each apertured slice and calculate residual  $OPD_{rms}$  for a given aperture and range of elevation angles and Mach numbers.

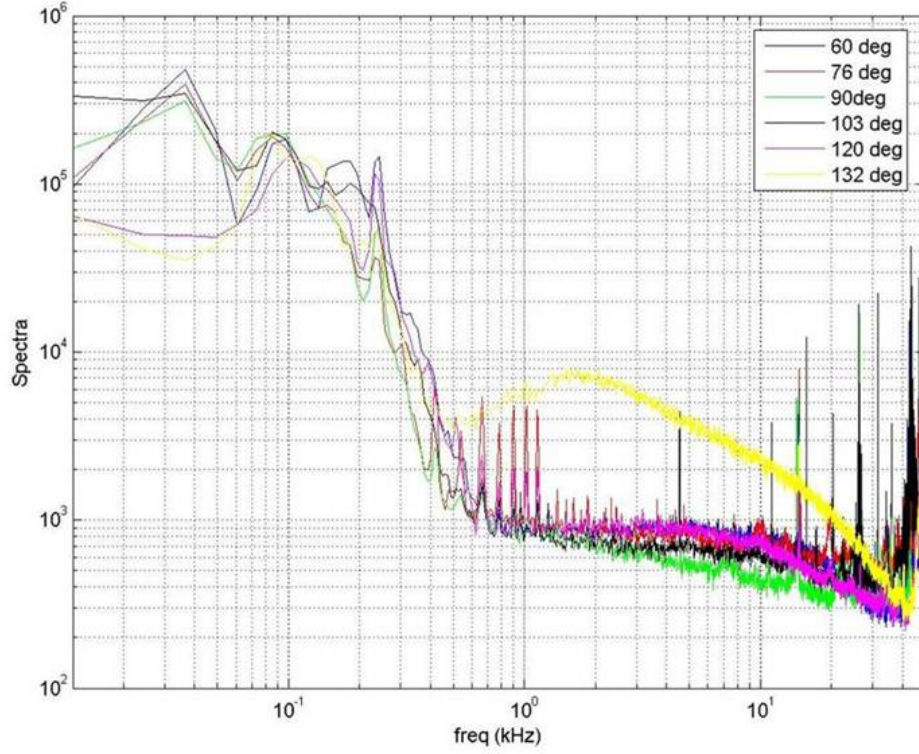


Figure 36: Deflection angle spectra for different elevation angles,  $M = 0.4$ .

Deflection angle power spectra plots for different elevation angles for  $M = 0.4$  are presented in Figure 36. Spectra for all angles have strong low frequency components,  $f < 0.7$  kHz. For back-looking angle of  $132^\circ$  the laser beam passes through a shear layer formed in the separation region behind the turret, so the deflection angle spectrum have an additional, shear-layer related peak around 2 kHz. Narrow peaks in spectra are electronic noise.

Phase plots for all elevation angles at  $M = 0.4$  are presented in Figure 37. All phase plots have a zero-phase correlation plateau for low frequencies below 0.8 kHz, suggesting the presence of stationary disturbances. The nature of these disturbances will be discussed later. All these stationary frequencies were removed using a low-pass filter. Above 0.8 kHz, the phase plots show a linear dependence with frequency. This indicates a convective nature of optically aberrating structures at high frequencies.

Knowing the phase slope, convective speeds were calculated. Results are presented in Figure 38. Flow accelerates over the front portion of the turret and decelerates on the back until it separates around  $115^\circ$ . After this point, shear layer structures appear with convective speeds of 0.8 of freestream speed. These speeds are consistent with shear layer convective speeds for the flat window turret.

*Wavefront sensor results:* Uncorrelated 2-D wavefronts across the turret aperture were taken using a Wavefront Sciences CLAS-2D 2-dimensional wavefront system. Pictures of the test section and the optical set-up are presented in Figure 39. A frequency-doubled YAG:Nd laser beam (pulse duration of 6 nsec) was expanded to a 5 inch collimated beam and directed from the optical bench to the test section with

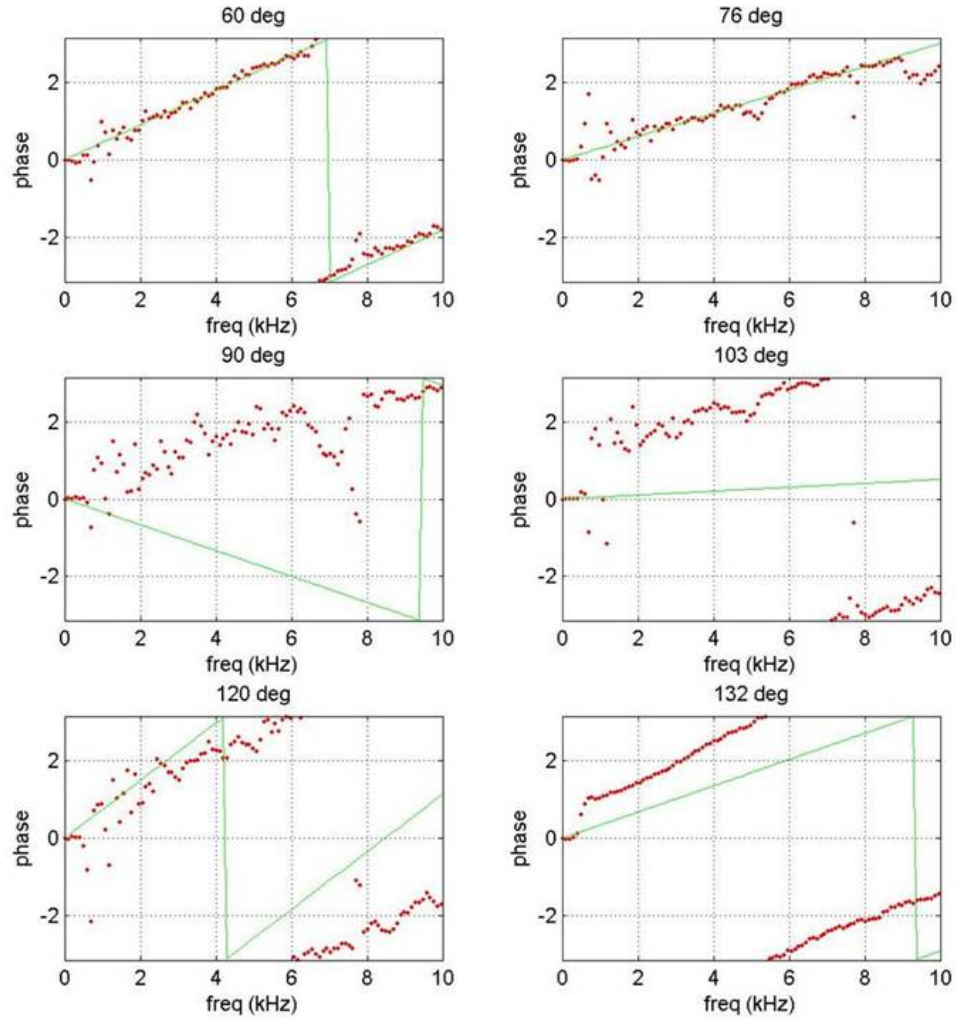


Figure 37: Phase plots  $\arg[S(f)]$  for different elevation angles,  $M = 0.4$ .

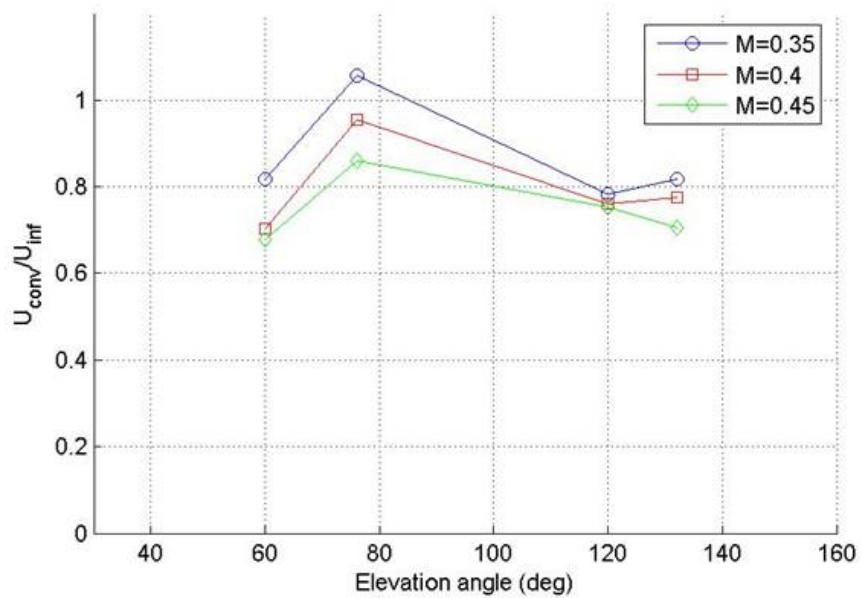


Figure 38: Convective speeds of optical structures from Malley probe.

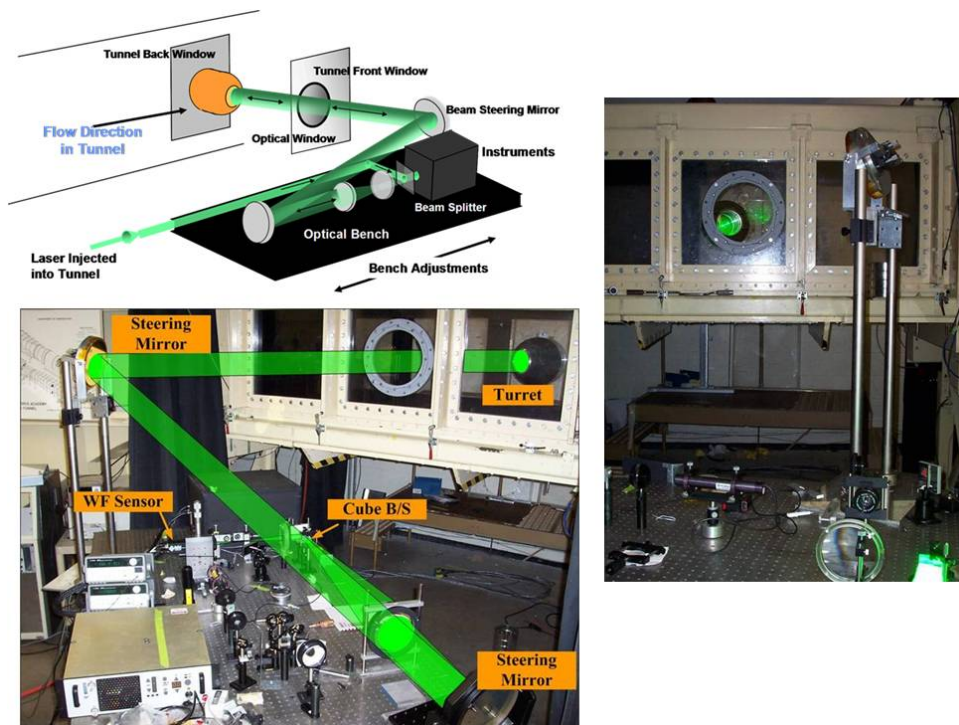


Figure 39: 2-D Wavefront Set-Up.



the turret using two large flat mirrors. The return beam was separated using a cube beam splitter. The beam's optical distortions were measured using the 2-D Shack-Hartmann wavefront sensor with a  $24 \times 36$  lenselet-array resolution. The wavefronts were sampled at 10 Hz. Two hundred wavefronts were recorded for each elevation angle and Mach number as shown in Table 2. Due to spherical aberrations imposed by expanding optics, only the central, 4.5-inch-diameter portion was used to calculate wavefront error. The wavefronts for each elevation angle and Mach number were post-processed as follows:

1. A reference “no-flow” wavefront was obtained at the beginning of each run to characterize the static aberrations imposed on the laser beam. All wavefronts were measured as deviation from this reference wavefronts.
2. Piston and tip/tilt components were removed from each wavefront. Removed tip/tilt was recorded and mean values calculated.
3. A steady wavefront was computed by averaging all wavefronts.
4. The steady wavefront was subtracted from each wavefront and spatial  $OPD_{rms}$  averaged over all wavefronts.

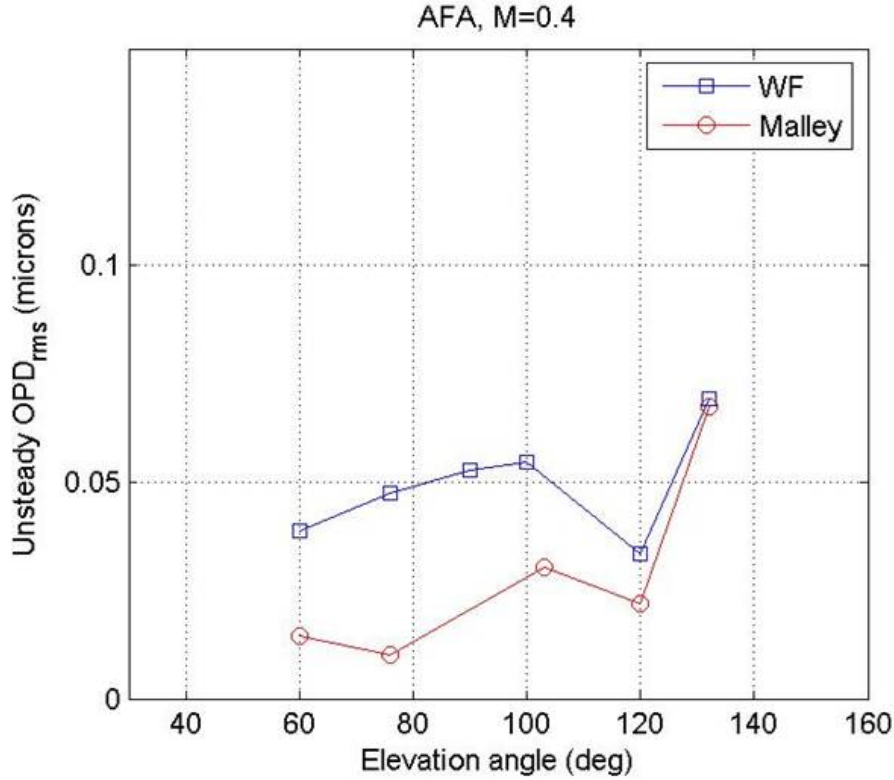


Figure 40:  $OPD_{rms}$  from WaveFront and Malley probe measurements.

$OPD_{rms}$  from the 2-D WaveFront sensor for different elevation angles at  $M = 0.4$  are presented in Figure 40. Also shown for comparison are results for  $OPD_{rms}$  from the Malley probe apertured to the central 4.5" beam. Malley probe and WF results give similar numbers for elevation angles above  $120^\circ$ . In this region, the dominant aberrations are the moving shear-layer structures. WF results are consistently higher than the Malley data for all angles below  $100^\circ$ . The reason of this discrepancy is that all zero-phase correlations, i.e. below 800 Hz, were filtered out from Malley probe data during a post-process analysis using a digital filter. Thus, any physical stationary aberrations were removed from resulting optical distortions.

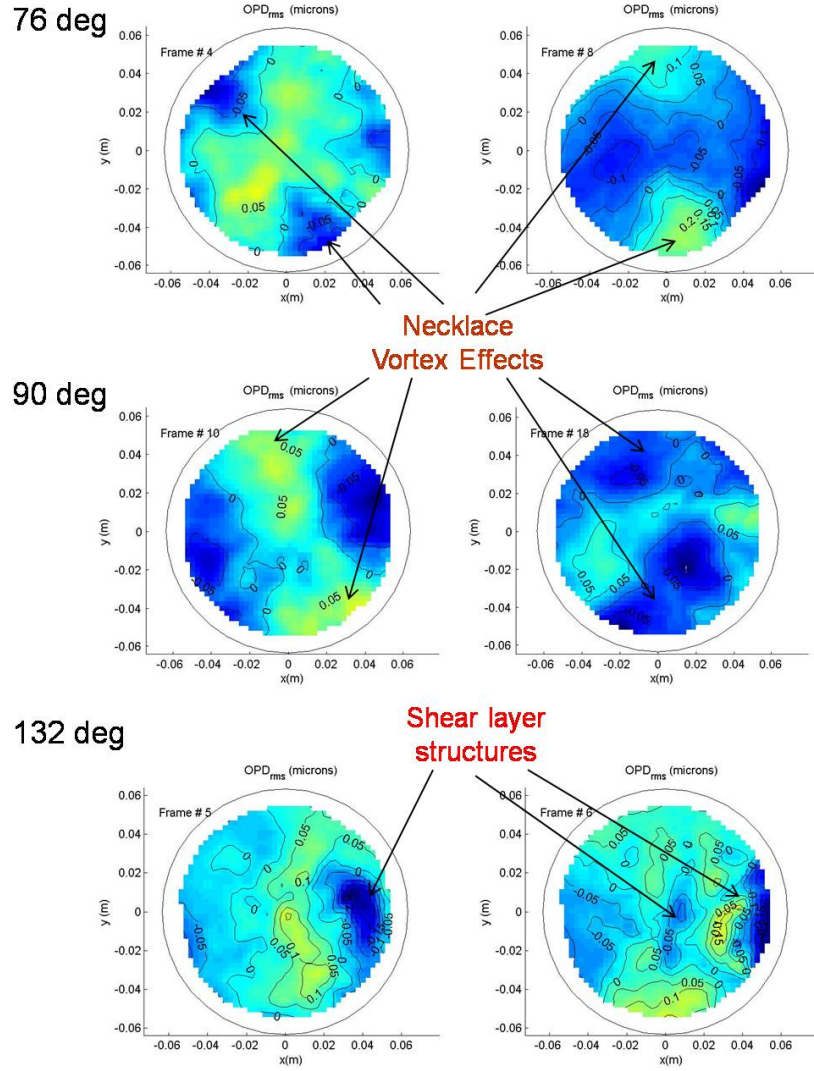


Figure 41: Selected wavefronts for 76, 90 and 132 degrees,  $M = 0.4$ . Flow goes from left to right.

To investigate the nature of stationary aberrations at forward looking angles, selected wavefronts for elevation angles of 76, 90 and 132° at  $M = 0.4$  are presented in Figure 41. Small to moderate deviations ( $\leq 0.12 \mu\text{m}$ ) from a planar wavefront can be observed on both sides of the aperture for 76° and 90° cases. These aberrations can be contributed to the influence of an unsteady necklace vortex formed on the bottom front portion of the turret. This slowly evolving vortex changes the potential flow everywhere around the turret through the Biot-Savart induction and creates stationary distortions on the laser beam. These aberrations are removed from Malley probe data, which under-predicts the optical aberrations using the Malley probe at forward looking angles, as in Figure 40.

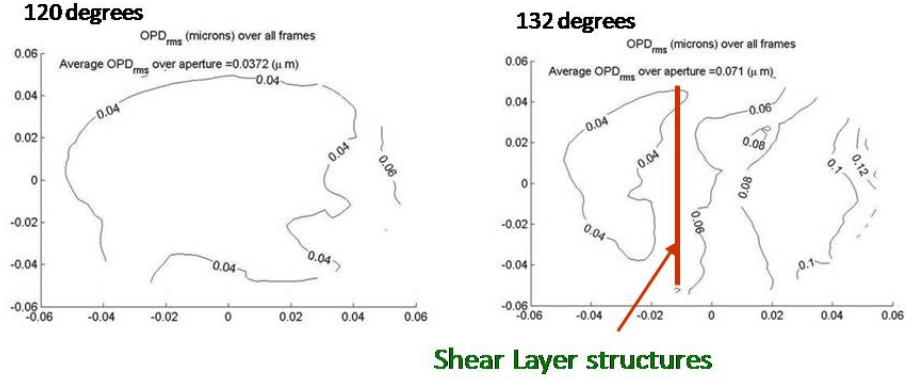


Figure 42: Temporal variations of wavefronts over the aperture,  $M = 0.4$ .

After the flow separates at 120°, spanwise shear-layer structures appear downstream. These are clearly visible for the 132 degrees case in Figure 41. Although the flow separates at 115° for  $M = 0.4$ , shear layer structures are developed some distance downstream of the separation point. Temporal variation of wavefronts over the aperture for 120° and 132° cases for  $M = 0.4$  are presented in Figure 42. For the 120 degree case, the  $OPD_{rms}$  is uniformly distributed over the aperture with levels of 0.04 microns. At 132°, the  $OPD_{rms}$  is around 0.04 microns for the front half of the aperture and increases downstream starting from the middle of aperture. This marks the onset of shear-layer structure formation. A linear growth of the shear layer leads to an observed linear increase in  $OPD_{rms}$  at the downstream half of the aperture.

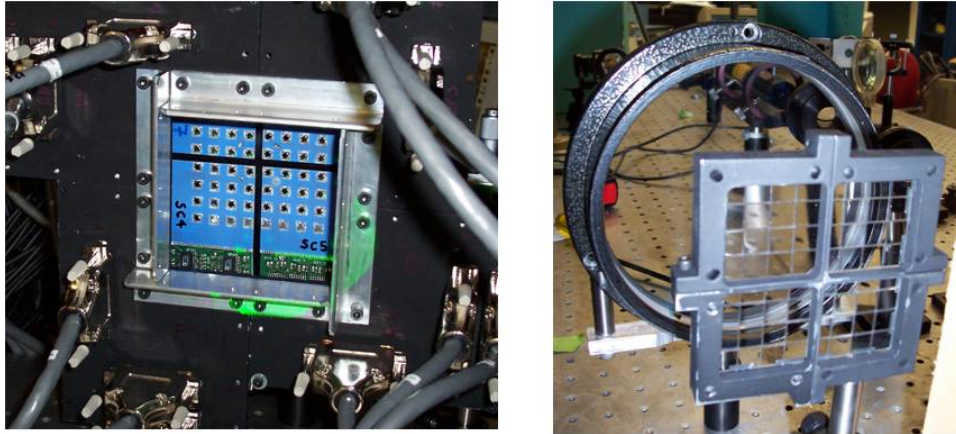


Figure 43: 8 × 8 Wavefront sensor.

*8 × 8 High-Bandwidth Wavefront Sensor Results:* A high-bandwidth wavefront sensor was also used to measure temporal-spatial evolution of wavefronts. The high-bandwidth wavefront sensor was jointly developed with Oceanit. It is a Hartmann-type wavefront sensor with a 80 mm x 80mm 8 × 8 lenslet array (Figure 43, left) and an 8 × 8 square array of analog position sensing devices to measure beam centroids,

(Figure 259, right). The analog nature of the data acquisition board allows wavefront sampling rates up to 78 kHz.

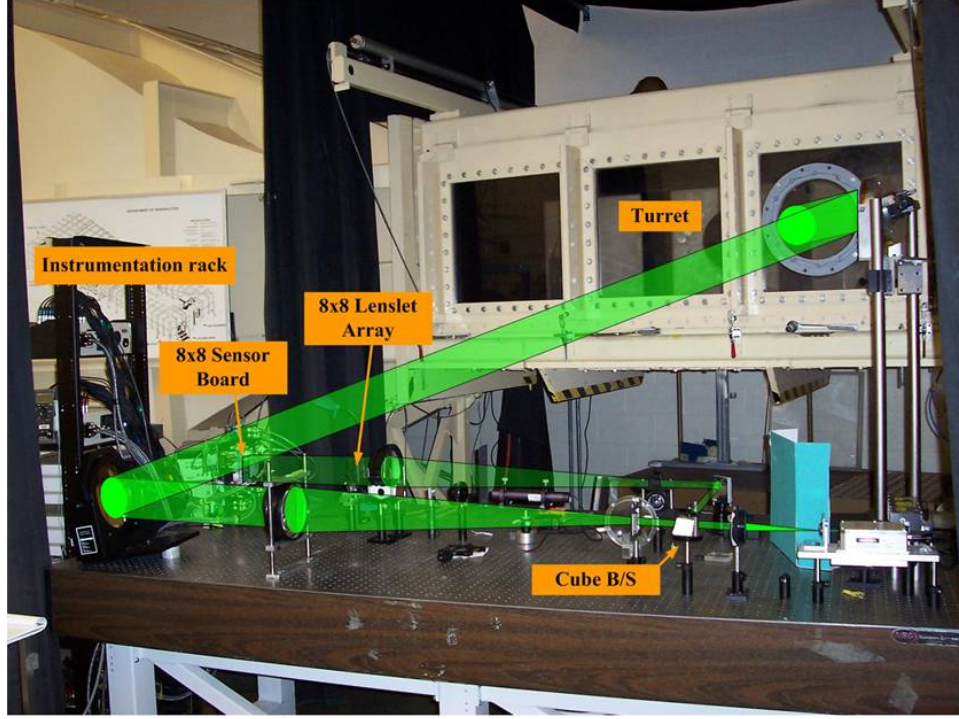


Figure 44:  $8 \times 8$  wavefront sensor optical set-up.

The high-bandwidth wavefront optical set-up is presented in Figure 44. A continuous wave YAG:Nd laser beam was expanded to 5", and transmitted through the flow to the turret. The reflected beam is sent to the  $8 \times 8$  wavefront sensor using a cube beam splitter. Only the middle portion of the returned beam with a diameter of 3" (not 4.5 ") was used to reconstruct wavefronts as follows:

1. 128 channels (2 channels per each sensor) are sampled at 78 kHz for 10 seconds.
2. Using calibration constants, signals are converted to deflection angles  $\theta(t)$ .
3. Deflection angles' time histories are filtered using either low- or high-pass filter to separate stationary and traveling structures.
4. Wavefronts are computed from deflection angles,  $WF(t) = \nabla\theta$ .
5. Piston and Tip/Tilt modes are removed from each wavefront.
6. Steady wavefront is computed over all wavefronts.
7. Steady component is removed from each wavefront.
8. Resulting wavefronts reflect unsteady components only.

Low and high-pass components of  $OPD_{rms}$  are computed by low- or high-filtering deflection angles' time series prior to wavefront reconstruction.

The temporal evolution of the  $OPD_{rms}$  over the aperture at  $M = 0.4$  are presented in Figure 45. Both high-pass (above 0.8 kHz) filtered and no-filtered cases for two angles of  $120^\circ$  and  $132^\circ$  are shown. For the 120 degree case, most of optical aberrations are located at low frequencies, below 0.8 kHz. These exhibit large amplitude, low frequency deviations. This is due to the slow unsteady variation of the necklace vortex around the turret base. High frequencies, above 0.8 kHz, are responsible only for a small portion of



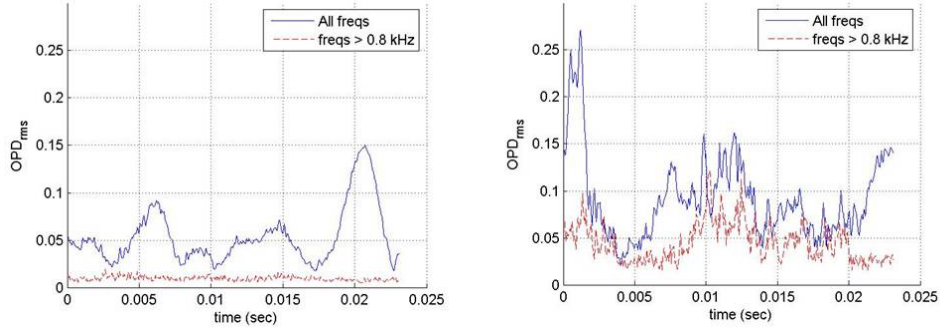


Figure 45: Temporal evolution of  $OPD_{rms}$  from  $8 \times 8$  sensor for 120 degree (left) and 132 degree (right) cases,  $M = 0.4$ .

optical aberrations for this angle. However, for the 132 degree case, the high, shear-layer-related frequencies cause most of optical aberrations. Low, necklace-vortex related frequencies occasionally influence optical distortions.

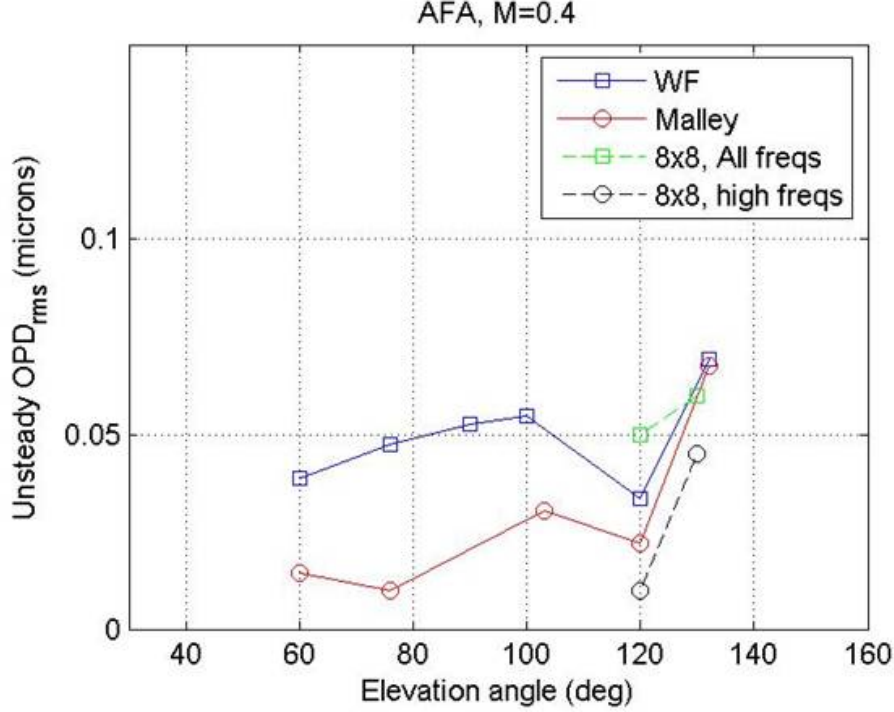


Figure 46:  $OPD_{rms}$  for different elevation angles for all measurement devices.

A summary of the time-averaged optical measurements using all three sensors are presented in Figure 46. Unfiltered  $8 \times 8$  sensor data (3" aperture) at elevation angles of  $120^\circ$  and  $132^\circ$  are similar to WF results (4.5" aperture), and give about 0.05 microns of optical aberrations at  $M = 0.4$ . High-pass filtered  $8 \times 8$  sensor results are similar to the Malley probe data (4.5" aperture), since neither include stationary effects of the necklace vortex. Overall, optical aberrations are high for backward looking angles, where structures in the separated shear layer play a dominant role.

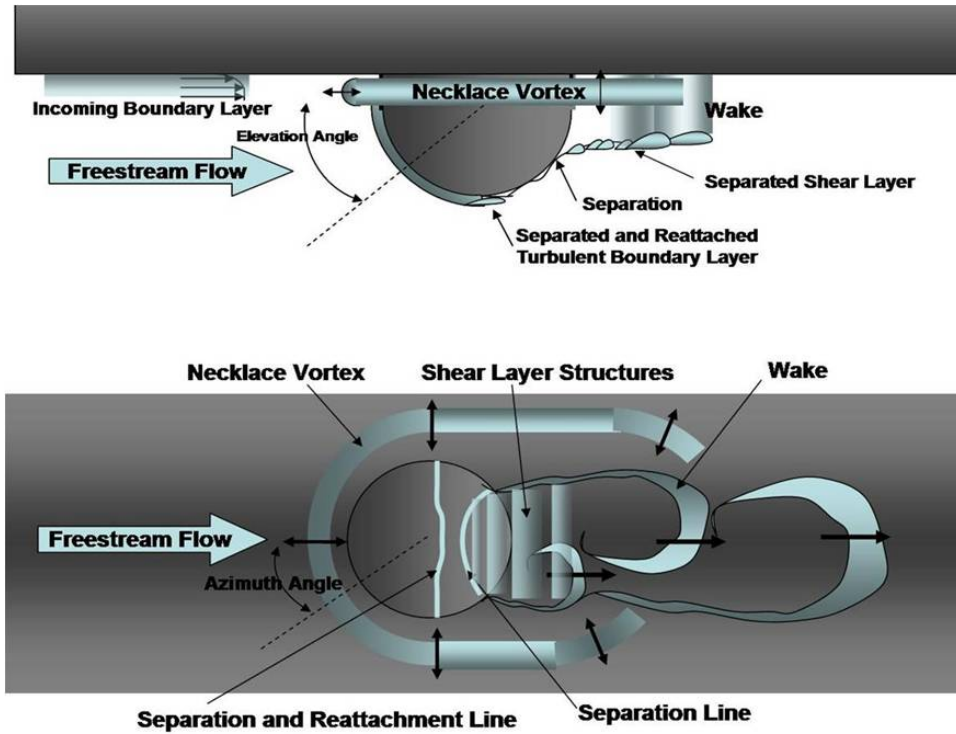


Figure 47: Flow topology around the conformal-window turret.

## Summary

Both hydrodynamic and optical data of the flow around a hemisphere-on-cylinder with a conformal window were collected and analyzed. Analysis reveals a complex structure of the flow around the turret, as shown in Figure 47. OPD's in forward lines-of-sight are influenced by the necklace vortex at the turret base. The necklace vortex wraps around the turret base and convects downstream. Flow stays attached on the front portion of the turret and separates behind it, forming a shear layer and unsteady wake downstream of the turret.

Depending on the elevation angle, the laser beam passes through physically different regions of the flow. For forward-looking angles, the main optical distortion mechanism is the slowly changing potential flow around the turret due to the necklace vortex. Optical structures are stationary at these angles. The OPD depends on the size of the turret and height of its base, relative to the vortex. For subsonic flow and turret diameters greater than about 12 inches, the influence of the vortex is relatively small. For backward-looking angles beyond separation, the influence of the vortex is also small. In contrast, the convecting shear layer structures are the primary contributor to larger OPD's in this region.

Using a suite of instruments allows one to better understand the underlying flow physics. In this test program, a Malley Probe, a 24 X 36 2-D Shack-Hartmann wavefront sensor, and an 8 x 8 wavefront sensor were used. The Malley probe allowed high bandwidth in-flow characterization of 1D OPD "slices". The Shack-Hartmann provided temporally-uncorrelated but spatially-resolved 2D OPD maps. And the 8 x 8 WFS produced high bandwidth, temporally resolved, 2D OPD measurements.

When compared with properly scaled results from the small turret experiment, some aspects of the flow around the large turret (the necklace vortex dynamics, the separation point) were found to be Reynolds number dependent, while other aspects remained the same (shear layer structures in the separation region). This is important in evaluating the accuracy and reliability of scaling with density, Mach number and turret size.

## 2.4 1-Foot Turret with Flat Window

### Experimental Set-Up

The next set of experimental data corresponds to a one-foot turret configuration with a flat window (see Figures 48 and 49). The tests were performed in the United States Air Force Academy's Subsonic Wind Tunnel. The wind tunnel has test-section dimension of 3 ft  $\times$  3 ft (see Figure 48) and ambient conditions corresponding to the facility's altitude of 7,160 ft. It is important to note that the wind tunnel breather is located in the settling chamber; as such, the facility ambient conditions are effectively the test-section stagnation properties. The test section flow parameters are given in Table 3, while the model parameters are given in Table 4. Plots of the data sets discussed below, as well as interpretation of the data, are presented in considerable detail in Reference [4].

Table 3: Test-section flow parameters

Parameter	Value
Temperature	Not controlled, typically 30° C to 40° C
Free-stream turbulence	0.2 %
Total pressure	78 kPa (nominal)
Total density	0.99 kg/m <sup>3</sup>
Mach number range	0.3 to 0.5 (see individual tests)

Table 4: Model parameters

Parameter	Value
Model	Hemisphere-on-Cylinder Turret, D=12, H=4 Window: flat, 5.4 dia, flush with hemisphere at window edges
Re based on D	$\approx 2.2$ to 3.6 million
Test-section floor boundary-layer thickness at model	$\approx 0.08$ D
Model area blockage	8.5%

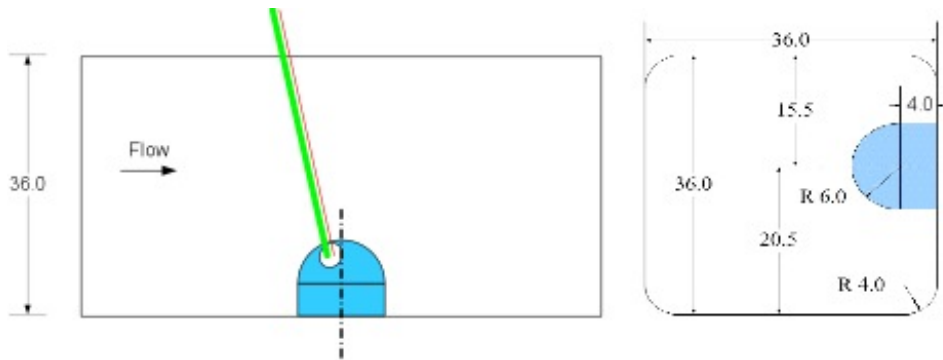


Figure 48: Test section schematic (dimension in inches).

### Hot-wire Measurements

Time-averaged mean and rms fluctuating data was collected at Locations 1, 2 and 3 (see Figure 49) for an incoming Mach number of  $M_\infty = 0.3$  with the turret at an azimuthal angle of  $100^\circ$ , as well as at  $M_\infty = 0.35$



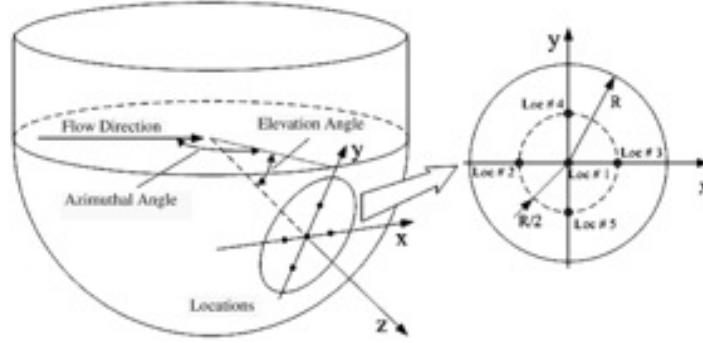


Figure 49: Turret orientation and measurement locations

with an azimuthal angle of  $110^\circ$ .

### Malley Probe Measurements

Instantaneous 1D Malley probe data was collected for various test configurations and conditions. Two azimuthal angles,  $100^\circ$  and  $135^\circ$ , were considered with three incoming Mach numbers ( $M_\infty = 0.35, 0.4, 0.45$ ). For the azimuthal angle of  $100^\circ$ , data was acquired for the baseline turret case as well as for the cases where passive control devices (pins or small vortex generators) were employed upstream of the flat turret. For the azimuthal angle of  $135^\circ$ , data corresponding to the baseline and small vortex generator cases only were provided. The data includes 50 instantaneous frames for two independent measurement sets at each configuration examined.

### Wavefront Measurements

Wavefront measurements obtained with a 2D Shack-Hartmann wavefront sensor were also acquired at azimuthal angles of  $100^\circ$ ,  $110^\circ$ ,  $114^\circ$  and  $135^\circ$ , with zero angle facing upstream. Instantaneous unsteady wavefronts were obtained for a Baseline case, as well as for passive control devices (pins and small vortex generators, or SVG) placed upstream of the flat window. Incoming Mach numbers of 0.35, 0.4 and 0.45 were considered and the aperture size is 4.5 inches. The 2-D wavefront data reduction procedure was as follows:

1. A reference "no-flow" wavefront was obtained at the beginning of each run to absorb all non-flow related aberrations imposed on the laser beam and all wavefronts were measured as deviation from this reference wavefronts.
2. Piston and tip/tilt components were removed from each wavefront. Removed tip/tilt was recorded and mean values of removed tip/tilt were calculated.
3. A steady wavefront was computed by averaging among all wavefronts.
4. The steady wavefront was subtracted from each wavefront. Resulting wavefronts saved as unsteady instantaneous wavefronts.

## 2.5 4-Inch Cylindrical Turret with Flat Window

The baseline flow and effects of different passive control devices on aero-optical environment over the cylindrical turret with the flat insert were investigated in order to better understand underlying physics of optical aberrations. A test section with the rotating 2-dimensional turret with the flat window was built at Hessert Center, University of Notre Dame (see Figure 50 for general view and detailed test section dimensions). The rotating cylinder of 4 inches in diameter has a flat window insert 2 inches long and 3 inches wide with an optically accessible portion of 1.5 inches by 2.5 inches. The cylinder can be rotated to position the flat window relative to the freestream direction, so the elevation angle of the outgoing laser beam was between

90° (looking upward) and 150°. The test section is instrumented with 8 steady pressure ports, marked by red circles in Figure 50 to monitor the streamwise evolution of the flow around the cylinder.

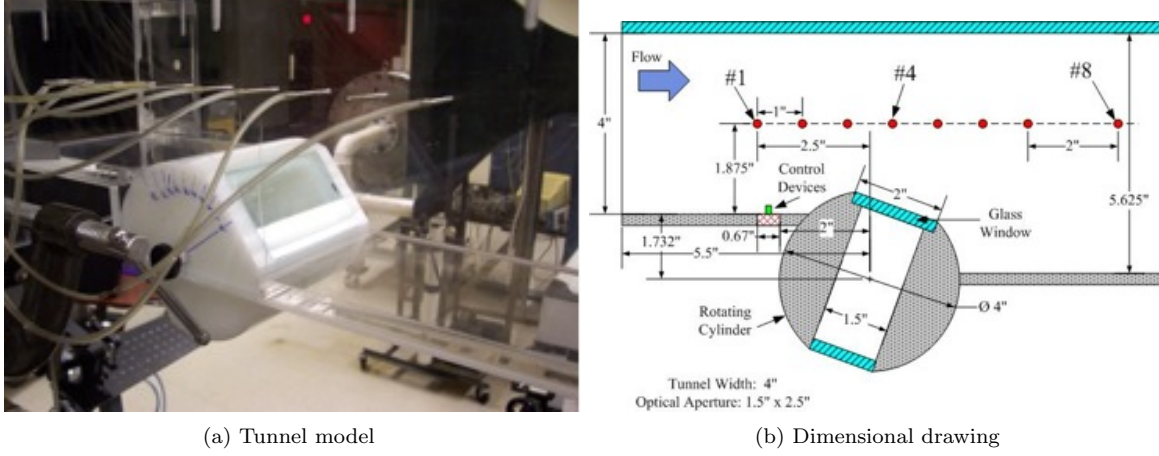


Figure 50: 2-dimensional turret

Due to blockage effects from the cylinder, the flow was quantified by two Mach numbers, calculated from steady pressure data using isentropic relation between the pressure drop and  $M$ : incoming Mach number,  $M_{in}$ , was calculated at Port # 1, Figure 50 and turret Mach number,  $M_{turret}$ , was calculated at Port #4, Figure 50.

Database provides the following hydrodynamic and optical data for baseline and several devices placed upstream of the cylinder (see the following section):

1. Relative pressure values at pressure ports for different incoming  $M$ .
2. Velocity profiles at different streamwise locations for one  $M$  (baseline only).
3. 2-D wavefronts for different  $M$  and elevation angles, see Figure 51 for an optical set-up.

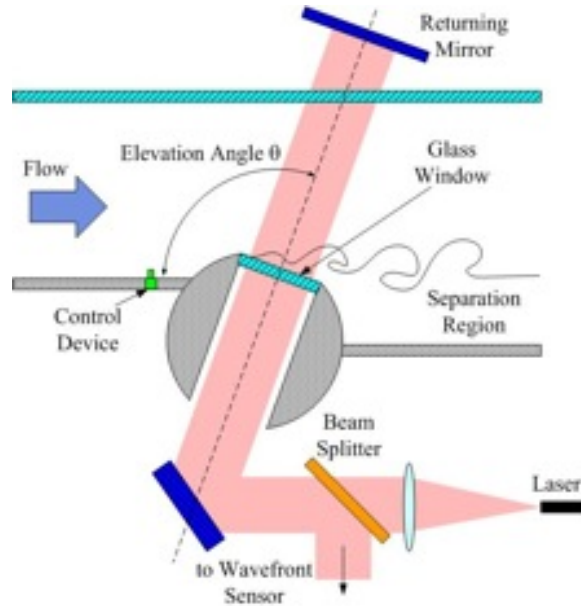


Figure 51: Optical set-up to measure 2-D wavefronts

### Passive Control Devices

Different inserts with passive devices were placed upstream of the turret, see Figure 50. The following devices were tested: pins with different diameters, 1 mm, 3 mm and 5 mm, small vortex generators (SVG) and big vortex generators (BVG, BVG2 and BVG3), see Figures 52 and 53. Geometrical information is provided in Table 5. All vortex generators have triangular shapes with a  $45^\circ$  leading beveled edge. Heights of pins and small VGs were chosen to be 5 mm, which is on the order the incoming boundary layer thickness (7 mm). Big VGs were chosen to introduce strong counter-rotating streamwise vortices in an attempt to significantly modify the mean flow over and behind the turret.

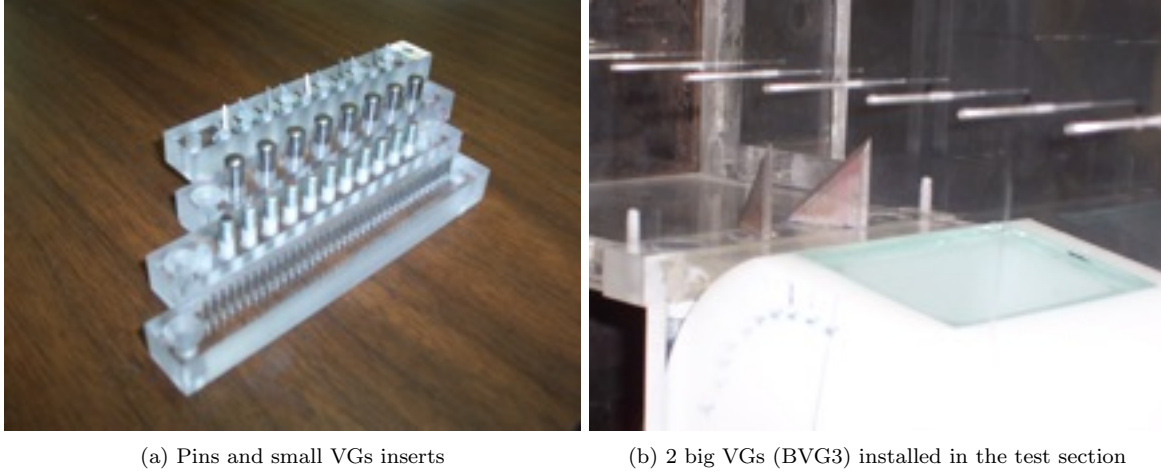


Figure 52: Flow control devices

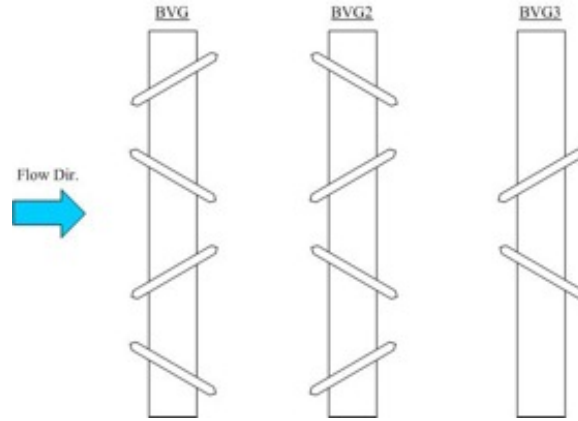


Figure 53: BVG arrangements

Static pressure data were taken at various azimuthal angles and incoming Mach numbers along the tunnels side wall at 8 locations, see Table 6 and Figure 50(b) for locations. All coordinates are given in the turrets frame of reference, with a zero coinciding with the cylinders center, x-axis is horizontal axis in the downstream direction and the y-axis is vertical axis normal to the bottom tunnel wall. Pressure data was collected for the turret configurations listed in Table 5. Time averaged velocity profiles were also collected at a wide variety of locations for the baseline (no flow control) configuration.

Wavefront data was also collected at various incoming Mach numbers and azimuthal angles for the various

Table 5: Description of Passive Control Devices

Control Device	Configuration	Height	Spanwise Spacing
Pins, 1 mm	Series of 1mm vertical cylindrical pins	5 mm	2 mm
Pins, 3 mm	Series of 3mm vertical cylindrical pins	5 mm	6 mm
Pins, 5 mm	Series of 5mm vertical cylindrical pins	5 mm	10 mm
Small VG (SVG)	Series of triangular vertical VG, placed at +/- 30° to incoming flow	5 mm	10 mm
BVG, see Figure 53	4 triangular vertical VG, placed at +/- 30° to incoming flow	25 mm	50 mm
BVG2, see Figure 53	4 triangular vertical VG, placed at +/- 30° to incoming flow	25 mm	50 mm
BVG3, see Figure 53	2 triangular vertical VG, placed at +/- 30° to incoming flow	25 mm	50 mm

turret configurations of Table 5. Data in the form of  $OPD_{rms}$  are available, where

$$OPD_{rms} = \sqrt{\left\langle \frac{\int_{A_p} W^2(x, y, t) dx dy}{\int_{A_p} dx dy} \right\rangle} \quad (2)$$

Here  $A_p$  is the beam aperture, the brackets denote ensemble (time) averaging, and  $W(x, y, t)$  is the instantaneous wavefront calculated as follows:

1. A reference "no-flow" wavefront was obtained at the beginning of each run to absorb all non-flow related aberrations imposed on the laser beam and all wavefronts were measured as deviation from this reference wavefronts.
2. Piston and tip/tilt components were removed from each wavefront. Removed tip/tilt was recorded and mean values of removed tip/tilt were calculated.
3. A steady wavefront,  $W_{steady}(x, y)$ , was computed by averaging among all wavefronts.
4. The steady wavefront was subtracted from each wavefront. Resulting wavefronts saved as unsteady instantaneous wavefronts,  $W(x, y, t)$ .

Table 6: Pressure port locations

Port #	1	2	3	4	5	6	7	8
x (inches)	-2.5	-1.5	-0.5	0.5	1.5	2.5	3.5	5.5
y (inches)	3.6	3.6	3.6	3.6	3.6	3.6	3.6	3.6

## 3 AVUS Code Analysis and Improvement for Aero-Optic Applications

### 3.1 Introduction

The passage of a planar optical wave-front through a flow field with varying density and turbulent intensity causes aberration of the wave front. This aberration has detrimental effects on the performance of the optical system, which uses the laser beam. The study of this aberration of the optical beam as it passes through the flow field that is disturbed by the moving object is called aero-optics. One of the pre-requisites for the study of aero-optics is an accurate prediction of the flow field around a moving object. The aberration of a wave-front is caused by a light transmission through time varying turbulent, index-of-refraction varying fluid structures next to the exit aperture of the light source. Optical aberrations are typically measured using the beams optical path length as it travels through these fluid structures. The changes in the optical path lengths are caused by the variation in the index-of-refraction due to varying density, turbulent shears and boundary layers. This necessitates benchmarking of the computational fluid dynamics (CFD) solver with these classes of problems. The Air Vehicle Unstructured Solver (AVUS) has been validated for the simulation of aerodynamics applications [5, 6, 7] and is routinely used by DoD researchers for a wide variety of applications. However, AVUS has not been used for the prediction of flow fields for the purpose of aero-optics analysis. A first step towards the use of the AVUS code for aero-optics application is the benchmarking of the code with shear flow simulations. Thus, the objectives of this effort is to benchmark AVUS for shear flow problems and make appropriate modifications to the AVUS code for better prediction of this class of problems.

### 3.2 Gradient Estimation

The estimation of gradients is an important step in the linear reconstruction of flow variables for higher order spatial accuracy. The gradients used in the linear reconstruction can influence the numerical dissipation and can dissipate vortices present in the flow field. Two of the most commonly used methods are the weighted averaging together with Gauss theorem [8] and least square approach [9, 10, 11].

#### Un-weighted Least Square Gradients

In this approach, the flow variables at the center of the cells surrounding the cell under consideration is expressed in terms of the cell averaged values and the gradient within the reference cell using Taylors series expansion. For example the properties in the neighboring cells of 0 (refer Figure 54) can be expressed as:

$$\begin{aligned} f_1 &= f_0 + f_x \Delta x_1 + f_y \Delta y_1 + O(\Delta x_1^2, \Delta y_1^2) \\ f_2 &= f_0 + f_x \Delta x_2 + f_y \Delta y_2 + O(\Delta x_2^2, \Delta y_2^2) \\ f_3 &= f_0 + f_x \Delta x_3 + f_y \Delta y_3 + O(\Delta x_3^2, \Delta y_3^2) \\ f_4 &= f_0 + f_x \Delta x_4 + f_y \Delta y_4 + O(\Delta x_4^2, \Delta y_4^2) \end{aligned} \tag{1}$$

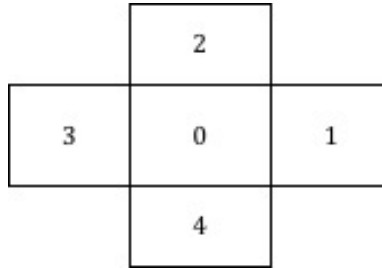


Figure 54: Sample grid for gradient estimation using least square approach

This will result in a linear system of equations.:

$$\begin{bmatrix} \Delta x_1 & \Delta y_1 \\ \Delta x_2 & \Delta y_2 \\ \Delta x_3 & \Delta y_3 \\ \Delta x_4 & \Delta y_4 \end{bmatrix} \begin{bmatrix} f_x \\ f_y \end{bmatrix} = \begin{bmatrix} f_0 - f_1 \\ f_0 - f_2 \\ f_0 - f_3 \\ f_0 - f_4 \end{bmatrix} \quad (2)$$

An example of the linear system is given in the above equation and the corresponding two-dimensional grid is shown in Figure 54. This is usually an over determined system and is solved using either normal equations or the Gram-Schmidt method. For a viscous grid the condition number of the matrix resulting from the normal equations is very high. Therefore, the Gram-Schmidt method is preferred and is used for solving the least square problem. In terms of the AVUS variables, the gradient is estimated using the relation:

$$\begin{bmatrix} f_x \\ f_y \end{bmatrix} = [(RI \ QT)] \begin{bmatrix} f_0 - f_1 \\ f_0 - f_2 \\ f_0 - f_3 \\ f_0 - f_4 \end{bmatrix} \quad (3)$$

### Weighted Least Square Gradients

One of the disadvantages with the least square approach is that equal weights are given to all neighboring cells. This has a detrimental effect when there are high aspect ratio cells in the boundary layer. This can be overcome by dividing each of the expressions in Equation 2 by the distance between the centroids. With this modification, Equation 2 can be written as:

$$\begin{bmatrix} \frac{\Delta x_1}{ds_1} & \frac{\Delta y_1}{ds_1} \\ \frac{\Delta x_2}{ds_2} & \frac{\Delta y_2}{ds_2} \\ \frac{\Delta x_3}{ds_3} & \frac{\Delta y_3}{ds_3} \\ \frac{\Delta x_4}{ds_4} & \frac{\Delta y_4}{ds_4} \end{bmatrix} \begin{bmatrix} f_x \\ f_y \end{bmatrix} = \begin{bmatrix} \frac{f_0 - f_1}{ds_1} \\ \frac{f_0 - f_2}{ds_2} \\ \frac{f_0 - f_3}{ds_3} \\ \frac{f_0 - f_4}{ds_4} \end{bmatrix} \quad (4)$$

In terms of the AVUS variable, this can result in:

$$\begin{bmatrix} f_x \\ f_y \end{bmatrix} = [(RI \ QT)'] \begin{bmatrix} f_0 - f_1 \\ f_0 - f_2 \\ f_0 - f_3 \\ f_0 - f_4 \end{bmatrix} \quad (5)$$

where  $(RI \ QT)'$  is calculated using the right-hand side of Equation 4. Also, the distance between the cell centroids in Equation 5 can be absorbed into  $(RI \ QT)'$  and the resulting equation can be written in the same form as Equation 3. The resulting equation can be written as:

$$\begin{bmatrix} f_x \\ f_y \end{bmatrix} = [(RI \ QT)'] \begin{bmatrix} f_0 - f_1 \\ f_0 - f_2 \\ f_0 - f_3 \\ f_0 - f_4 \end{bmatrix} \quad (6)$$

### Validation of weighted least square method

The validation of the implementation of the weighted least square approach for the estimation of gradients is achieved using a transonic flow past a NACA0012 airfoil. The following freestream conditions are used



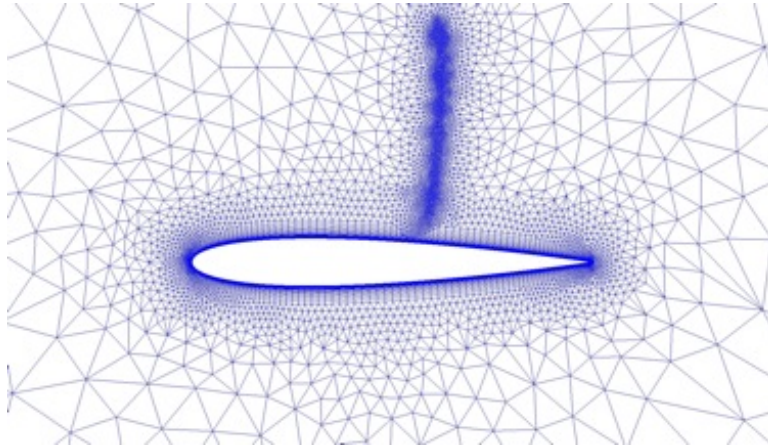
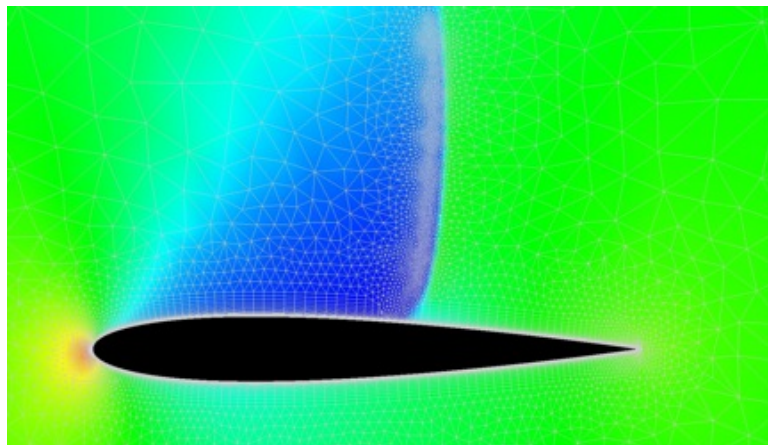
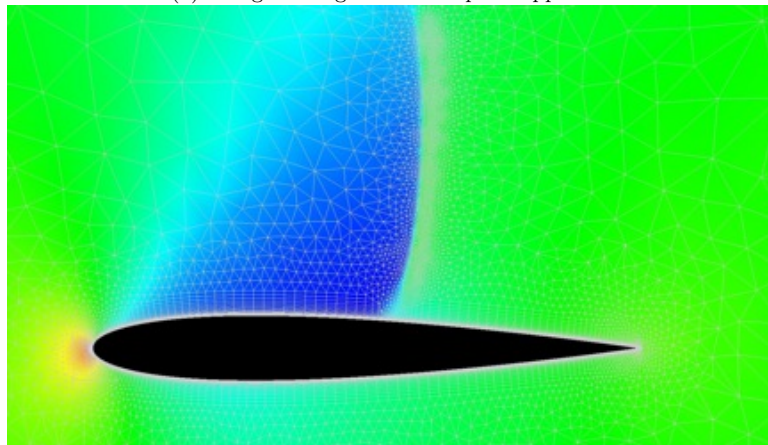


Figure 55: Grid used for the transonic flow past NACA0012 airfoil



(a) Using un-weighted least square approach



(b) Using weighted least square approach

Figure 56: Comparison of pressure distribution around NACA0012 airfoil for different least square approaches

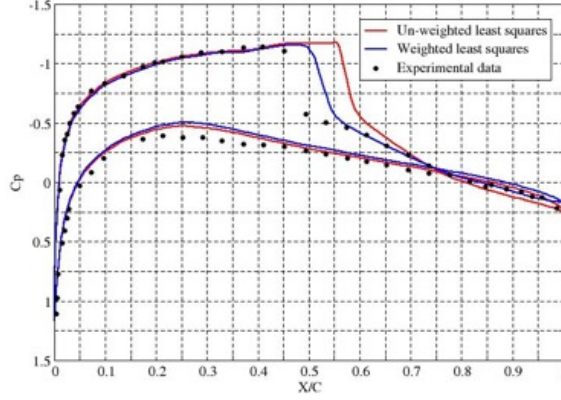


Figure 57: Comparison of  $C_p$  distribution around NACA0012 airfoil for weighted and un-weighted least square approaches

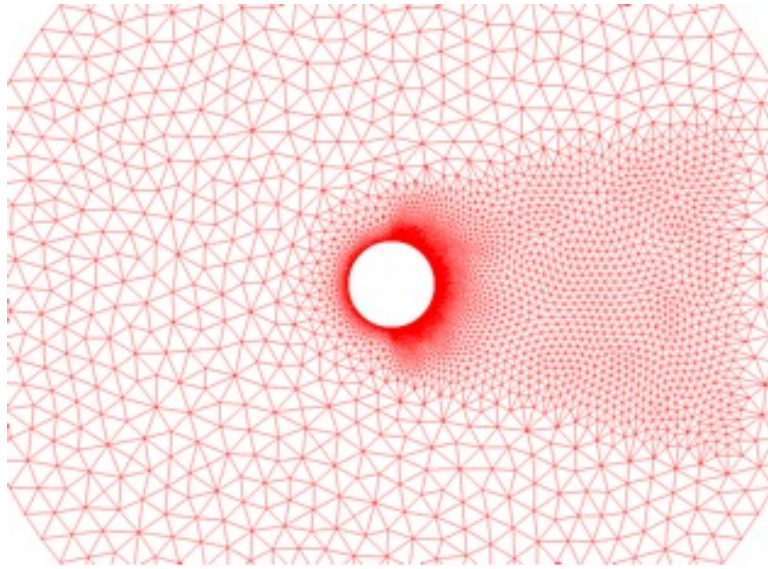
for this simulation: a Mach number of 0.799, angle of attack of 2.26, and Reynolds number of  $9.0 \times 10^6$ . A hybrid grid, shown in Figure 55, has been used for this simulation. A clustering of points in the vicinity of the shock has been used for this simulation as shown in Figure 55. The computed pressure distribution around the airfoil using weighted and un-weighted least square approaches are shown in Figure 56. It can be seen from these figures that the un-weighted least square approach predicts the shock location downstream of the grid clustering, while the weighted least square approach predicts the shock location upstream of the clustering. The predicted  $C_p$  distribution for both these approaches is compared with the experimental data in Figure 57. It can be seen from the figure that the weighted least square approach predicts the shock location accurately when compared to that done by the un-weighted least square approach.

### 3.3 Summary of Laminar Cylinder Simulations

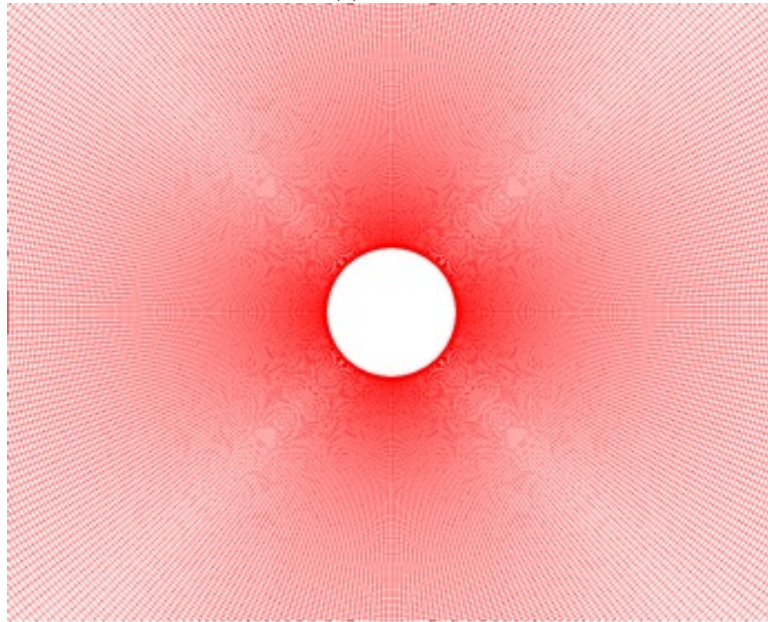
A 2-dimensional and a 3-dimensional grid have been used for the simulation of vortex shedding from a circular cylinder. An unstructured grid with grid packing in the wake region as shown in Figure 58(a) is for the 2-D simulation. A structured grid with 361 points along the circumferential direction, three planes in the z-direction with a spacing of 0.1 units has been used as the 3-D grid (shown in Figure 58(b)). The details of the 3-D grid include: outer diameter of the domain as 15, distance of first point of the wall as  $1.0 \times 10^{-3}$ , and geometrical growth of grid spacing normal to the wall with a growth ratio of 1.15 in the boundary layer and 1.01 after that.

Computational simulations has been carried out for Reynolds numbers of 200 and 300 using the 2004 and 2006 versions of AVUS with and without weighted least square approaches for the gradient estimation. The summary of these simulations is given in this section of the report. For all these simulations the following input parameters have been used:  $\theta$  (parameter to select explicit or implicit schemes) as 0.75, 32 iterations for the Gauss-Seidel iterations, temporal damping coefficients of 0.1 for inviscid and 0.05 for viscous Jacobians, 5 Newton iterations, and a time step of 3.673625 seconds. A typical pressure distribution around the cylinder during the vortex shedding is shown in Figure 59 and the time history of the forces acting on the cylinder is shown in Figure 60. From these figures, it can be seen that the period vortex shedding is predicted by the simulations.

A typical power spectral density distribution from the spectral analysis of the lift and drag forces is shown in Figure 61. This power spectral density distribution is used for the estimation of the Strouhal number for the vortex shedding. The Strouhal number is the non-dimensional frequency and is defined as  $St = fL/U$ , where  $St$  is the Strouhal number,  $f$  is the frequency,  $L$  is the reference length, and  $U$  is the reference velocity. A summary of the mean values of the lift and drag coefficients, and the Strouhal number from the spectral analysis is tabulated in Table 7. It can be seen from this table that the predicted Strouhal numbers for the weighted and un-weighted least square approaches are approximately the same for all the cases and matches well with the experimental data (0.178-0.201 for  $Re = 200$  and 0.192-0.208 for  $Re = 300$ ). For the 2-D



(a) 2D Grid



(b) 3D Grid

Figure 58: Grids used for the simulation of laminar vortex shedding from a cylinder



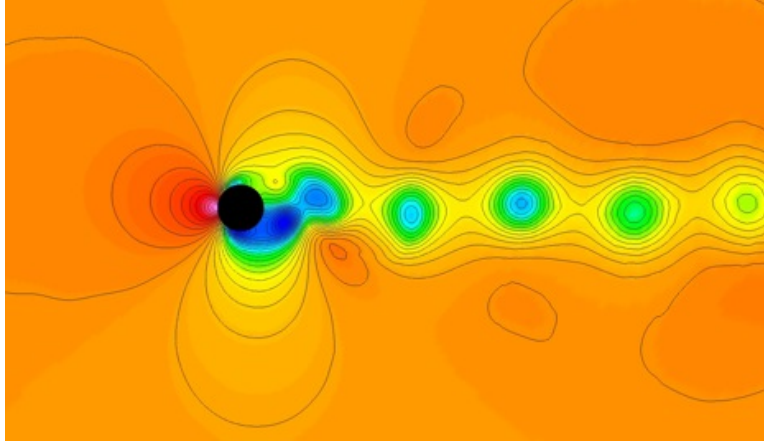
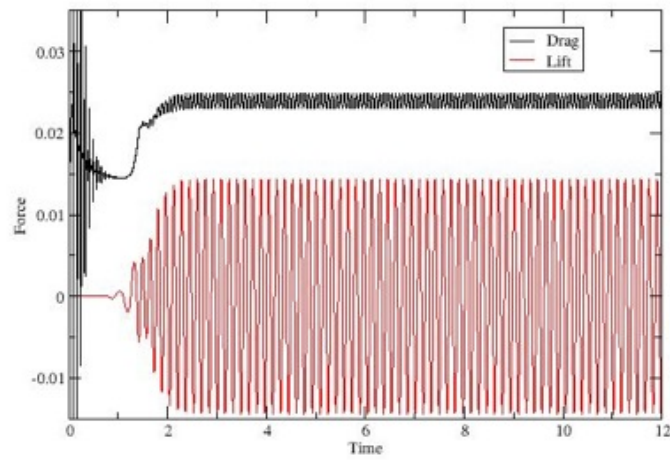
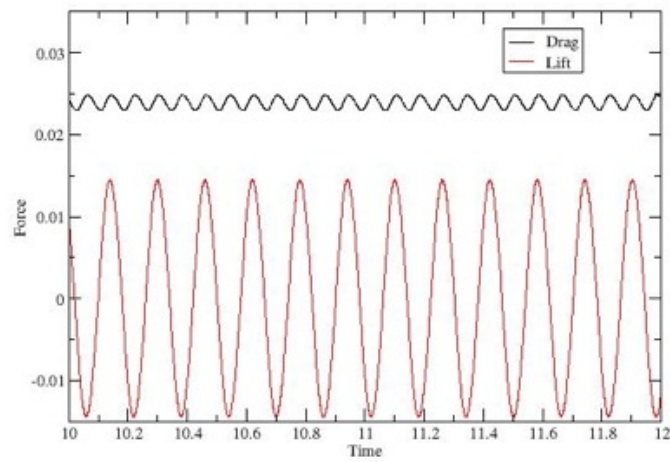


Figure 59: Pressure distribution around the cylinder during vortex shedding



(a) Overall View



(b) Detailed View

Figure 60: Time history of forces acting on the cylinder

simulations, the predicted drag coefficients are slightly higher for the weighted least square approach when compared with the un-weighted approach. However, the drag coefficients are approximately the same for the 3-D simulations. It was noted that the 2004 version of the AVUS code did not predict the vortex shedding for the 3-D case. The lift coefficients are very small when compared to the drag coefficient, and therefore are not used for the estimation of the accuracy of numerical schemes.

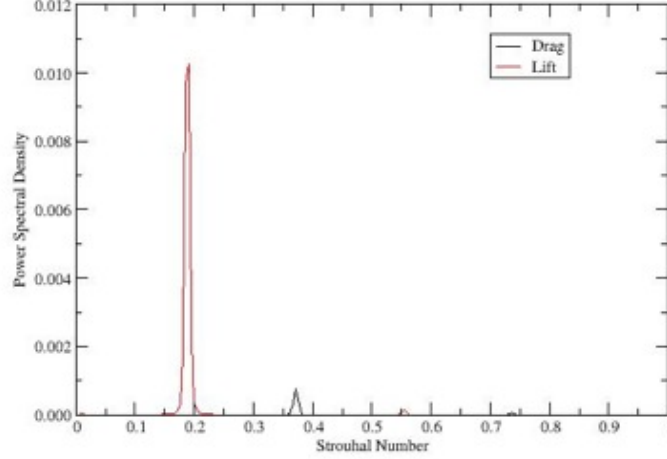


Figure 61: Power Spectral Density (PSD) of the vortex shedding

Table 7: Summary of results for the laminar vortex shedding simulations.

Case	Re	$C_l$			$C_d$			Strouhal number		
		Old code	Wtd	Un-Wtd	Old Code	Wtd	Un-Wtd	Old code	Wtd	Un-Wtd
2D	200	5.50e-03	-9.00e-03	1.68e-03	1.2795	1.4871	1.2778	0.2002	0.2010	0.2002
	300	0.0153	0.0173	0.0227	1.2868	1.4511	1.2824	0.2010	0.2100	0.2100
3D	200	-	-8.07e-06	8.33e-04	-	1.2860	1.2855	-	0.1855	0.1807
	300	-	4.45e-03	-5.70e-03	-	1.3088	1.3099	-	0.1904	0.1904

### 3.4 Summary of Turbulent Cylinder Simulations

Unsteady three-dimensional calculations were performed for the vortex shedding from a circular cylinder for  $M = 0.2$  and  $Re_d = 8 \times 10^6$ . The experimental Strouhal number for this case is approximately 0.307. The Strouhal number is defined as:

$$St = \frac{fL}{U} \quad (7)$$

where  $f$  is the frequency of vortex shedding,  $L$  is the characteristic length, and  $U$  is the characteristic velocity. In this simulation, the characteristic length (diameter of the cylinder) is taken as 1m, and the characteristic velocity is taken as 66.8432 m/sec (Speed of sound (334.216 m/sec) times the Mach number (0.2)). This results in the vortex shedding frequency of 20.52 Hz and a period of 0.306 seconds. The details of the grids used for the simulations and the results obtained are listed below.

#### Computational Domain and Grids

The computational domain for these simulations is taken as a cylinder with unit diameter and a field of 15 units around it. A uniform grid is used in the circumferential direction and geometric progression is used

Table 8: Summary of grids used and the computed Strouhal numbers for the turbulent vortex shedding simulations.

Grid	Points in circumferential dir	Distance to first point off the wall	Time step	$y^+$	Strouhal number	Weighted LSF Strouhal number
1	181	1.70e-06	0.002	0.033	0.025	
2	181	3.40e-06	0.002	0.0685	0.025	
3	181	6.80e-06	0.002	0.1395	0.025	
4	181	1.36e-05	0.002	0.33668	0.025	
4	181	1.36e-05	9.10e-05	0.3752	0.07	
5						
6	361	2.50e-05	9.10e-05	0.9523	0.08	0.08
7	401	1.70e-06	9.10e-05	0.092	0.08	
8	401	3.40e-06	9.10e-05	0.17	0.08	0.08

for the growth of grid spacing in the radial direction. A growth factor of 1.1 is used until a radial distance of 0.6 and a ratio of 1.01 is used afterwards. The smaller growth ratio behind the boundary layer preserves enough grid resolution to capture the wake behind the cylinder. The spacing of the first point off the wall is calculated based on the applet given in <http://geolab.larc.nasa.gov/APPS/YPlus/>. For a Reynolds number of  $8.0 \times 10^6$  and a  $y^+ = 0.5$ , the first point off the wall is estimated to be  $1.70 \times 10^{-6}$ . This grid was progressively coarsened to check the effect of grid spacing. The details of various grids used for these simulations are listed below.

## Results

It was noticed from the simulations that the  $y^+$  after 50,000 iterations was  $0.033 - 0.37$  for the first point of the wall varying from  $1.70 \times 10^{-6}$  to  $1.36 \times 10^{-5}$  (Grids 1-4). In these grids 181 points were used along the circumferential directions. For a time step of 0.002 second, the predicted Strouhal number was approximately 0.025 for all the cases. A typical force and power spectral density for these cases is given in Figure 62 and Figure 63 respectively.

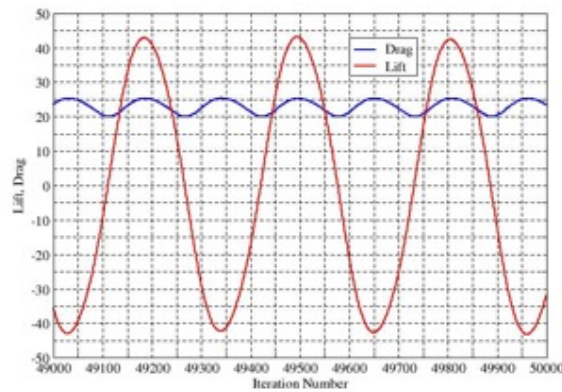


Figure 62: Typical force history for Grids 1-4 and time step of 0.002 seconds

For a time step of  $9.1 \times 10^{-5}$  seconds (for Grid 4), the predicted Strouhal number was 0.07. However, the amplitude of forces and moments decreased continuously with each time iteration. The overall view of the force history and a detailed view are given in Figure 64.

A study was conducted by refining grids in the circumferential directions (for Grids 6-8 given in Table 8). It was noted that the computed Strouhal number remained a constant, approximately 0.08 for all grids (6-8)



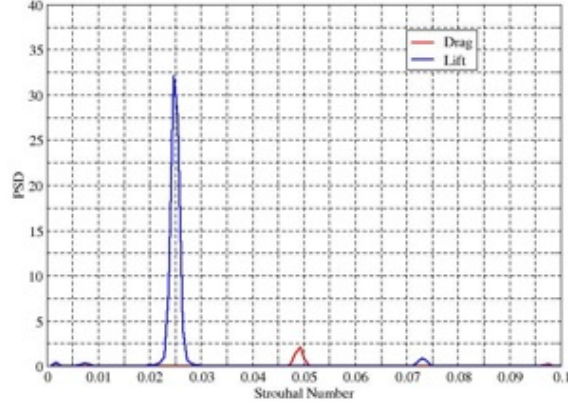


Figure 63: Typical PSD distribution for grids 1-4 and time step of 0.002 seconds

and the decay of the amplitude of forces disappeared for the refined grids. An overall view and a detailed view of the convergence history for Grid 6 are shown in Figure 65.

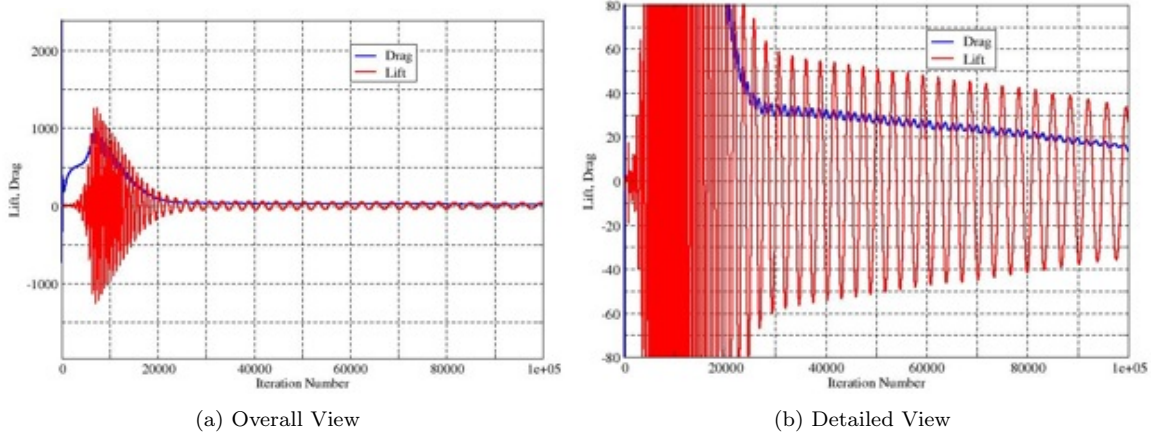


Figure 64: Force history for Grid 4 and time step of 9.1E-05 seconds

### Effect of Turbulence Model on Strouhal Number

In order to study the effect of the turbulence model on the vortex shedding frequency, various turbulence models are used. These include Spalart-Allmaras, Spalart-Allmaras DES,  $k-\omega$ ,  $k-\omega$  SST, Mentors baseline, Mentors baseline SST, Hybrid RANS/LES, and a wall-distance free model. Grid 6, given in Table 8, is used for this study since the grid is fine and the  $y^+$  value is less than 1. A time step of  $9.1 \times 10^{-5}$  seconds is used for these simulations, 50,000 iterations is used for attaining periodicity in predicted forces, and 8,192 data points were used for the calculation of the Strouhal number. The predicted Strouhal number from these simulations is given in Table 9. From these results, it can be seen that the turbulence model does not have a strong influence in getting the correct Strouhal number.

Table 9: The effect of turbulence models on Strouhal number

S-A Model	S-A DES	Baseline	Baseline SST	$k-\omega$	$k-\omega$ SST	Hybrid RANS/LES	Wall distance free
0.08	0.08	0.08	0.08	0.1	0.06	0.06	0.08

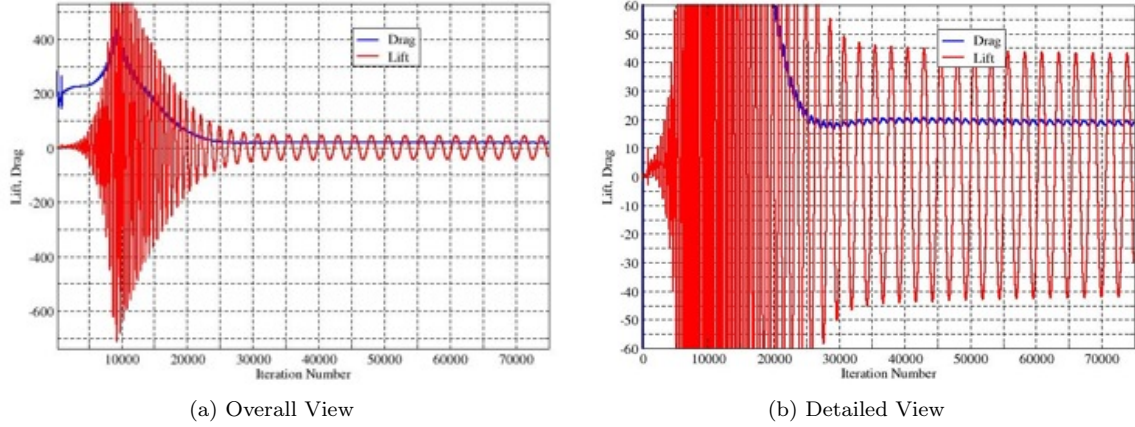


Figure 65: Force history for Grid 6 and time step of 9.1E-05 seconds

### Effect of Dimensionality on Strouhal Number

Three dimensional flow features have been reported in the literature [12] for turbulent vortex shedding from a circular cylinder. To study the 3-D behavior a grid was generated with a span length of 10 diameters for the cylinder and 61 points along the spanwise direction. The grid consisted of 15 million nodes, 14.5 million elements, and 44.7 million faces. The simulation was carried out using 96 processors and took approximately seven weeks to finish 15,000 iterations. The lift history and the power spectral density of lift and drag histories are plotted in Figure 66 and Figure 67 respectively. It can be seen from Figure 66 that the amplitude of the lift curve does not keep a fixed value as in the case of laminar vortex shedding. From the power spectral density curve, it can be seen that the Strouhal number for vortex shedding is approximately 0.25, which is in good agreement with experimental value of 0.27-0.31 [13, 14, 15].

The visualization of the data revealed spurious values of flow variables in the domain.

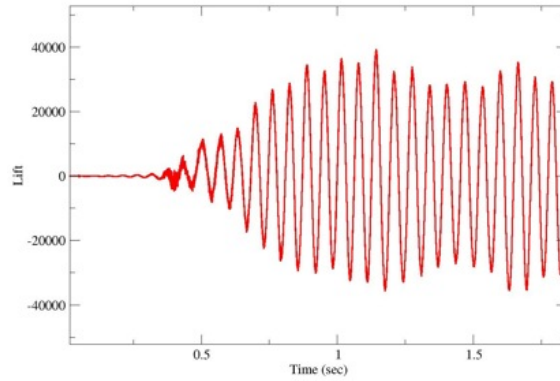


Figure 66: Lift history for vortex shedding from a circular cylinder

### 3.5 Summary of Prolate Spheroid Simulations

A steady flow past a 6:1 prolate spheroid at angles of attack of  $10^\circ$  and  $20^\circ$  will be used for the study of flow separation and vortical flows. The results of the computation will be compared with the experimental data available in the literature [16, 17, 18, 19, 20, 21, 22]. The 6:1 prolate spheroid used for the measurements is 1.37 m long and the Reynolds number based on the spheroid length is  $4.20 \times 10^6$ . The benchmark data was collected using hot wire and LDV measurements in the wind tunnel at the Virginia Polytechnic Institute and State University. This wind tunnel is a continuous, closed return, subsonic wind tunnel having a 7 m

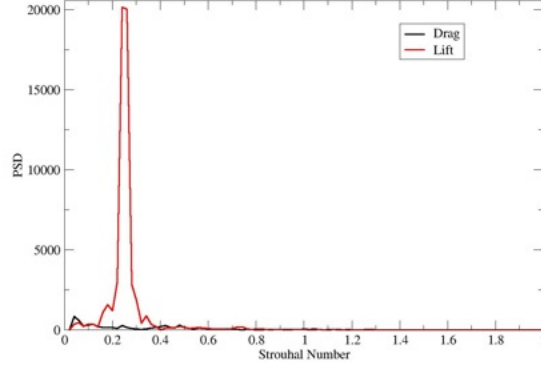


Figure 67: Power spectral density of lift and drag histories

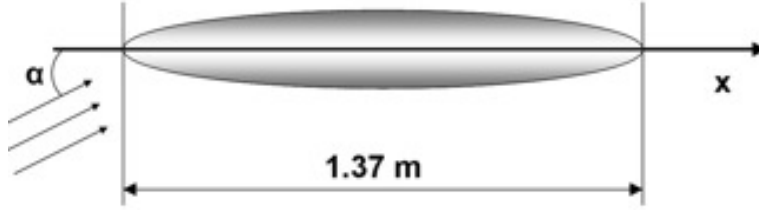


Figure 68: Pictorial representation of the 6:1 prolate spheroid

long and 1.8 m square test section and provides low free-stream turbulence levels of the order of 0.03%. A pictorial representation of the 6:1 prolate spheroid is shown in Figure 68. In the body-axis coordinate system,  $x$  is the distance along the model axis and is measured from the nose of the model. The radial distance, from the surface of the model is denoted by  $r$  and is measured perpendicular to the model axis. The azimuthal position,  $\phi$ , is measured from the windward side of the model.

Three different grids have been used for the simulation of flow past a prolate spheroid and are shown in Figure 69. In the first case only half of the geometry is considered for the simulation by taking advantage of the symmetry of the body and the other two cases use full 3-D geometry. A structured grid with 409,751 points and 354,000 cells is used for the first configuration (Figure 69(a)). The second grid is of structured topology and consists of 1,377,637 points and 1,241,170 cells (Figure 69(b)). The case is an unstructured grid with 650,212 points and 2,716,590 cells (Figure 69(c)).

Simulations have been carried out using weighted and unweighted least square approaches for angles of attack of  $10^\circ$  and  $20^\circ$  (a total of 12 simulations). Spalart-Allmaras turbulence model has been used for the modeling of fine scale turbulence. The oil flow pattern on the surface of the spheroid using weighted and un-weighted least squares for three different grids and two different angles of attack are compared in Figure 70 and Figure 71. It can be seen from the figures that the separation region is not very evident for Grid 2 and Grid 3 for both the angles of attack. This may be due to the fact that the grid resolution in the boundary layer region is fine enough to capture the separation accurately. Therefore the results from Grid 1 are used for the comparison with experimental data and other simulations.

Oil flow patterns from LES simulation by Fureby [22] (shown in Figure 72) is used for the comparison with the present simulation. A close examination of Figure 70, Figure 71, and Figure 72 reveals that the weighted least square method for gradient estimation produces better comparison with the LES simulation. The simulated streamline pattern around the spheroid for an angle of attack of  $10^\circ$  is shown in Figure 73. A comparison of calculated circumferential  $C_p$  distribution with the experimental data at a distance of  $x/L$  of 0.772 from the leading edge of the spheroid is shown in Figure 74 and Figure 75 for angle of attack 10 and 20 respectively. From the figure it can be seen that the weighted least square approach better predicts value of  $C_p$  when compared to the unweighted least squares for angle of attack of  $20^\circ$ . The location of the separation

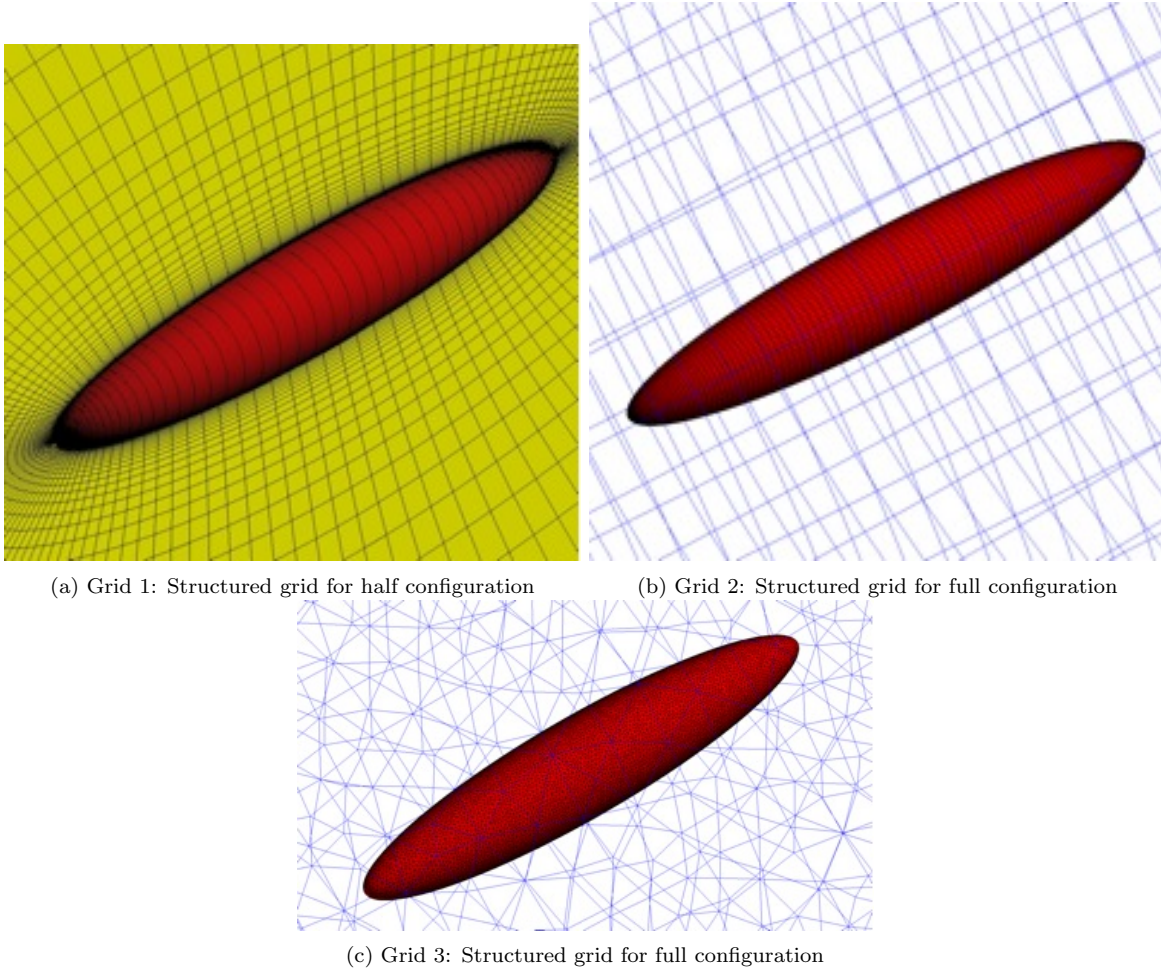


Figure 69: Configurations and grids used for prolate spheroid simulations

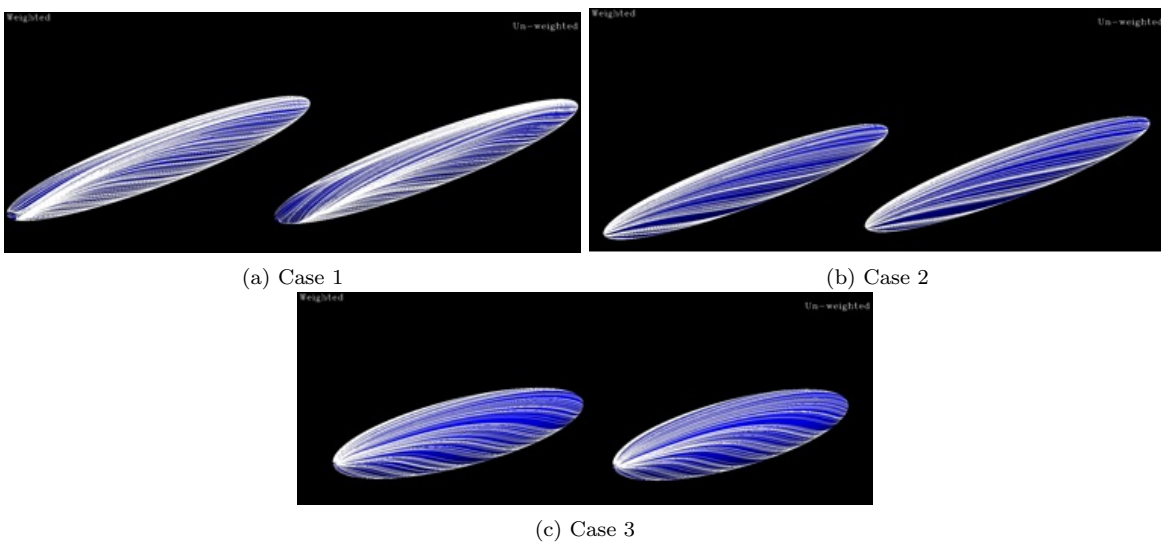


Figure 70: Oil flow pattern for an angle of attack of  $10^\circ$



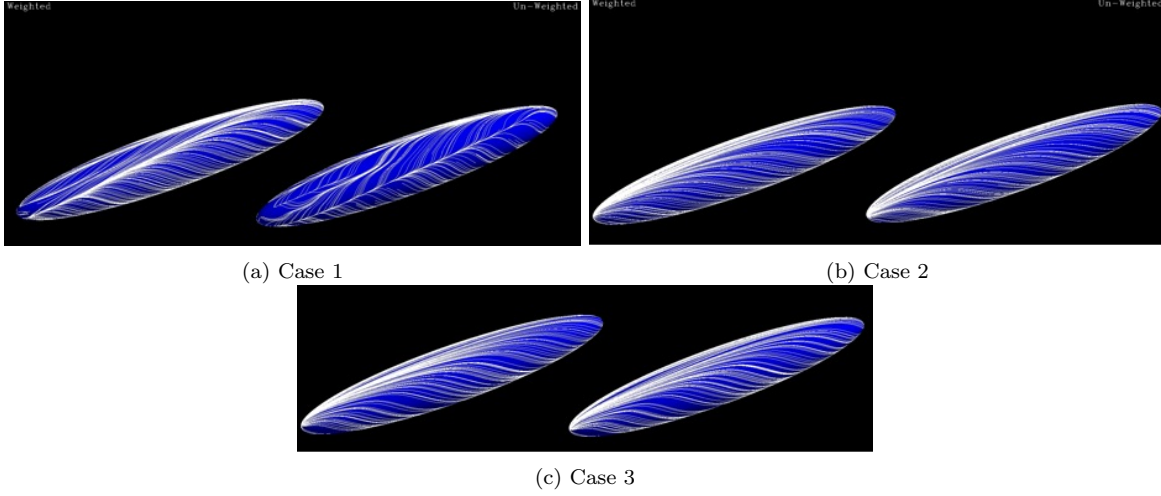


Figure 71: Oil flow pattern for an angle of attack of  $20^\circ$

regions are also better predicted by the weighted least square method as compared with unweighted least squares. However, there is a shift in the computed  $C_p$  distribution when compared to the experimental values.

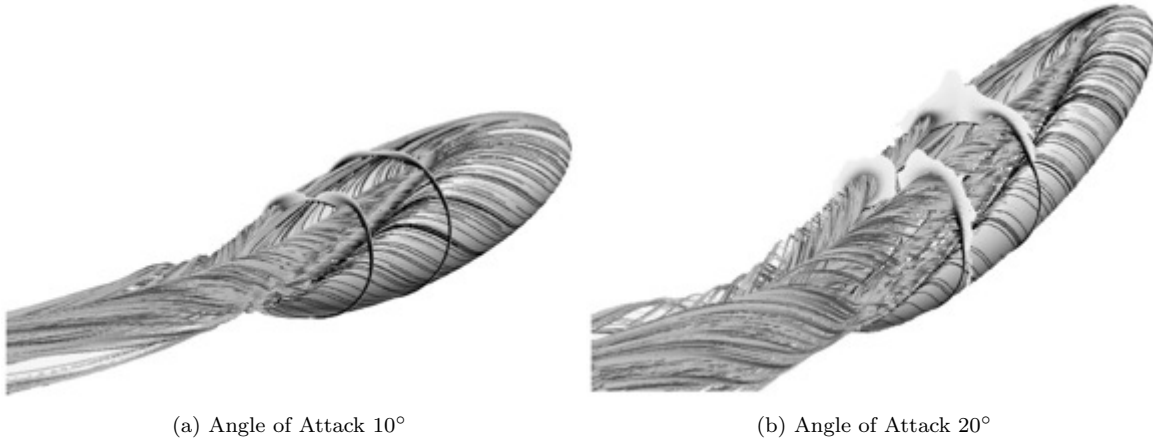


Figure 72: Cross flow separation associated with flow over a 6:1 prolate spheroid [22]

### 3.6 Summary of Shear Flow Simulations

Shear layers is one of the main flow features that affect the optical aberration of laser beams used for aero-optics. Therefore shear flows should be well captured for accurate analysis of aero-optics. In order to benchmark the AVUS code for the simulation of shear flows, a mixing layer problem will be considered. In this case, two parallel fluid streams with different velocities will be allowed to mix with each other to produce shear layers. Accurate estimation of viscosities as well as smaller numerical dissipation are required for the simulation of the size of the large scale eddies, frequency of the vortex shedding, and sustained mixing for the long duration of the simulation. A mixing layer will be simulated, and the results from the computation will be compared with the experimental data. The effect of the outflow boundary condition will also be studied to check the stability of the vortical structures.

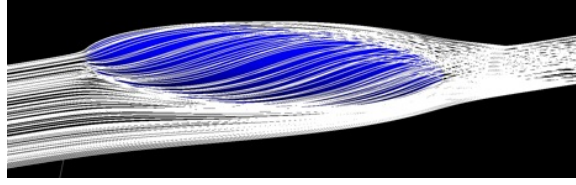


Figure 73: Streamline pattern over the spheroid for an angle of attack of  $10^\circ$

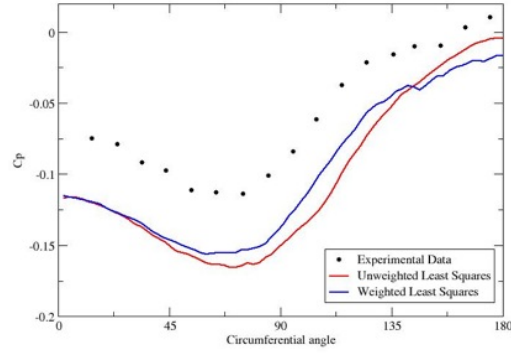


Figure 74: Circumferential  $C_p$  distribution for an angle of attack of  $10^\circ$

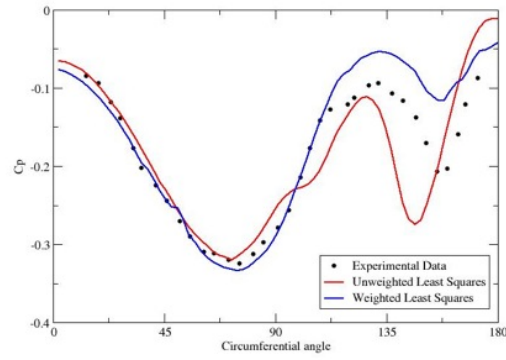


Figure 75: Circumferential  $C_p$  distribution for an angle of attack of  $20^\circ$

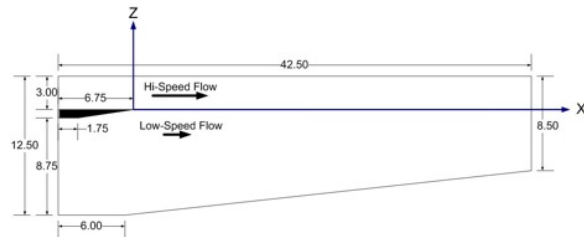
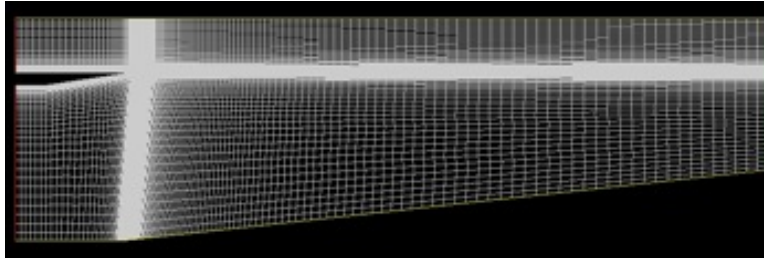
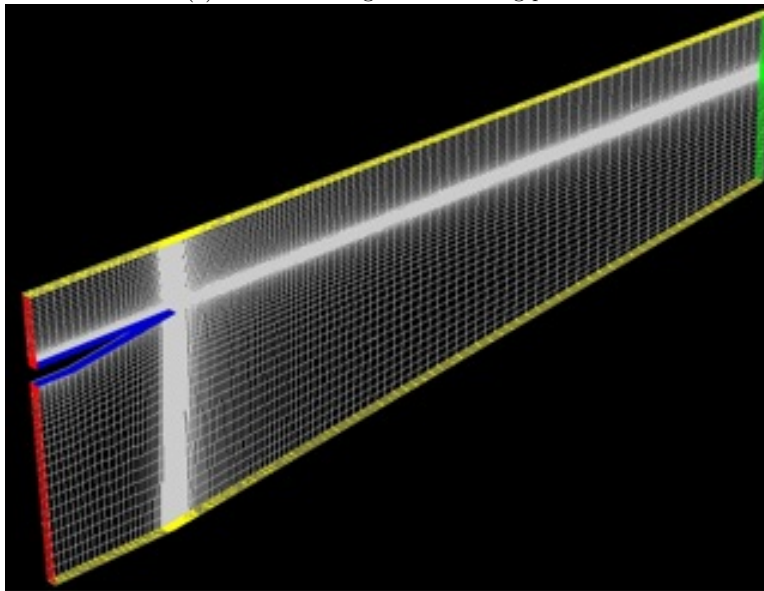


Figure 76: Geometry for the configuration I for the shear flow simulations





(a) A view of the grid in a cutting plane



(b) Overall view

Figure 77: Grid used for configuration I for shear flow simulation

## Configuration 1

The first configuration that is considered for shear layer simulation is based on the paper by Siegenthaler et.al. [1]. A few inconsistencies have been noticed in the experimental data for the turbulent mixing layers presented in Ref. [1]. The vortices had also disappeared after a few thousand iterations. Based on communication with the authors of the paper, a new geometry has been considered for the simulation base on the wind tunnel configuration as shown in Figure 76 [23]. In this figure all the dimensions are given in inches and the black wedge at the entrance to the test section represents the splitter. The trailing edge of the splitter plate is taken as a sharp corner. The test section contracts slightly to maintain a constant pressure gradient so that the shear layer spreads into the high- and low-speed streams in a manner similar to a canonical shear layer. The tunnel is an indraft configuration, and therefore the total temperature for both high- and low-speed streams is the lab ambient temperature and is approximately 298K. As a result, the static temperature of the high-speed stream is reduced below ambient and assuming isentropic flow it is approximately 265K for a Mach number of 0.78, although in practice there is likely to be substantial heat transfer. The low speed flow (Mach number of 0.12) flow is effectively at lab ambient. The high-speed flow is accelerated through a contraction, so its total P is effectively lab ambient. The low-speed flow is passed through a series of high-loss straw boxes to reduce its total pressure. The static pressure where the two flows merge is the same and is approximately 68 kPa. Static densities in the two flows are computed using static temperatures given above and the ideal gas law. The computed densities are 0.89 kg/m<sup>3</sup> for high-speed flow (Mach number of 0.78), and 0.79 kg/m<sup>3</sup> in low-speed flow (Mach number of 0.12).

The grid used for the simulation is shown in Figure 77 and it consists of 211,728 points and 159,960 cells. A time step of  $5.0 \times 10^{-8}$  seconds is used for the simulation and 400,000 time steps have been used for this simulation. Since the flow field is unsteady, animation of the flow field with regard to time iteration is used for the analysis of the results.

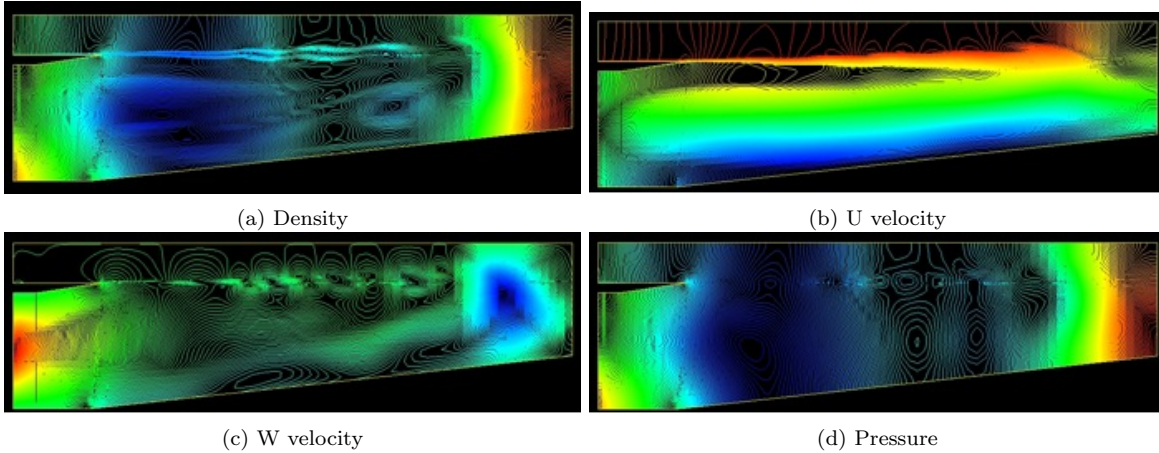


Figure 78: Visualization of the flow field after 400,000 time levels for configuration I

Snapshots of the results from the simulation, after 400,000 time levels are shown in Figure 78. It can be seen from the figure that the density and velocity components show the presence of the shear layer. However, these results show a low density and low speed fluid stream below the shear layer. This may be due the high density fluid at the exit region of the domain. Further investigation is required to study the effect of the boundary condition at the exit to avoid high density fluid at the outflow boundary.

## Configuration II

In addition to the case that was proposed, a second configuration by Samimy and Elliot [24, 25] was also used for evaluating AVUS code for mixing layer application. This experiment consists of two stream planar mixing layers with the upper stream being supersonic and the lower stream subsonic. A 3.175 mm thick splitter plate flat on the upper surface and is machined on the subsonic side to an angle of one degree over a length of 125 mm and separates the supersonic and subsonic regions. The thickness of the trailing edge

of the splitter plate is 0.5 mm. The grid used for the simulation is shown in Figure 79 and it consists of 236,740 points and 180,400 cells.

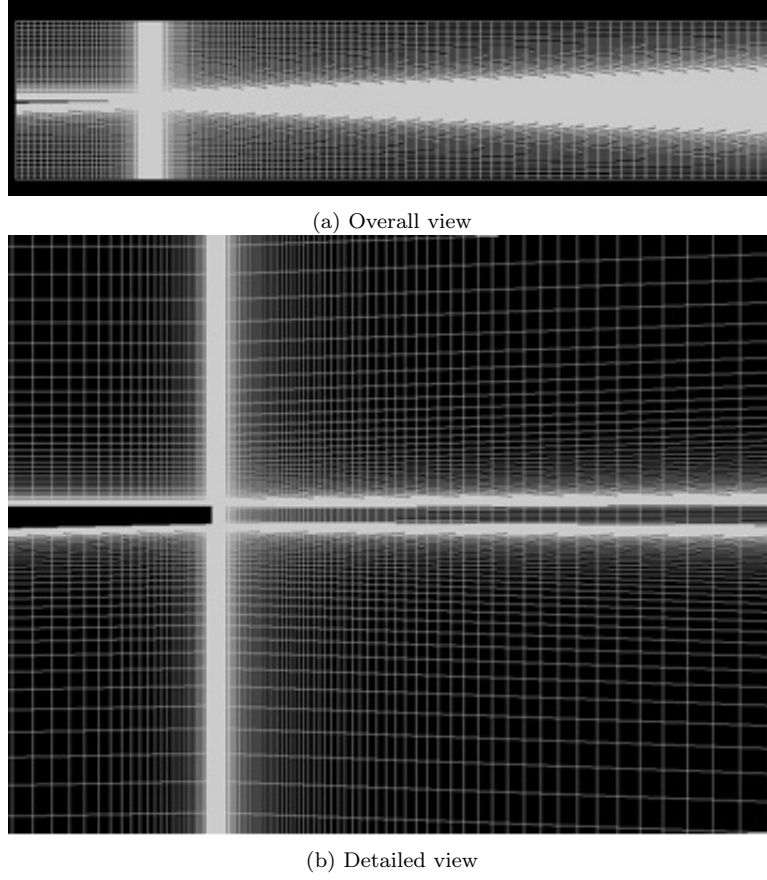
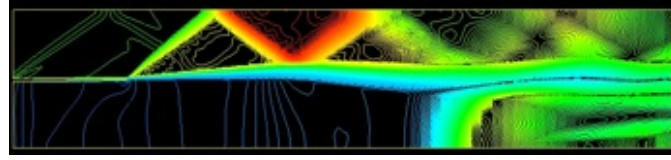


Figure 79: Geometry and grid used for configuration II for shear flow simulation

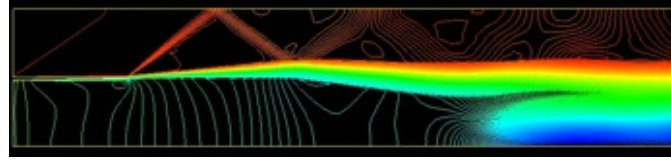
The flow parameter used for this simulation is shown in Table 10. In this table subscripts 1 and 2 represent the supersonic and subsonic streams respectively. A time step of  $5.0 \times 10^{-8}$  seconds is used for this simulation and the numerical integration has been carried out for 100,000 iterations. Similar to configuration I, animation of the flow development inside the channel is used for visualization of the simulation results. The distribution of flow variables at the end of 100,000 iterations is plotted in Figure 80. It can be seen from these figures that an expansion fan emanates from the trailing edge of the splitter plate, reflects back from the upper wall, and reflects again from the shear layer.

Table 10: Flow parameters for the mixing layer problem (Configuration II)

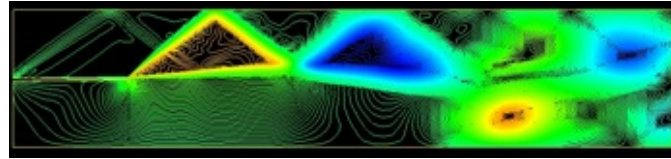
$T_o$ (K)	$P_{o1}$ (kPa)	$M_1$	$M_2$	$U_1$ (m/s)	$U_2/U_1$	$\rho_2/\rho_1$
291.0	314.0	1.80	0.51	479.5	0.355	0.638



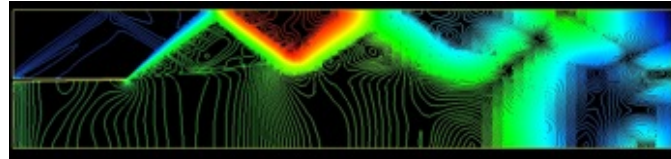
(a) Density



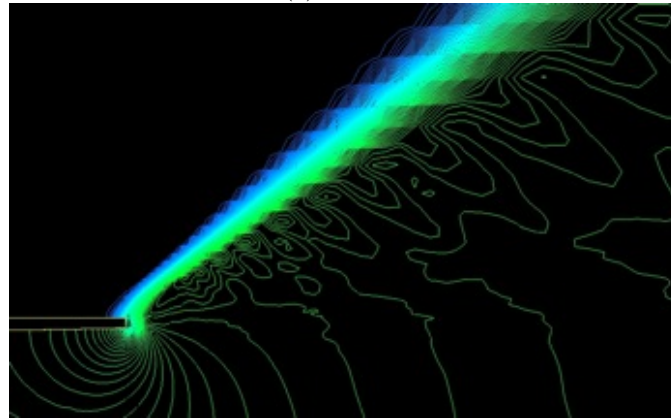
(b) U velocity



(c) W velocity



(d) Pressure



(e) Detailed view of pressure at the end of splitter plate

Figure 80: Results from the simulation of shear layers for configuration II

## 4 Conclusion

This report summarizes the efforts of the first two years of the Aero-optics Code Development Program managed by the Computational Sciences Branch, AFRL/RBAC. This initial effort focused on the acquisition of high-quality experimental data for configurations associated with aero-optics applications to perform future validation against, and evaluation and improvements to the in-house unstructured flow solver AVUS. The experimental data acquired from the University of Notre Dame consisted of a compressible shear layer, a 1.5-inch turret with a conformal window, a 1-foot turret with a conformal window, a 1-foot turret with a flat window, and a 4-inch cylindrical turret with a flat window.

With regards to the AVUS Code Analysis and Improvement for Aero-Optic Applications, weighted least square approach for the estimation of gradients for higher order spatial accuracy and viscous fluxes was implemented into AVUS and validated. Numerical experiments showed that the weighted averaging based gradient estimation predicts better shock location (using transonic NACA0012 benchmark data) and proper location of separation region (prolate spheroid data). Simulation of an inviscid vortex convection problem showed numerical dissipation in the domain causing the vortex to change shape and to introduce spurious values in the domain. Various trials such as different boundary conditions, velocity corrections, convergence of exact Riemann solver, spatial and temporal accuracies different approaches for gradient estimation, and use of serial processing did not improve the simulated results. Further investigation is required to find the cause of this problem. Laminar and turbulent flow past a circular cylinder was conducted. For a two-dimensional case, the laminar simulations predicted correct Strouhal number, while the turbulent cases predicted lower Strouhal number as compared with experimental data. Various turbulent models used for the simulation showed very little or no effect on the predicted Strouhal number. The use of a 3-D grid, with 10 diameters in the spanwise direction, helped predict accurate Strouhal number.

## 5. References

- [1] Siegenthaler, J., Gordeyev, S., and Jumper, E., “Shear Layers and Aperture Effects for Aero-Optics,” AIAA Paper 2005-4772, 36th AIAA Plasmadynamics and Laser Conference, Toronto, Canada, June 2005.
- [2] Gordeyev, S., Hayden, T., and Jumper, E., “Aero-Optical and Hot-Wire Measurements of the Flow Around the Hemispherical Turret With a Flat Window,” AIAA Paper 2004-2450, 35th AIAA Plasmadynamics and Laser Conference, Portland, Oregon, July 2004.
- [3] Dumas, J., Fuqua, M., and Hayden, T., “Final Report: Boundary Layer Survey of the Subsonic Wind Tunnel,” Tech. rep., Department of Aeronautics, United States Air Force Academy, Colorado Springs, Colorado, May 2005.
- [4] Gordeyev, S., Hayden, T. E., and Jumper, E. J., “Aero-Optical and Flow Measurements Over a Flat-Windowed Turret,” *AIAA J.*, Vol. 45, No. 2, 2007, pp. 347–357.
- [5] Strang, W. E., Tomaro, R. F., and Grismer, M. J., “The Defining Methods of Cobalt60: A Parallel, Implicit, Unstructured Euler/Navier-Stokes Flow Solver,” AIAA Paper 99-0786.
- [6] Forsythe, J. R., Strang, W. Z., and Hoffmann, K. A., “Validation of Several Reynolds-Averaged Turbulence Models in a 3-D Unstructured Code,” AIAA Paper 2000-2552.
- [7] Strang, W. Z., “Cobalt60: Users Manual,” Tech. rep., Sept 2000.
- [8] Koomullil, R. P., *Flow Simulation System for Generalized Static and Dynamics Grids*, Ph.D. thesis, Mississippi State University, MS, 1997.
- [9] Koomullil, R. P. and Soni, B. K., “Wind Field Simulations in Urban Area,” AIAA Paper 2001-2621, 15th AIAA Computational Fluid Dynamics Conference, Anaheim, CA, June 2001.
- [10] Hyams, D. G., *An Investigation of Parallel Implicit Solution Algorithms for Incompressible Flows on Unstructured Topologies*, Ph.D. thesis, Mississippi State University, MS, 2000.
- [11] Mavriplis, D. J., “Revisiting the Least-Squares Procedure for Gradient Reconstruction on Unstructured Meshes,” AIAA Paper 2003-3986, 16th AIAA Computational Fluid Dynamics Conference, Orlando, FL, June 2003.
- [12] Nichols, R., “Comparison of Hybrid Turbulence Models for a Circular Cylinder and a Cavity,” *AIAA J.*, Vol. 44, No. 6, 2006, pp. 1207–1219.
- [13] Jones, G., Cincotta, J. J., and Walker, R., “Aerodynamic Forces on a Stationary and Oscillating Circular Cylinder at High Reynolds Number,” NASA TR-R-300, Oct 1968.
- [14] Roshko, A., “Experiments on the Flow past a Circular Cylinder at Very High Reynolds Number,” *J. Fluid Mech.*, Vol. 10, No. 3, 1961, pp. 345–356.
- [15] Schlichting, H., *Boundary Layer Theory*, McGraw-Hill Book Company, seventh ed., 1979.
- [16] Chesnakas, C. and Simpson, R., “Measurements of the Turbulence Structure in the Vicinity of a 3-D Separation,” *J. Fluids Eng.*, Vol. 118, No. 2, 1996, pp. 268–275.
- [17] Chesnakas, C. and Simpson, R., “A Detailed Investigation of the 3-D Separation About a 6:1 Prolate Spheroid,” *AIAA J.*, Vol. 35, No. 6, 1997, pp. 990–999.
- [18] Wetzel, T., Simpson, R., and Chesnakas, C., “Measurement of Three-Dimensional Crossflow Separation,” *AIAA J.*, Vol. 36, No. 4, 1998, pp. 557–564.
- [19] Goody, M., Simpson, R., and Chesnakas, C., “Separated Flow Surface Pressure Fluctuations and Pressure-Velocity Correlations on Prolate Spheroid,” *AIAA J.*, Vol. 38, No. 2, 1998, pp. 266–274.

- [20] Goody, M., *An Experimental Investigation of Pressure Fluctuations in Three-Dimensional Turbulent Boundary Layers*, Ph.D. thesis, VPI&SU, Blacksburg, VA, 1999.
- [21] Goody, M. C., Simpson, R. L., Engel, M., Chesnakas, C. J., and Devenport, W. J., “Mean Velocity and Pressure and Velocity Spectral Measurements within a Separated Flow around a Prolate Spheroid at Incidence,” AIAA Paper 98-0630.
- [22] Fureby, C., Alin, N., Wikstrom, N., Menon, S., Svanstedt, N., and Persson, L., “Large-Eddy Simulation of High-Reynolds-Number Wall-Bounded Flows,” *AIAA J.*, Vol. 42, No. 3, 2004, pp. 457–468.
- [23] Rennie, R., Siegenthaler, J., and Jumper, E., “Forcing of a Two-Dimensional, Weakly-Compressible Subsonic Free Shear Layer,” AIAA Paper 2006-0561, 44th AIAA Aerospace Sciences Meeting, Reno, NV, January 2006.
- [24] Samimy, M. and Elliott, G., “Effect of compressibility on the characteristics of free shear layers,” *AIAA J.*, Vol. 28, No. 3, 1990, pp. 439–445.
- [25] Nelson, C., , and Nichols, R., “Evaluation of Hybrid RANS/LES turbulence models using an LES code,” AIAA Paper AIAA Paper 2003-3552, 16th AIAA Computational Fluid Dynamics Conference, Orlando, FL, June 2003.